Mathematical models of calcium signalling in the context of cardiac hypertrophy

Hilary Hunt
ORCID iD: 0000-0003-3799-7214

Doctor of Philosophy

February 2020

School of Mathematics and Statistics
The University of Melbourne

The thesis is being submitted in fulfilment of the degree.
The degree is not being completed under a jointly awarded degree.

Abstract

Throughout the average human lifespan, our hearts beat over 2 billion times. With each beat, calcium floods the cytoplasm of every heart cell, causing it to contract until calcium re-uptake allows the heart to relax, ready for the next beat. However, calcium is known to be critical in other cell functions, including growth. Calcium plays a central role in mediating hypertrophic signalling in ventricular cardiomyocytes on top of its contractile function. How intracellular calcium can encode several different, specific signals at once is not well understood.

In heart cells, calcium release from ryanodine receptors (RyRs) triggers contraction. Under hypertrophic stimulation, calcium release from inositol 1,4,5-trisphosphate receptor (IP_3R) channels modifies the calcium contraction signal, triggering dephosphorylation and nuclear import of the transcription factor nuclear factor of activated T cells (NFAT), with resulting gene expression linked to cell growth.

Several hypotheses have been proposed as to how the modified cytosolic calcium contraction signal transmits the hypertrophic signal to downstream signalling proteins, including changes to amplitude, duration, duty cycle, and signal localisation. We investigate the form of these signals within the cardiac myocyte using mathematical modelling. Using a compartmental heart cell model, we show that the effect of calcium channel interaction on the global calcium signal supports the idea that increased calcium duty cycle is a plausible mechanism for IP_3-dependent hypertrophic signalling in cardiomyocytes.

A corresponding calcium signal within the nucleus must be present to maintain NFAT in the nucleus and thus allow NFAT to alter gene expression, initiating hypertrophic remodelling. Yet the nuclear membrane is permeable to calcium and this must all occur on a background of rising and falling calcium with each heartbeat. The mechanisms shaping calcium dynamics within the nucleus remain unclear.

We use a spatial model of calcium diffusion into the nucleus to determine the effects of buffers and cytosolic transient shape on nuclear calcium dynamics. Using experimental data, we estimate the diffusion coefficient and the effects of buffers on nuclear [Ca^{2+}]. Additionally, we explore the effects of altered cytosolic calcium transients and calcium release on nuclear calcium. To approximate experimental measurements of nuclear calcium, we find that there must be perinuclear Ca^{2+} release and nonlinear diffusion. Comparisons of 1D and 3D models of calcium in the nucleus suggest that spatial variation in calcium concentration within the nucleus will not have a large effect on calcium-mediated gene regulation.

This work brings us closer to understanding the signalling pathway that leads to pathological hypertrophic cardiac remodelling.

Declaration of Authorship

This is to certify that

1. the thesis comprises only my original work towards the PhD except where indicated in the Preface;

2. due acknowledgement has been made in the text to all other material used; and

3. the thesis is less than 100,000 words in length, exclusive of tables, maps, bibliographies and appendices.

Signed:

_____

Hilary Hunt, February 2020

Preface

Chapter 2 is adapted from an article, IP_3R Ca^{2+} release shapes cytosolic Ca^{2+} transients for hypertrophic signalling in ventricular cardiomyocytes, that was submitted to the Biophysical in January 2020, authored by me (Hilary Hunt; **HH**), Agne Tilunaite (AT), Greg Bass (GB), Christian Soeller (CS), H. Llewelyn Roderick (HLR), Vijay Rajagopal (VR), and Edmund J. Crampin (EC) (a previous draft is also available at (58)). I was the primary author of this publication and contributed to approximately 85% of the work. Regarding the contributions of the authors:

- Conceived the study: EJC, VR, HLR, CS, and GB
- Developed the model: **HH**, EJC, VR, AT
- Analysed the model: **HH**, and AT with input from EJC and VR
- Drafted the manuscript: **HH**, with input from EJC, AT, VR.

The experimental data used in Chapter 3 and Chapter 4 was collected in the Babraham Institute by Gregory Bass, supervised by H. Llewellyn Roderick. Post-processing of the data, i.e. deconvolution, and measurement of nucleus size was also performed by Gregory Bass. Further data analysis and plot generation was performed by myself.

All other work in the thesis is my own. None of the work in the thesis has been submitted for other qualifications. None of the work in the thesis was carried out prior to enrolment in the degree. No third party editorial assistance was provided in preparation of the thesis. I have been supported by the Australian Government through an Australian Research Training Program Scholarship and the Australian Research Council Discovery Projects funding scheme (project DP170101358).

Citation for Third party copyright material	Location	Permission given
Katz, A.M. Congestive Heart Failure. *New England Journal of Medicine*, 293(23):1184–1191, 1975. doi: 10.1056/NEJM197512042932309	Figure 1.2	Y
Hinch, R. et al. A Simplified Local Control Model of Calcium-Induced Calcium Release in Cardiac Ventricular Myocytes. *Biophysical Journal*, 87(December):24–29, 2004. doi: 10.1529/biophysj.104.049973	Figure 2.3	Y

Acknowledgements

There is a long list of people I must thank for enabling me to get this far. First and foremost, thank you to my supervisors Edmund Crampin and Vijay Rajagopal. Thank you for giving me the oppotunity to work with you and for your continuous support over my PhD. Thank you for celebrating my achievements and encouraging me through my doubts. Your professional and scientific guidance over the last four years has been invaluable in shaping my path forward as a researcher. It has been an extraordinary experience working with you both.

Next, I would like to thank my experimental collaborators Llewelyn Roderick, Christian Soeller, and Gregory Bass for their advice and insight into the physiology and experimental methods used in the study of cardiac calcium. Without you, my research would not be nearly as grounded in experimental data.

I woud also like to thank my computational collaborators: Agne Tilünaite for all of your advice, constructive criticism and relentless encouragement; and David Ladd for your technical support and guidance.

I would like to acknowledge the Australian Government Research Training Program Scholarship and the University of Melbourne School of Mathematics and Statistics for their financial support. In particular, Kirsten Hoak for assisting with any and all administrative questions.

Thank you to everyone in the Mathematical and Computational Biology group for creating a supportive work environment, stimulating discussions, and fostering a sense of belonging between staff and students. Thank you to my friends and fellow residents of Old Geology South, both past and present, for moral support, thought-provoking conversations, and PhD tips. In particular, thank you Claire Miller, Tiffany Leung, Michael Lydeamore, Alex Zarebski, Ada Yan, Jackson Kwok, Stuart Johnston, Sarah Belet, Domenic Germano, Dominic Maderazo, and Agne Tilünaite. Without you, my PhD experience would not have been as enjoyable as it has been.

Finally, I would like to thank my family for everything you've done for me. Thank you for your support and encouragement through decades of education, and for being there for me through everything.

Contents

List of Figures

List of Tables

Acronyms

Ang-II	Angiotensin II
ARVM	Adult rat ventricular myocyte
ATP	Adenosine triphosphate
Ca^{2+}	Calcium ion
CaM	Calmodulin
CaRU	Calcium release unit, also denoted CRU
CICR	Calcium-induced calcium release
CnA	Calcineurin A
DNA	Deoxyribonucleic acid
ECC	Excitation contraction coupling
ET-1	Endothelin 1
ETC	Excitation transcription coupling
FDHM	Full duration at half maximum
HDAC5	Histone deacetylase 5
IP_3	Inositol 1,4,5-trisphosphate, also referred to as '$InsP_3$'
IP_3R	Inositol 1,4,5-trisphosphate receptor
jSR	Junctional sarcoplasmic reticulum
LTCC	L-type calcium channel, also denoted LCC
NCX	Sodium-calcium exchanger
NE	Nuclear envelope
NFAT	Nuclear factor of activated T cells
NPC	Nuclear protein complex
PMCA	Sarcolemmal Ca^{2+} ATPase
RyR	Ryanodine receptor

SERCA	Sarco/endoplasmic reticulum Ca^{2+} ATPase
SR	Sarcoplasmic reticulum
TnC	Troponin C
TTP	Time to peak

Chapter 1

Background biology and models

Pathological cardiac hypertrophy refers to heart cell growth to the point of disease. It can be caused by genetic or pathological issues and often accompanies, and exacerbates, other cardiovascular conditions. Cardiovascular disease is one of the most common causes of death globally with an annual mortality rate in the millions (162). Heart failure, aggravated by hypertrophy, is one of the biggest contributors to this statistic. Despite this, many aspects of heart function and regulation remain unknown.

One such unknown is the exact nature of the role of calcium in regulating the hypertrophic pathway. Here 'calcium' refers to the bivalent ionic form of calcium, Ca^{2+}. Ca^{2+} is a universal secondary signalling molecule. It is ubiquitous both within our cells and in a startling number of signalling pathways. The mechanisms behind how calcium can perform all of its many and varied roles are not fully understood. In particular, here how such a simple molecule can perform the role of triggering every beat within every heart cell while regulating hypertrophic gene expression within both the cell cytosol and nuclei continues to be a mystery. In this thesis, we investigate the role of intracellular calcium signalling in initiating cardiac hypertrophy through computational modelling.

We use computational models, informed by experimental measurements, to understand the complex role of calcium signalling within heart cells. Mathematical modelling allows us to better understand calcium channel interactions as well as the nonlinear dynamics generated by the many intracellular molecules that calcium interacts with. The process of constructing biophysical models that explain experimental results allows us to better understand the implications of

experimentally generated data. We can explore the potential underlying mechanisms and predict the results of future experiments that may not yet be possible with current methods.

The overarching aim of this study is to use mathematical modelling to understand physiological intracellular cardiomyocyte calcium dynamics and how they are altered to initiate hypertrophic remodelling. These models could be used to better understand the complete sequence of signals within the cardiac hypertrophic pathway. This would in turn allow more nuanced identification of hypertrophic triggers and treatments.

Chapter 1 details the structure and function of the heart and cardiac hypertrophy. We explain the known roles of calcium in cell contraction and hypertrophic remodelling as well as a brief overview of calcium models and the hypertrophic pathway, highlighting gaps in our understanding.

Following this, Chapter 2 models the changes to cytosolic calcium dynamics following activation of IP_3R channels which are calcium channels implicated in the hypertrophic pathway. Aspects of the cytosolic calcium signal that could trigger hypertrophic remodelling are considered. We describe the space of possible alterations to cytosolic calcium that could result in hypertrophic remodelling. We show that a key new candidate proposed by Hannanta-anan and Chow (49) as a method of hypertrophic signal transmission in HeLa cells is also possible in heart cells.

In Chapter 3 we construct a model of nuclear calcium dynamics during the calcium contraction signal in heart cells. Here we aim to construct the simplest biophysical model that can explain temporal patterns of calcium movement we see within confocal line-scan experiments. Our model describes the effects of nucleus size, the nuclear envelope and calcium buffers on nuclear calcium. We then use the model to show the effects of any alterations to cytosolic calcium dynamics on nuclear calcium dynamics.

Chapter 4 explores the importance of nuclear geometry in determining spatial variation of nuclear calcium concentration. We find an algebraic expression to determine calcium concentration within the 3D nucleus given a cytosolic calcium signal. While the mechanisms of hypertrophic calcium signalling are even less understood in the nucleus than the cytosol, we determine that the longitudinal movement of calcium is unlikely to be important in the signalling pathway. The

approximations made in Chapter 3 are justified. Additionally, we explore the effect of calcium oscillation frequency on nuclear calcium.

Finally, Chapter 5 discusses the advances made in this study, its limitations and the implications of our results on future research.

1.1 The structure and cellular makeup of the heart

During the average human lifespan, the heart will beat over 2 billion times. Mammalian hearts are made up of two, connected pumps. One, consisting of the right atrium and right ventricle, pumps blood from systemic circulation (the body) towards the lungs for reoxygenation; the other, consisting of the left atrium and left ventricle, pumps the oxygenated blood from the lungs back into systemic circulation. Figure 1.1 shows a schematic illustration of the circulatory system. Blood enters the heart through the atria and is pumped out and through the rest of the circulatory system through the ventricles. The ventricles experience greater pressure than the atria and have thicker, stronger walls. The left ventricle, having to pump blood further, is about twice as thick as the right ventricle (67).

To push blood around the body, the heart undergoes synchronised contractions – the walls of the atria contract inwards to eject blood into the ventricles before relaxing to refill, and subsequently the ventricles contract inwards to eject blood out of the heart before relaxing to refill from the atria.

Heart contractions are coordinated by electrical signals generated by specialised 'pacemaker' cells in the sinoatrial (SA) node. This is a band of cells found between the superior vena cava (the main vein) and the right atrium. While these are not the only cardiac cells capable of being pacemakers, they fire more rapidly than the other cardiac depolarising cells and release a wave of depolarisation, activating the others (108, 1, 153). The wave of depolarisation travels through nearby myocardial cells, and spreads to cause a contraction in each atrium. From there, the signal travels through the atrioventricular (AV) node and AV bundle (108). These propagate the electrical signal to the base of the heart to initiate ventricular contraction (67).

The ventricular walls are made up of overlapping, interconnected muscle fibers – myocardial cells, arranged in a spiral shape (45, 142). Myocardial cells are also

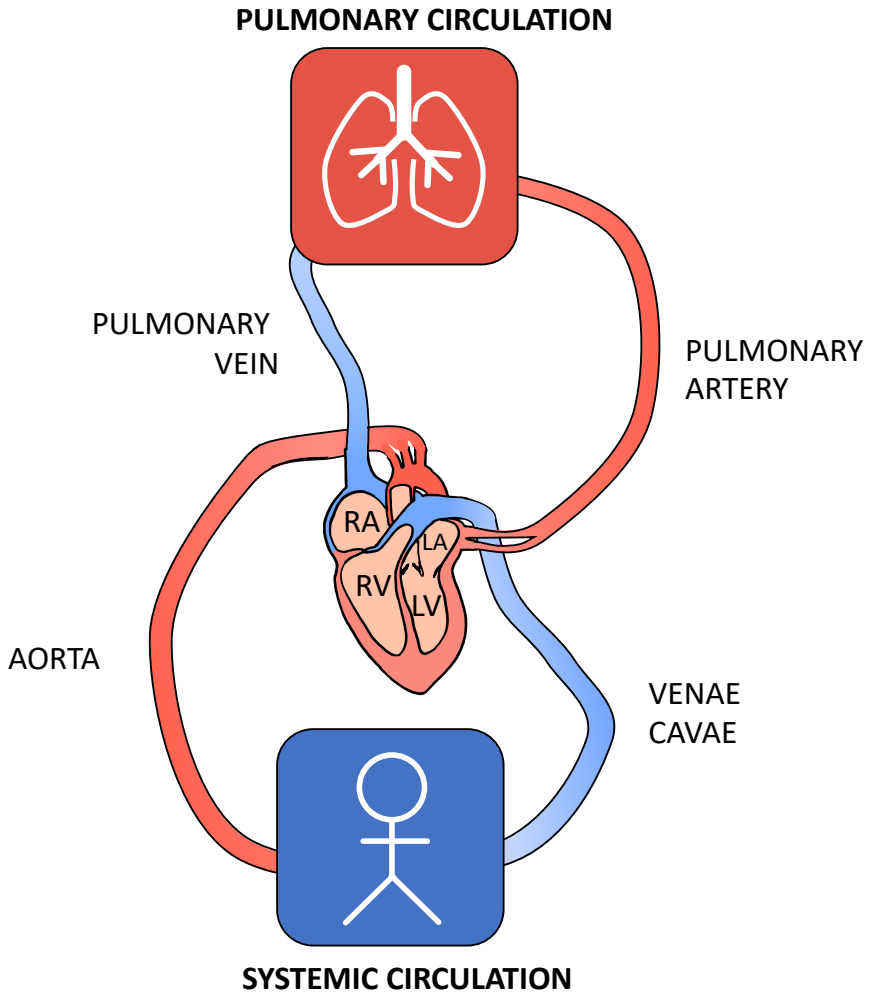

Figure 1.1: A simplified diagram of the mammalian circulatory system. The heart is divided into four distinct chambers. Two atria, and two ventricles. The atria (RA and LA) draw in blood from the circulatory system and push it into the ventricles. The right ventricle (RV) pumps blood into pulmonary circulation where it is oxygenated in the lungs. The left ventricle (LV) pumps the oxygenated blood, drawn in through the left atrium (LA), around the body. Since this requires the most force, the left ventricle is usually the largest of the four chambers.

known as 'cardiac myocytes' or 'cardiomyocytes'. In response to the electrical signal from the pacemaker cells, these cells contract, pushing the blood around the body. In this thesis, I focus on the function of these cells.

1.1.1 Cardiomyocyte structure

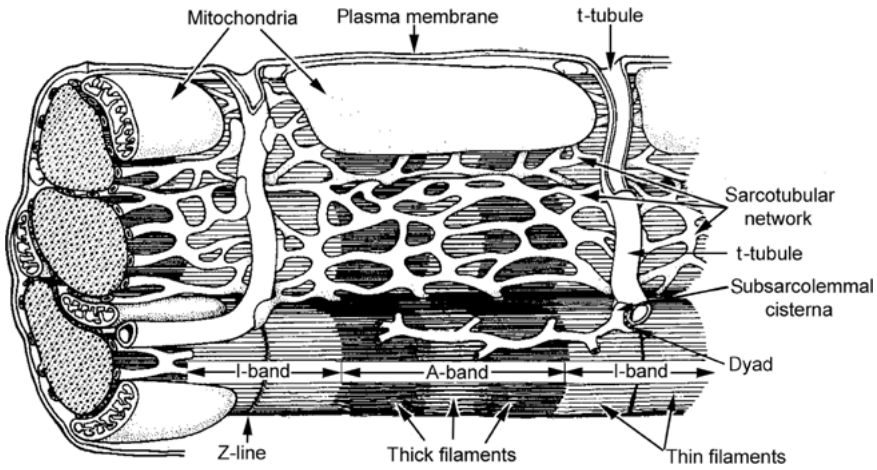

Figure 1.2: The ultrastructure of a myocardial cell. Pictured here is a section of a cardiomyocyte. The space between two Z-lines, a.k.a. z-disks, is called a 'sarcomere' and consists of two half I-bands and an A-band. The length of this diagram varies with cell contraction. At dilation, Z-lines are spaced approximately 2μm apart. In rats and humans, left ventricular myocyte length is approximately 135μm (150). The mitochondria are the powerhouses of the cell where ATP is produced. The plasma membrane invaginates the cell in the form of t-tubules, narrowing the distance between the extracellular space and the sarcoplasmic reticulum to enable faster propagation of electrical signals into the cell. The small space between the t-tubules and the sarcoplasmic reticulum is known as a dyad. Reproduced with permission from Katz (66), copyright Massachusetts Medical Society.

By volume, approximately half of each cardiomyocyte is made up of myofibrils, bundles of contractile proteins which can be further divided into thick and thin myofilaments (see Figure 1.2). Myofibrils are arranged in alternating bands of fibers, connected end to end within the cell. The thick filaments of the myofibrils make up what are known as A (anisotropic) bands and are primarily composed

Component	Percentage of Cell Volume
Myofibrils	46.7
Mitochondria	36
Sarcoplasmic reticulum	3.5
Subsarcolemmal cisternae	0.35
Sarcotubular network	3.15
Nuclei	2
Other (mainly cytosol)	11.8

Table 1.1: The makeup of a rat left ventricular myocyte (109).

of myosin, while sections of thin filaments are known as I (isotropic) bands and are primarily composed of actin.

Cardiomyocytes can be segmented into smaller contractile units called sarcomeres. These are the fundamental contraction units of the cell. Each sarcomere consists of two (half) I bands separated by an A band. Adjacent sarcomeres are connected to each other by Z (zwischen – meaning "between") discs which are located between two half I bands (see Figure 1.2).

The rest of the cell consists mostly of mitochondria which produce ATP; the sarcoplasmic reticulum (SR), which acts as Ca^{2+} storage for the cell; and two nuclei, where DNA is stored (see Table 1.1) (67). The nuclei are separated from the cytosol by a double membrane known as the nuclear envelope (NE). The space between each of the two membranes that make up the nuclear envelope is confluent with the sarcoplasmic reticulum and is also part of the cell's stores. The ion channels present on the nuclear envelope are believed to be similar to the channels found on the sarcoplasmic reticulum.

It is important to note that there are a variety of structural differences present between cell types, e.g. atrial vs ventricular, and species, e.g. rabbit vs rat. These differences encompass cell makeup, i.e. the percentages described in 1.1 are not uniform across species or cardiomyocytes; channel number and distribution; and calcium handling. In this work, we focus primarily on rat ventricular myocytes and it is the structure and function of these myocytes that are described herein.

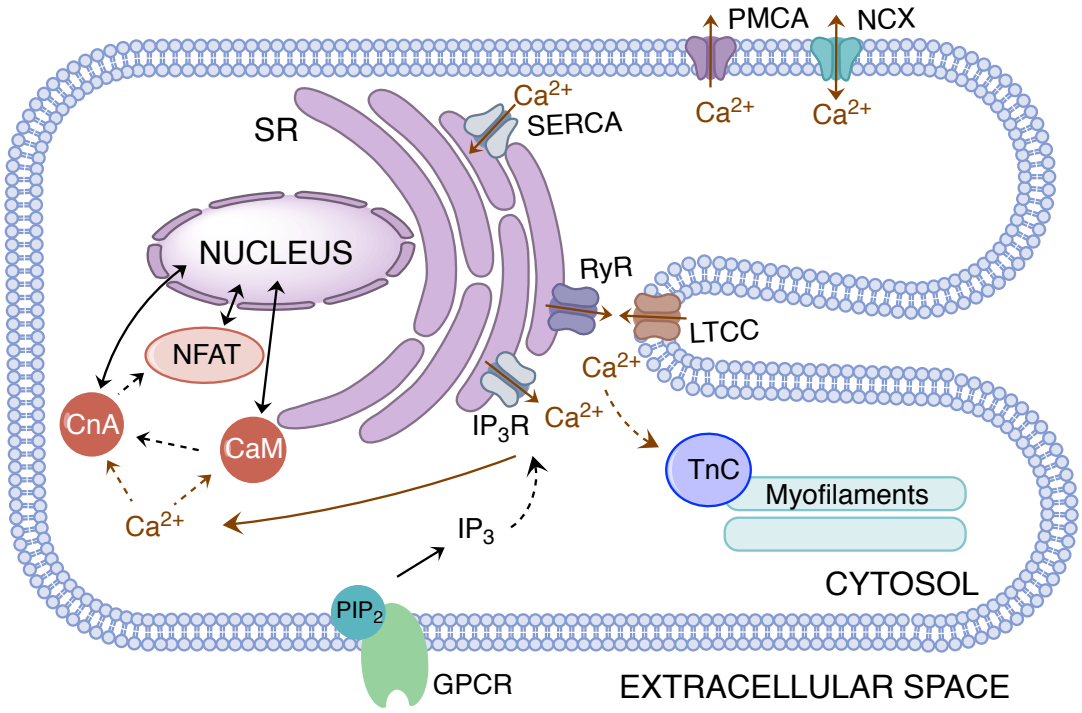

Figure 1.3: Schematic diagram showing key Ca^{2+} signalling pathways in the cardiomyocyte. excitation contraction coupling (ECC) Ca^{2+} signalling processes include RyRs, L-type calcium channel, also denoted LCCs (LTCCs), sarco/endoplasmic reticulum Ca^{2+} ATPase (SERCA), sodium-calcium exchanger (NCX), sarcolemmal Ca^{2+} ATPase (PMCA) and troponin C (TnC). Growth-related IP_3– CnA/CnA signalling processes include IP_3Rs, G protein-coupled receptor (GPCR), phosphatidylinositol 4,5-bisphosphate (PIP_2), calmodulin (CaM), calcineurin A (CnA) and nuclear factor of activated T cells (NFAT). Note that NCX is depicted outside of the t-tubule, the sarcolemmal invagination that allows RyR and LTCC channels to collocate. NCX can also be found within the t-tubules of cardiomyocytes however, in this work, we have not explicitly modelled it within the calcium release unit, also denoted CRU (CaRU) so it is shown separately

1.1.2 The contraction pathway

Contraction, the essential function of cardiomyocytes, is initiated by an electrical signal and transmitted internally through Ca^{2+} release. When an electrical signal reaches a cardiomyocyte, the outer membrane (sarcolemma) is depolarised.

This activates the L-type calcium channel, also denoted LCCs (LTCCs). These are voltage gated channels on the sarcolemma, the cell's outer membrane, that allow Ca^{2+} to enter the cell. They are concentrated on invaginations of the cell membrane called t-tubules. These invaginations penetrate the cytosol to

bring the outer membrane close to the sarcoplasmic membrane – the membrane surrounding the sarcoplasmic reticulum which contains the bulk of the cell's Ca^{2+} stores.

Throughout the cell, these t-tubules create small pockets of the cell cytosol, partially insulated from the rest of the cell by the sarcolemma and SR membrane, known as 'dyadic clefts' or just 'dyads'. Here, the LTCCs are found in close proximity to RyR channels (31, 68, 16). These are Ca^{2+}-gated Ca^{2+} channels found in clusters on the SR membrane and concentrated at the Z discs.

The small amount of Ca^{2+} released by the LTCCs activates nearby RyR channels within the dyad in a process known as 'calcium-induced calcium release' (CICR). The enclosed shape of the dyad slows diffusion to the bulk cytosol and ensures that nearby RyR channels can sense the signal.

A dyad, including contained LTCCs and RyRs, is known as a calcium release unit, also denoted CRU (CaRU). The activation of an RyR cluster, a group of densely positioned RyR channels, creates a short spike in local Ca^{2+} known as a 'calcium spark'. When RyR clusters are activated across the whole cell (some through LTCCs, some through Ca^{2+} diffusion from nearby clusters), they create a cell-wide increase in Ca^{2+} , constituting the initial phase of the 'Ca^{2+} transient' that is produced every heartbeat.

Ca^{2+} from the transient binds to troponin C (TnC), a protein bound to myofibrils, causing them, and hence the cell to contract (61). This signalling pathway is called excitation contraction coupling (ECC). Ca^{2+} reuptake into the sarcoplasmic reticulum through sarco/endoplasmic reticulum Ca^{2+} ATPase (SERCA) pumps – Ca^{2+} pumps found on the SR membrane – increases with increased cytosolic Ca^{2+} and brings Ca^{2+} concentrations back down to diastolic (resting) levels as Ca^{2+} release from RyR channels ceases.

Other Ca^{2+} pumps that affect the Ca^{2+} transient are the sarcolemmal Ca^{2+} ATPase (PMCA) and the sodium-calcium exchanger (NCX), both found on the sarcolemma. Figure 1.3 shows a schematic representation of a cardiomyocyte with the relevant Ca^{2+} channels. The mechanisms behind spark (and hence transient) termination are still under debate. Exactly what prevents further Ca^{2+} release from RyRs is still an open question (161, 69).

1.2 Cardiac hypertrophy

Hypertrophy is a phenomenon common to many cell types including muscle, kidney, and liver cells (118, 29, 48). The term refers to the enlargement of an organ through cell growth. In the heart, hypertrophy can be divided into concentric and eccentric hypertrophy.

Concentric hypertrophy describes the process whereby muscle cells grow through the addition of sarcomeres in parallel. In hearts, this means that the atrial and/or ventricular walls thicken.

Eccentric hypertrophy describes the process whereby cardiomyocytes grow through the addition of sarcomeres in series. This causes the cells to elongate resulting in larger chambers within the heart (67).

In addition to structural changes, hypertrophic cells also undergo changes to protein (including Ca^{2+} channel) expression (103, 20, 171, 50). Cardiac hypertrophy is an essential process in development and is particularly apparent during adolescence, pregnancy, and extreme athletic pursuits. Concentric hypertrophy is commonly observed in strength-based athletes, and eccentric in endurance-based athletes (94). In these cases, it is known as physiological hypertrophy, a normal form of growth.

Hypertrophy can also be a compensatory adaptation to cardiac stress – strengthening and enlarging the heart to better cope with disease. Heart disease is the most common form of death in First World countries and heart failure is one of the most common types of heart disease. Hypertrophy is known to accompany the majority of heart diseases. It may initially have a mitigating effect, but its presence has been shown to be an exacerbating factor (6). Hypertrophy may increase the heart's capacity, but hypertrophic cell growth generally won't affect the underlying causes and so ultimately cannot relieve the strain on the heart. Growth then continues and becomes detrimental to the heart's function. This increases the chance of heart failure and is known as pathological hypertrophy(98, 118).

Studying how an increase in workload for the heart translates to heart cell growth is an important step in characterising hypertrophy and identification of targets for the treatment of medical conditions. The causes and effects of hypertrophy are well documented in literature (see (51, 129, 81)), but the underlying mechanisms are not as well understood.

One of the biggest questions revolves around Ca^{2+}'s simultaneous involvement in the hypertrophic process as a secondary messenger, simultaneous to its role in cell contraction. This thesis is concerned with the role of Ca^{2+} signalling in the dynamics of the eccentric, pathological, left ventricular hypertrophic signalling pathway.

1.2.1 The hypertrophic signalling pathway

Pathological hypertrophy is initiated through the CnA/NFAT pathway (98, 51). This pathway is initiated when G protein-coupled receptors on the cell membrane recognise an external signal such as endothelin 1 (ET-1), angiotensin II, or a catecholamine. These receptors are also coupled with phospholipase C, an enzyme which facilitates the generation of diacylglycerol (DAG) and inositol 1,4,5-trisphosphate, also referred to as '$InsP_3$' (IP_3) through hydrolysis of phosphatidylinositol 4,5-biphosphate. DAG binds to and activates protein kinase C (PKC) which alters myofilament contractility.

IP_3 is a secondary messenger that activates the IP_3R on the SR membrane, potentially altering the normal Ca^{2+} dynamics of the cardiomyocyte. This could potentially lead to dephosphorylation of NFAT in the cytosol (with the aid of calmodulin and calcineurin A), and its subsequent translocation to the nucleus (157, 104, 117), via the pores in the nuclear envelope, as well as activation of calmodulin kinase II (CaMKII), a protein linked to gene regulation in cardiac hypertrophy (172, 28). CAMKII phosphorylates histone deacetylase 5 (HDAC5), exporting it from the nucleus (91, 165). Removal of HDAC5, which represses the genes for hypertrophy, together with the presence of NFAT in the nucleus, initiates hypertrophic gene transcription and, hence, cell restructuring (107).

Without the presence of nuclear Ca^{2+} removing HDAC5, NFAT is unable to activate the genes for hypertrophy. Nuclear CnA and calmodulin phosphorylate NFAT and the phosphorylated NFAT is then transported back out of the nucleus, preventing the activation of the hypertrophic pathway. The rate of phosphorylation/dephosphorylation varies between NFAT isoforms (64), and different patterns of Ca^{2+} release (149, 49). However, studies performed on genetically modified mouse models have shown that the NFATc3 (NFAT4) isoform in particular is necessary for the pathological hypertrophic pathway (158, 159). Understanding the initiating Ca^{2+} dynamics in both the cytosol and nucleus of

heart cells is therefore essential to our understanding of NFAT4 activation and the CnA/NFAT pathway.

1.3 The role of IP_3Rs in cardiomyocyte calcium dynamics

1.3.1 Cytosolic calcium

IP_3Rs are found in clusters near dyads on the sarcoplasmic reticulum (junctional SR/jSR) (78, 50) and on the nuclear envelope (3, 160). In ventricular myocytes, the expression level of IP_3Rs is far lower than that of RyRs (101, 11, 50). Experimental studies involving stimulation of healthy ventricular myocytes with IP_3 generally report an increase in spontaneous Ca^{2+} transients and/or an increase in transient amplitude (113, 30). However, there are also many studies that report no significant increase in amplitude (87, 173, 50) (Summarised in Table 2.1).

The main hypotheses for alteration to the Ca^{2+} transient to convey hypertrophic signalling were oscillation frequency and amplitude (7). Whether the change to the shape of the Ca^{2+} transient (amplitude or duration), transient frequency, or a persistent rise in the base Ca^{2+} concentration in the cytosol leads to hypertrophy, is still unclear (161). It has been shown that while constant elevated calcium ion (Ca^{2+}) concentration, $[Ca^{2+}]$, will activate NFAT, $[Ca^{2+}]$ oscillations are a more efficient method of transmitting the hypertrophic signal and Ca^{2+} dynamics below a certain threshold have little to no effect on NFAT activity (149). The Ca^{2+} release from IP_3Rs augments the beat to beat $[Ca^{2+}]$ oscillations; modifying their shape, and potentially the base level of Ca^{2+} in the cytosol. Slow binding Ca^{2+} sites on CnA allow it to act as a low pass filter (124), so that only these altered $[Ca^{2+}]$ oscillations lead to activation of the NFAT pathway. A recent experimental study in HeLa cells demonstrates that the 'duty cycle' of $[Ca^{2+}]$ oscillations has a greater effect than either maximum concentration or frequency (49). In their paper, Hannanta-anan and Chow (49) define duty cycle as either the Ca^{2+} concentration integrated over time then divided by the maximum concentration and period, or the transient duration divided by the period. Whether the change to the shape of the Ca^{2+} transient (amplitude or duration), transient frequency, or a persistent rise in the base Ca^{2+} concentration in the cytosol leads

to hypertrophy, is still unclear (161). In ventricular heart cells, where the period is determined by pacemaker cells in the sinoatrial node, and assuming cardiac hypertrophy is not heralded by arrhythmias, this implies that the most important aspect of hypertrophic Ca^{2+} dynamics is the duration of each oscillation, presumably the duration over a threshold concentration. This hypothesis has not yet been verified in cardiac cells and will be explored further in Chapter 2.

1.3.2 Nuclear calcium

Relatively little is currently known about nuclear calcium: how, when, and why nuclear Ca^{2+} transients occur is still not completely understood. Channels on the nuclear envelope can allow Ca^{2+} entrance and exit to both the nucleus and the intermembrane space. IP_3R channels in the nuclear membrane release Ca^{2+} into the perinuclear region and the nucleus from the nuclear envelope (165). Additionally, there are large pores in the nuclear envelope, regulated by protein complexes, known as Nuclear Pore Complexes (NPCs). NPCs are permeable to any solutes smaller than approximately 20kDa, meaning that calcium ions can diffuse through them (43, 56). There is evidence that Ca^{2+} concentrations at the nuclear envelope affect the permeability of NPCs (43).

Ca^{2+} does not diffuse far within cells due to its high reactivity with numerous intracellular proteins and other molecules i.e. cytosolic Ca^{2+} is highly buffered. This means that only Ca^{2+} events within 3μm of the perinuclear region have any significant effect on nuclear [Ca^{2+}] levels (77). This includes Ca^{2+} transients. Due to these factors, Ca^{2+} concentrations within the nucleus are highly dependent on cytosolic Ca^{2+} dynamics. Ca^{2+} diffuses slower through the nuclear space than through the cytosol (39), and the lingering nature of nuclear Ca^{2+} transients may allow the nucleus to serve as a "Ca^{2+} tunnel" – letting nearby signals spread more rapidly throughout the cytosol (77).

Experiments have shown the nuclear envelope to filter high frequency oscillations in Ca^{2+} concentration but transmit sustained [Ca^{2+}] increase (19). It is known that the periodic spikes in nuclear [Ca^{2+}] from excitation contraction coupling (ECC) signals do not activate the hypertrophic pathway (79, 165). However, understanding these mechanisms could help to understand how the hypertrophic signal enters the nucleus (71). Studying the mechanisms involved will give us

further insight into the interplay between hypertrophic and contraction signals, and, potentially the means by which the cell distinguishes them.

1.4 The role of modelling in calcium dynamics

Experimental methods have progressed to the point where we can view the workings of cells in amazing detail – the precise ultrastructure and distribution of organelles, intracellular transport in real-time. However, knowing *what* is happening does not always explain *how* it is happening. Confocal microscopy and, more recently, superresolution microscopy technologies have given us a wealth of information on intracellular structures. Similarly, other *in vitro* experiments have been able to tell us much about the function and distribution of major proteins and channels within the cell. However, there are still many facets of biology that can only be explained with the help of a mathematical model. Mathematical models help us to understand not only what we have witnessed in experiments but also the implications of these results and the physical limits of each system. This thesis contains mathematical models of the cardiomyocytes and their Ca^{2+} dynamics developed to better understand the hypertrophic pathway.

Heart cells contain numerous different types of Ca^{2+} channels, many of which will not be covered here. We are primarily interested in those most involved in the hypertrophic pathway, specifically RyR channels and IP_3R channels. Both channels are Ca^{2+} activated and allow calcium ions from the sarcoplasmic reticulum, or nuclear envelope, to enter the cytosol when opened. They share many similarities but differ in their activation conditions and purpose.

1.4.1 Modelling RyRs and the CaRU

RyR channels have been the focus of numerous models (22, 169, 170, 141) and are often modelled as part of the calcium release unit (138, 46). Due to their crucial role in RyR activation, models of the gating properties of LTCCs and the influence of their location in the dyadic cleft are necessarily included. A particularly influential model in this area was that of Stern et al. (140), which showed that previous common (Ca^{2+}) pool models could not be consistent with the positive feedback loop created by calcium-induced calcium release. Instead, we need to

consider Ca^{2+} within t-tubules and the junctional sarcoplasmic reticulum (jSR) separately to the rest of the sarcoplasmic reticulum, and take into account the flow of Ca^{2+} within the sarcoplasmic reticulum. Further noteworthy models include those of Sobie et al. (138) who created a cytosolic $[Ca^{2+}]$ model which incorporates both coupled RyR gating, where nearby RyR channels affect each other's gating behaviour, and jSR regulated gating to produce robust spark termination; and Hinch (54), who with the use of fast equilibrium approximations, produced a greatly simplified model of cell-wide ECC while preserving the dyadic interaction between LTCCs and RyRs.

1.4.2 Modelling IP_3R channels

A plethora of IP_3R models have also been created over the last few decades. However, there are currently no combined models of IP_3Rs and their interactions with other Ca^{2+} channels in cardiac cells. This is primarily because of the key role of IP_3R in Ca^{2+} signalling in non-cardiac cell types where the Ca^{2+} concentration is more constant. One of the aims of this thesis is to incorporate IP_3Rs into a model of cardiac Ca^{2+}.

The open probability of IP_3R channels increases in the presence of IP_3, Ca^{2+}, and ATP. Experiments have shown intracellular Ca^{2+} channels exhibit a bimodal dependence on Ca^{2+}, with one mode having a much higher open probability for the channel (133, 119, 134, 135). Increased Ca^{2+} levels cause a shift to this mode; however, at higher concentrations, calcium ions also inhibit the opening of IP_3R channels, and they shift back to their resting mode. The channel can open in either mode. The resting mode is when the channel is mostly closed with short fluctuations to open and back. In the activated mode, the channel remains open for much longer periods.

It has been hypothesised that the inhibitory binding site has a much lower binding affinity than the activation site, due to the delay between activation and inhibition by Ca^{2+} (32). An early model of IP_3R channel gating by De Young and Keizer (167) incorporated this and introduced the idea that each subunit of an IP_3R channel had two activating sites, one for each of IP_3 and Ca^{2+}, as well as an inhibitory binding site for Ca^{2+}. Rate constants estimated from experimental

data were then used to describe the binding of these sites. Whilst these models have since been updated and improved upon, the ideas behind them remain central to many of our current models of IP_3R channels.

Stochastic models of IP_3R channel gating (145, 99) were created in the late 1990s, and were derived from the De Young-Keizer model. The number of Ca^{2+} binding sites in each model differed from each other, but both managed to more accurately replicate the observed fluctuations in channel opening than previous deterministic models. More complicated models include not only the chemical binding rates, but also the allosteric (conformation) shifts of channel proteins (69), as well as multi-channel cluster/cell and $[Ca^{2+}]$ wave models (33, 34, 131, 132, 143). Shuai et al. (130) review stochastic gating models based on the De Young-Keizer model, and while their gating characteristics are more consistent with data, the question of how to model Ca^{2+} transient termination in these models is still unresolved (119).

Later models such as those by Ionescu et al. (60), Ullah et al. (151) and Siekmann et al. (133) focus more on the modal gating of the channels i.e. the modes mentioned in Siekmann et al. (133). In these, the behaviour within each mode is not affected by the concentrations of local chemical species; rather, the likelihood of the channel being in each mode is influenced. The latter two in particular place much less emphasis on kinetic binding and the mechanisms of channel activation, and more on the statistical properties of the data. This allows for more accurate models of when and for how long IP_3R channels will open with fewer parameters. However, the significance of the results of these models has not yet been fully realised.

The Siekmann et al. (133) model was combined with the idea of 'dynamic models' (37), delayed channel reactions to changes in local concentrations, by Cao et al. (17) and later Sneyd et al. (137).

1.4.3 Models of hypertrophic calcium signalling

There are no current models of hypertrophic Ca^{2+} dynamics in cardiomyocytes. Hohendanner et al. (56) developed a preliminary whole cell cardiac model of the

Ca^{2+} dynamics in the cytosol and nucleus due to ECC signalling in rabbit ventricular myocytes however the model did not investigate Ca^{2+} translocation into or within the nucleus.

Johny et al. (63) created a model of cytosolic Ca^{2+}, IP_3R and RyR interactions in vascular smooth muscle cells. The model combined a number of existing models, including the IP_3R cluster model of Swillens et al. (146). Thorough analysis revealed the most important components of the Ca^{2+} machinery in determining smooth muscle Ca^{2+} dynamics. However, the channel concentrations and isoforms in smooth muscle are not similar enough to cardiac cells for this model to be immediately applicable.

Cooling et al. (23, 25) developed models of ET-1-generated IP_3 transients and the sensitivity of NFAT to cytosolic Ca^{2+} transients in the context of hypertrophy. However, they did not couple either of these with the cardiac Ca^{2+} machinery.

There is a clear gap in the literature on the intracellular mechanisms and effect of IP_3R channel activation on cardiac Ca^{2+} dynamics.

1.4.4 NFAT models

Nuclear factor of activated T cells (NFAT) dephosphorylation and translocation within the cardiac cell has received relatively little attention in the scientific literature. While there have been several knockout studies examining the necessity of the various NFAT isoforms in cardiac hypertrophy, there are few that have examined the conditions necessary for NFAT activation and translocation to the nucleus – due in part to the difficulty in tracking NFAT movement in cardiac cells.

However, there are several models of CnA/NFAT signalling, developed using the available experimental data. Saucerman and Bers (124) developed a model of calmodulin, CaMKII, and CnA in rabbit ventricular myocytes that coupled with the Shannon-Bers ventricular myocyte Ca^{2+} model (126, 127). It modelled the effects of the excitation contraction coupling signal on the activity of these three proteins in the CnA/NFAT pathway in both the dyad and general cytosol, determining that the sensitivity and availability of calmodulin were integral in differentiating between excitation contraction coupling (ECC) and hypertrophic

Ca^{2+} signals.

Cooling et al. (25) created a four state NFAT model, mediated by CnA and Ca^{2+}. It tracked the proportion of NFAT in the dephosphorylated (DNA-ready) state within the cytosol and nucleus respectively as well as the phosphorylated state within each of the cytosol and nucleus. The model was fitted to skeletal muscle and baby hamster kidney cell data. The model was then simulated with $[Ca^{2+}]$ oscillations of varying mean and frequency and was shown to be responsive to both a relatively flat, IP_3R generated Ca^{2+} signal and $[Ca^{2+}]$ oscillations simulating ECC and this signal combined, i.e. a low pass filter.

Bazzazi et al. (5) performed novel calcineurin A imaging experiments in both neonatal rat and adult guinea pig ventricular myocytes. Using their imaging results and a simplified version of the Saucerman and Bers (124) CaM/CaMKII/CnA model, they developed a model of CnA activation – extrapolating the Ca^{2+} and Ca^{2+}/CaM binding rates. This model was built on by Kar et al. (65), who investigated the differing behaviour of NFAT1 and NFAT4 isoforms in HEK293 cells in responce to varying Ca^{2+} signals. They demonstrated experimentally that NFAT1 was slower to activate but only needed a local rise in $[Ca^{2+}]$ from store-operated Orai1 channels whereas NFAT4 required both a local Ca^{2+} signal and a nuclear Ca^{2+} signal for activation.

Building on the work of both Saucerman and Bers (124) and Bazzazi et al. (5), Kar et al. (65) simulated calcineurin A accumulation in the nucleus based on their experimentally measured levels of $[Ca^{2+}]$ in the nucleoplasm of HEK293 cells. Their four-state NFAT model implies that nuclear calcineurin A concentrations oscillate in a similar pattern to nuclear Ca^{2+} concentrations and that $[Ca^{2+}]$ oscillations are far more effective at activating calcineurin A than constant low level Ca^{2+}.

There is yet to be a complete model of the CnA/NFAT pathway from IP_3R-mediated Ca^{2+} dynamics to NFAT activity in the nucleus.

Chapter 2

The role of IP_3R in cardiac hypertrophic signalling

Calcium plays a central role in mediating both contractile function and hypertrophic signalling in ventricular cardiomyocytes. Several hypotheses as to how the modified calcium transient carries the hypertrophic signal have been proposed, including changes to amplitude, duration, duty cycle, and signal localisation.

Here we use mathematical modelling to investigate the possible mechanisms given current knowledge of inositol 1,4,5-trisphosphate receptors (IP_3Rs), cardiac excitation contraction coupling (ECC) machinery, and the sensitivity of downstream proteins in the hypertrophic signalling pathway to calcium. To our knowledge, no such model of the interactions necessary to generate this signal in cardiac cells currently exists.

We develop a model describing the effect of functional interaction (crosstalk) between RyR and IP_3R channels on the calcium transient. We examine the sensitivity of the calcium transient to the properties of IP_3R activation. A key result of our study is that IP_3R activation increases calcium transient duration but its effect on the amplitude of the calcium transient is IP_3-dependent. We further demonstrate that IP_3-mediated Ca^{2+} release in the cytosol is capable of increasing the duty cycle of the cytosolic calcium transient across a broad range of parameter values and IP_3 concentration. These findings suggest increased Ca^{2+} duty cycle as a plausible mechanism for IP_3-dependent hypertrophic signalling in ventricular cardiomyocytes.

The material in this chapter is reproduced from a publication titled '*IP_3R Ca^{2+} release shapes cytosolic Ca^{2+} transients for hypertrophic signalling in ventricular cardiomyocytes*' which is currently in review at *Biophysical Journal*.

2.1 Introduction

In this study we have taken the experimental studies on rat ventricular cardiomyocytes as a reference point for the observed effects of IP_3R activation on cellular Ca^{2+} dynamics and extended a well-established model of beat-to-beat cytosolic Ca^{2+} transients in cardiac cells (55, 147) to include a model of IP_3R (137) channels.

This deterministic, compartmental model of cardiac excitation contraction coupling enables us to investigate how IP_3R activation could affect Ca^{2+} dynamics at the whole cell scale, while avoiding the computational complexity associated with detailed stochastic and spatial modelling. Specifically, it enables us to explore the parameter ranges of IP_3R-mediated Ca^{2+} release that modify the global cytosolic Ca^{2+} transient.

A number of transcription factors serve to transduce changes in Ca^{2+} to activation of hypertrophic gene transcription. Of particular note is the nuclear factor of activated T-cells (NFAT). There are five known NFAT isoforms expressed in mammals, four of these are found in cardiac cells (152, 158). NFAT isoforms are known to have redundant, overlapping functions however NFAT1 (15) and NFAT4 (158) have been shown to be necessary in the mouse pathological hypertrophy pathway.

Several studies have focused on characterising the Ca^{2+} dynamics necessary to activate NFAT and initiate hypertrophy (149, 21, 117, 166, 49, 65) and have shown NFAT to be a Ca^{2+} signal integrator (149). Furthermore, a recent study by Hannanta-anan and Chow (49) used direct optogenetic control of cytosolic Ca^{2+} transients in HeLa cells to demonstrate that the transcriptional activity of NFAT4 can be up-regulated by increasing the residence time of Ca^{2+} in the cytosol within each oscillation. The increased residence time of Ca^{2+}, also referred to as 'duty cycle' is the ratio between the area under the Ca^{2+} transient curve divided by the maximum possible area as calculated by the product of transient amplitude and period (see Figure 2.1A). Note that area under the curve is calculated as the integral of the $[Ca^{2+}]$ over time. Their study showed that increasing the duty

Experimental data on hypertrophy and IP_3

Cell State		IP_3	ET-1
Rat	Amplitude:	▲(113)	▲(113) ◆(53)
	Duration:	–	–
	Basal Ca^{2+}:	–	–
	SCTs:	▲(113) ▲(50)	▲(113) ▲(50)
Other species	Amplitude:	▲(136)	▲(136) ▲(136)
	Duration:	–	–
	Basal Ca^{2+}:	▲(30)	▲(136) ▲(27)
	SCTs:	–	▲(136) ▲(136)

Table 2.1: Summary of experimentally observed changes to the Ca^{2+} transient of ventricular myocytes in rat and other species following addition of IP_3 and ET-1. SCTs stands for spontaneous Ca^{2+} transients. ▲ indicates an increase, ▼ a decrease, and ◆ no significant change reported. Colours indicate species (rat, rabbit, human, and mouse). Dashes indicate no data found.

cycle had a proportionally greater effect on NFAT transcriptional activity than changing either the frequency or amplitude of the cytosolic $[Ca^{2+}]$ oscillations. This suggests an increased Ca^{2+} duty cycle as a possible mechanism by which Ca^{2+} release through IP_3R channels can effect hypertrophic signalling.

Using an extended mathematical model of beat-to-beat cytosolic Ca^{2+} transients and IP_3R channels we show that IP_3R activation in the cytosol can increase the cytosolic $[Ca^{2+}]$ duty cycle, and thus provide a plausible mechanism for activating NFAT transcription in the cardiac cell.

We establish model feasibility through conducting parameter sensitivity analysis and comparing our simulation analysis to published experimental data summarised in Table 2.1. We show the conditions necessary for IP_3R channels to alter Ca^{2+} transient amplitude, width, basal Ca^{2+} and duty cycle.

2.2 Methods

We developed a computational model of RyR and IP_3R mediated Ca^{2+} fluxes in the cardiac cell. Model simulations were performed using the ode15s ODE solver from MATLAB 2017b (The MathWorks Inc., Natick, Massachusetts) with relative and absolute tolerances 1×10^{-3} and 1×10^{-6} respectively. Model code can be found at https://github.com/CellSMB/compartmental_ECC_ETC. $[Ca^{2+}]$ within cardiomyocytes is essentially a periodic function of time. To model the

long term changes to the Ca^{2+} transient after altering the model, e.g increasing the simulated [IP_3], we start our simulations with physiological initial conditions (stable initial conditions in our base model, without IP_3Rs) and simulate each subsequent transient with different initial conditions generated by the previous transient.

The model was paced until the normalised root mean square deviation (NRMSD) between each subsequent beat was below 1×10^{-3} ($<\approx 1\%$ of the minimum output), and all but the last oscillation discarded to eliminate short-term behaviours (e.g. the larger transient immediately after [IP_3] is increased in Figure 2.1B). Initial conditions were set to the basal Ca^{2+} level of the model at dynamic equilibrium with inactive IP_3R channels, determined after running the base model until the NRMSD was also below 1×10^{-3} (as before, $<\approx 1\%$ of the minimum output). The model equations were simulated at 1 Hz, the original pacing frequency of the Hinch et al. (55) model and at 0.3 Hz which is another common pacing frequency in experimental studies of IP_3 and Ca^{2+} in cardiomyocytes (113, 50).

2.2.1 Model Equations

We constructed a compartmental model of rat left ventricular cardiac myocyte Ca^{2+} dynamics based on the Hinch et al. (55) model of excitation contraction coupling with the addition of IP_3R Ca^{2+} release modelled using the Siekmann-Cao-Sneyd model (137) as well as a rapid buffering term (155) to account for fluorescent indicators used in experiments. In this chapter, the parameters were specifically chosen to simulate Fluo-4AM. The Hinch model is an established whole cell model of rat cardiac Ca^{2+} dynamics that describes the flux through the major Ca^{2+} channels and pumps on the cell and sarcoplasmic reticulum (SR) membranes and the effects of applying a voltage across the cell membrane. The parameters for the Hinch component of our model were maintained from the original except for those of the periodic driving voltage/membrane depolarisation, V, the duration of which was shortened to better approximate the rat action potential (110) (see Figure 2.2). V initiates each Ca^{2+} transient within the system.

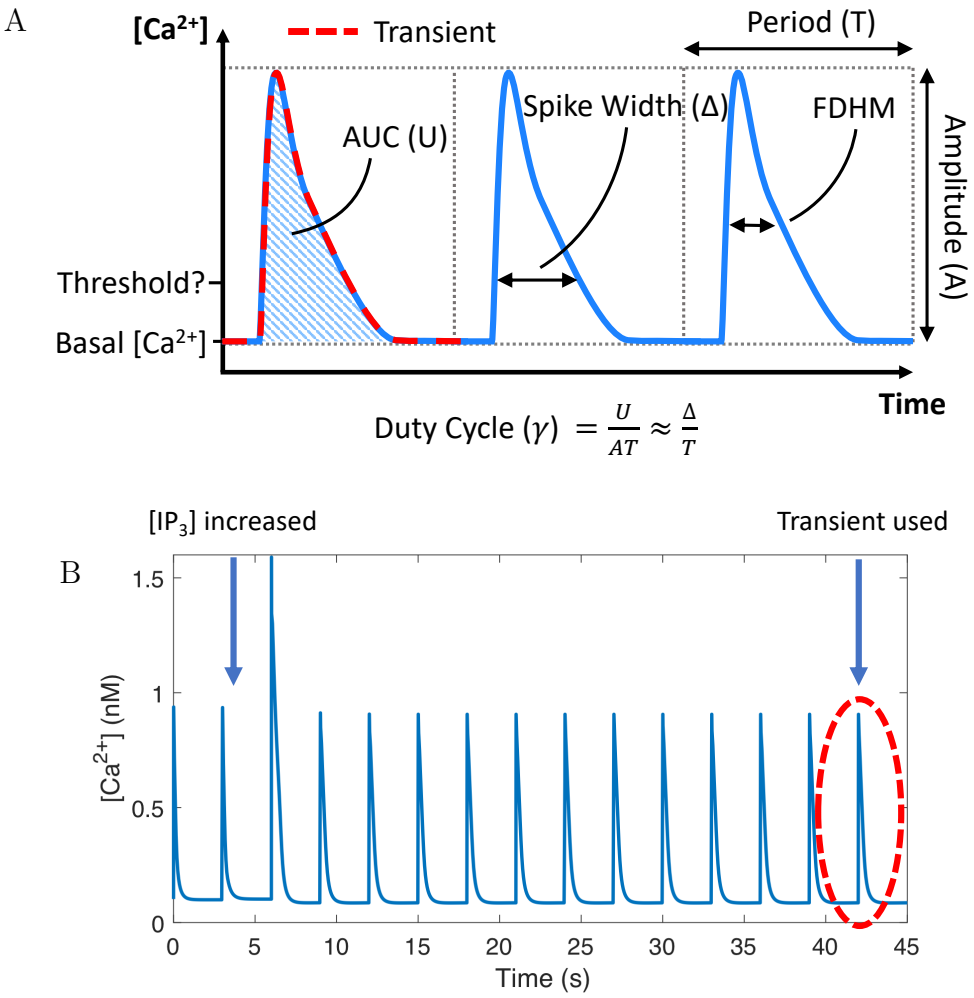

Figure 2.1: (A) Representative cytosolic Ca^{2+} concentration as a function of time, indicating the transient duty cycle, a function of the area under the curve (U), amplitude, and period. (B) Example of Ca^{2+} transients generated by the model.

The $[Ca^{2+}]$ in the cytosol is governed by the following ordinary differential equation:

$$\frac{\mathrm{d}[Ca^{2+}]_{cyt}}{\mathrm{d}t} = \beta_{fluo} \cdot \beta_{CaM} \cdot (J_{CaL} + J_{RyR} - J_{SERCA} + J_{IP_3R} + J_{other}) \tag{2.1}$$

$$J_{other} = J_{SRl} + J_{NCX} - J_{PMCA} + J_{CaB} + J_{TnC} \tag{2.2}$$

A small Ca^{2+} flux through the LTCCs, J_{CaL}, activates RyR channels to release Ca^{2+} from the sarcoplasmic reticulum into the cytosol at a rate of J_{RyR}. Ca^{2+} is

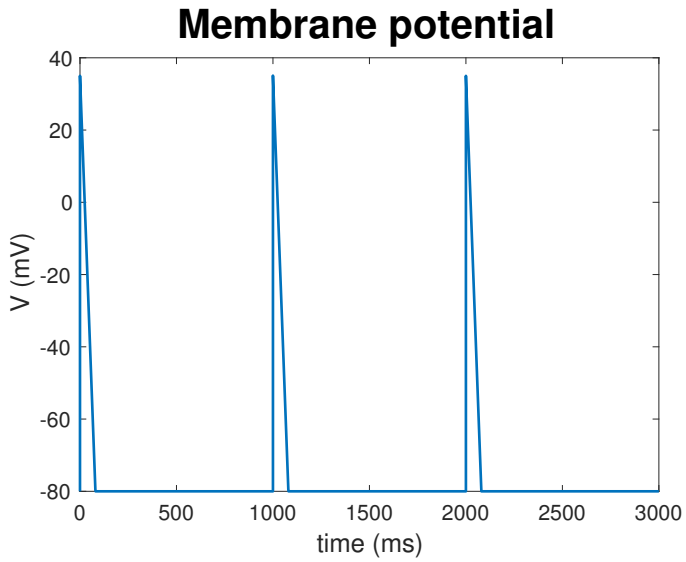

Figure 2.2: Membrane depolarisation as a function of time. Cardiomyocyte membrane depolaristion initiates each Ca^{2+} transient and determines the period of $[Ca^{2+}]$ oscillation.

resequestered into the sarcoplasmic reticulum by SERCA at a rate J_{SERCA}. β_{fluo} is the rapid buffer coefficient (155) for the fluorescent dye in the cytosol, as used to detect $[Ca^{2+}]$ in *in vitro* experiments, and β_{CaM} is the rapid buffer coefficient for calmodulin in the cytosol. J_{other} includes Ca^{2+} fluxes such as exchange with the extracellular environment through the sodium-calcium exchanger, J_{NCX}; sarcolemmal Ca^{2+}-ATPase, J_{PMCA}; and the background leak, J_{CaB}; as well as the SR leak, J_{SRl}; and buffering on troponin C, J_{TnC}.

When the simulation is run with IP_3 present, there is additionally a flux through the IP_3Rs :

$$J_{\text{IP}_3\text{R}} = \frac{k_f \cdot N_{\text{IP}_3\text{R}} \cdot P_{\text{IP}_3\text{R}} \cdot \left([Ca^{2+}]_{\text{SR}} - [Ca^{2+}]_{\text{cyt}}\right)}{M_{\text{myo}}} \tag{2.3}$$

Here k_f is the maximum total flux through each IP_3R channel, this was chosen to be 0.45 $\mu m^3 ms^{-1}$ unless otherwise stated to create a measurable effect on IP_3R channel activation while maintaining plausible total flux. $N_{\text{IP}_3\text{R}}$ is the number of IP_3R channels in the cell, this was set to 1/50th of the number of RyR channels (101). M_{myo} is the volume of the cell. $[Ca^{2+}]_{\text{cyt}}$ and $[Ca^{2+}]_{\text{SR}}$ are the Ca^{2+} concentrations in the cytosol and sarcoplasmic reticulum respectively.

$P_{\text{IP}_3\text{R}}$ is the $[Ca^{2+}]$ and $[IP_3]$ dependent open probability of the IP_3R channels, and is determined using the Siekmann-Cao-Sneyd model (133, 18, 137), which has

an in-built delay in response to changing Ca^{2+} concentration, along with several parameters governing channel activation and inactivation. This model describes P_{IP_3R} as

$$P_{IP_3R} = \frac{\beta}{\beta + k_\beta \cdot (\beta + \alpha)} \tag{2.4}$$

where k_β is a transition term derived from single channel data analysis Siekmann et al. (133), β describes the proportional rate of activation and α the rate of inactivation of the IP_3R channels:

$$\beta = B \cdot m \cdot h \tag{2.5}$$

$$\alpha = (1 - B) \cdot (1 - m \cdot h_\infty) \tag{2.6}$$

where h is time-dependent, and B, m, and h_∞ describe the dependence on IP_3, the dependence on Ca^{2+}, and the Ca^{2+}-dependent delay in IP_3R gating, respectively. Expressions for these variables are as follows:

$$B = \frac{[IP_3]^2}{K_p^2 + [IP_3]^2} \tag{2.7}$$

$$m = \frac{[Ca^{2+}]^4_{cyt}}{K_c^4 + [Ca^{2+}]^4_{cyt}} \tag{2.8}$$

$$\frac{dh}{dt} = \frac{(h_\infty - h) \cdot \left(K_t^4 + [Ca^{2+}]^4_{cyt}\right)}{t_{max} \cdot K_t^4} \tag{2.9}$$

$$h_\infty = \frac{K_h^4}{K_h^4 + [Ca^{2+}]^4_{cyt}} \tag{2.10}$$

Here K_c and K_h are parameters which determine the Ca^{2+}-dependence of IP_3R channel open probability, while K_t and t_{max} are parameters which affect the delay in IP_3R response to cytosolic changes. K_t determines the influence of $[Ca^{2+}]$ on the delay, while t_{max} is a temporal scaling factor for the reaction of IP_3Rs to changes in $[Ca^{2+}]$. K_p is the parameter that determines the IP_3-dependence of IP_3R channel behaviour. While these parameters have been fitted to data for type I IP_3Rs in Sneyd et al. (137), their values in type II IP_3Rs in rat ventricular cardiomyocytes have yet to be determined.

Several experimental studies have investigated IP_3R activity across a range of Ca^{2+} concentrations with 1 μM IP_3 (116, 38). These studies suggest that IP_3R channels would be open, with almost constant P_{IP_3R} over the full range of cytosolic

Ca^{2+} concentrations experienced during excitation contraction coupling in the cardiomyocyte. An IP_3R-facilitated SR-Ca^{2+} leak has been reported to amplify systolic concentrations (175, 13) as seen in most published experiments of IP_3 enhanced Ca^{2+} transients tabulated in Table 2.1. Through parameter sensitivity analysis of this model, in comparing Figure 2.4 and e.g. Figure 2.5 we find that in order to be consistent with these observations P_{IP_3R} must be significantly smaller at resting Ca^{2+} concentrations than that at higher concentrations.

The rest of the equations are as in the Hinch model. The ODEs for the other model compartments are described as follows

$$\frac{\mathrm{d}[Ca^{2+}]_{SR}}{\mathrm{d}t} = \frac{M_{myo}}{M_{SR}} \cdot (-J_{RyR} + J_{SERCA} - J_{SRl} - J_{IP_3R}) \tag{2.11}$$

$$\frac{\mathrm{d}CaTnC}{\mathrm{d}t} = J_{TnC} \tag{2.12}$$

Here M_{SR} refers to the volume of the sarcoplasmic reticulum, and $CaTnC$ the concentration of Ca^{2+}-bound troponin.

The Ca^{2+} release unit model

In order to simulate the Ca^{2+} released from the sarcoplasmic reticulum, we use the reduced, Hinch et al. (55) model of the CaRU as described in Yu et al. (168). The CaRU is modelled as having four states, z_1, z_2, z_3, z_4, each describing a different combination of an LTCC and an RyR channel being either active (opening and closing) or inactive (closed until activated). In z_1, both RyRs and LTCCs are active. In z_2, only LTCCs are active. In z_3, only RyRs are active. In z_4, both RyRs and LTCCs are inactive. J_{Li} and J_{Ri} are the total flux through the LTCCs and RyRs in state i respectively. The nine state model (with LTCCs and RyRs in switching between open, close, and inactive states), as well as its reduced four state version and the transition rates between states are depicted in Figure 2.3. These equations are detailed below.

$$J_{CaL} = \frac{N}{M_{myo}} \cdot (z_1 \cdot J_{L1} + z_2 \cdot J_{L2}) \tag{2.13}$$

$$J_{RyR} = \frac{N}{M_{myo}} \cdot (z_1 \cdot J_{R1} + z_3 \cdot J_{R3}) \tag{2.14}$$

where N is the number of RyRs in the cardiomyocyte.

$$J_{L1} = J_{Loo} \cdot y_{oo} + J_{Loc} \cdot y_{oc} \tag{2.15}$$

$$J_{L2} = \frac{J_{Loc} \cdot \alpha_p}{\alpha_p + \alpha_m} \tag{2.16}$$

$$J_{R1} = y_{oo} \cdot J_{Roo} + J_{Rco} \cdot y_{co} \tag{2.17}$$

$$J_{R3} = \frac{J_{Rco} \cdot \beta_{pcc}}{\beta_m + \beta_{pcc}} \tag{2.18}$$

where the CaRU fluxes through each of the channels, in each state are described as:

$$J_{Rco} = \frac{J_R \cdot \left([\mathrm{Ca}^{2+}]_{\mathrm{SR}} - [\mathrm{Ca}^{2+}]_{\mathrm{cyt}}\right)}{g_D + J_R} \tag{2.19}$$

$$J_{Roo} = \frac{J_R \cdot \left([\mathrm{Ca}^{2+}]_{SR} - [\mathrm{Ca}^{2+}]_{\mathrm{cyt}} + \frac{\frac{J_L}{g_D} \cdot 2\kappa}{1-e^{-2\kappa}} \cdot \left([\mathrm{Ca}^{2+}]_{SR} - [\mathrm{Ca}^{2+}]_o \cdot e^{-2\kappa}\right) \right)}{1 + \frac{J_R}{g_D} + \frac{\frac{J_L}{g_D} \cdot 2\kappa}{1-e^{-2\kappa}}} \tag{2.20}$$

$$J_{Loc} = \frac{\frac{J_L \cdot 2\kappa}{1-e^{-2\kappa}} \cdot \left([\mathrm{Ca}^{2+}]_o \cdot e^{-2\kappa} - [\mathrm{Ca}^{2+}]_{\mathrm{cyt}}\right)}{1 + \frac{J_L}{g_D} \cdot \frac{2\kappa}{1-e^{-2\kappa}}} \tag{2.21}$$

$$J_{Loo} = \frac{\frac{J_L \cdot 2\kappa}{1-e^{-2\kappa}} \cdot \left([\mathrm{Ca}^{2+}]_o \cdot e^{-2\kappa} \cdot \left(1 + \frac{J_R}{g_D}\right) - [\mathrm{Ca}^{2+}]_{\mathrm{cyt}} - \frac{J_R}{g_D} \cdot [\mathrm{Ca}^{2+}]_{SR} \right)}{1 + \frac{J_R}{g_D} + \frac{J_L}{g_D} \cdot \frac{2\kappa}{1-e^{2\kappa}}} \tag{2.22}$$

$$\text{where } \kappa = \begin{cases} \kappa & |\kappa| > \frac{1}{2} \times 10^{-5} \\ \frac{1}{2} \times 10^{-5} & \text{otherwise} \end{cases}$$

where

$$\kappa = \frac{FV}{RT} \tag{2.23}$$

$$\tag{2.24}$$

F being the Faraday constant, V the voltage across the cell membrane, described later, R the gas constant and T the temperature. We denote the $[\mathrm{Ca}^{2+}]$ outside the cell as $[\mathrm{Ca}^{2+}]_o$. g_D is . The thresholds here were primarily to avoid numerical

errors when solving in OpenCOR (168) and are generally not necessary in Matlab.

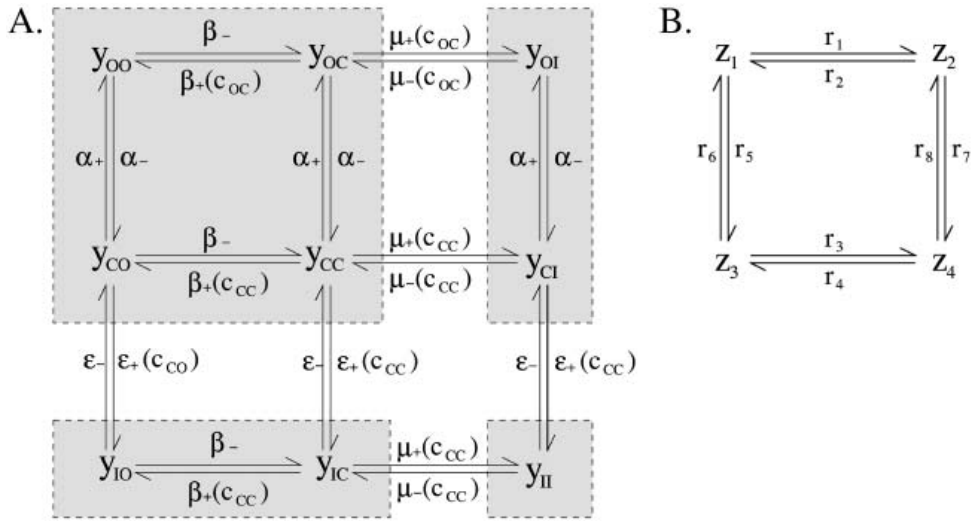

Figure 2.3: Calcium release unit, also denoted CRU dtates and transition times in the Hinch et al. (55) model. (A) The nine-state model. For each state y_{ij}, LTCC is in state i and RyR is in state j. The transitions are a function of $[Ca^{2+}]_{myo}$. (B) The reduced four-state model obtained by approximating the opening-closing times in the nine-state model as rapid in comparison to the activation-inactivation transitions. Reproduced from Hinch et al. (55), with permission from Elsevier.

The CaRU transitions between states at the following rates:

$$\frac{dz_1}{dt} = -(r_1 + r_5) \cdot z_1 + r_2 \cdot z_2 + r_6 \cdot z_3 \tag{2.25}$$

$$\frac{dz_2}{dt} = r_1 \cdot z_1 - (r_2 + r_7) \cdot z_2 + r_8 \cdot z_4 \tag{2.26}$$

$$\frac{dz_3}{dt} = r_5 \cdot z_1 - (r_6 + r_3) \cdot z_3 + r_4 \cdot z_4 \tag{2.27}$$

$$z_4 = 1 - z_1 - z_2 - z_3 \tag{2.28}$$

The transition rates, r_i, are defined as:

$$r_1 = y_{oc} \cdot \mu_{poc} + y_{cc} \cdot \mu_{pcc} \tag{2.29}$$

$$r_2 = \frac{\alpha_p \cdot \mu_{moc} + \alpha_m \cdot \mu_{mcc}}{\alpha_p + \alpha_m} \tag{2.30}$$

$$r_3 = \frac{\beta_m \cdot \mu_{pcc}}{\beta_m + \beta_{pcc}} \tag{2.31}$$

$$r_4 = \mu_{mcc} \tag{2.32}$$

$$r_5 = y_{co} \cdot \epsilon_{pco} + y_{cc} \cdot \epsilon_{pcc} \tag{2.33}$$

$$r_6 = \epsilon_m \tag{2.34}$$

$$r_7 = \frac{\alpha_m \cdot \epsilon_{pcc}}{\alpha_p + \alpha_m} \tag{2.35}$$

$$r_8 = \epsilon_m \tag{2.36}$$

where

$$\alpha_p = \frac{\mathrm{expVL}}{t_L \cdot (\mathrm{expVL} + 1)} \tag{2.37}$$

$$\alpha_m = \phi_L / t_L \tag{2.38}$$

$$\beta_{poc} = \frac{C_{oc}^2}{t_R \cdot (C_{oc}^2 + K_{\mathrm{RyR}}^2)} \tag{2.39}$$

$$\beta_{pcc} = \frac{[\mathrm{Ca}^{2+}]_{\mathrm{cyt}}}{t_R \cdot ([\mathrm{Ca}^{2+}]_{\mathrm{cyt}}^2 + K_{\mathrm{RyR}}^2)} \tag{2.40}$$

$$\beta_m = \frac{\phi_R}{t_R} \tag{2.41}$$

$$\epsilon_{pco} = \frac{C_{co} \cdot (\mathrm{expVL} + a)}{\tau_L \cdot K_L \cdot (\mathrm{expVL} + 1)} \tag{2.42}$$

$$\epsilon_{pcc} = \frac{[\mathrm{Ca}^{2+}]_{\mathrm{cyt}} \cdot (\mathrm{expVL} + a)}{\tau_L \cdot K_L \cdot (\mathrm{expVL} + 1)} \tag{2.43}$$

$$\epsilon_m = \frac{b \cdot (\mathrm{expVL} + a)}{\tau_L \cdot (b \cdot \mathrm{expVL} + a)} \tag{2.44}$$

$$\mathrm{expVL} = e^{\frac{V - V_L}{\Delta V_L}} \tag{2.45}$$

$$t_R = 1.17 \cdot t_L \tag{2.46}$$

$$\tag{2.47}$$

$$\mu_{poc} = \frac{(C_{oc}^2 + c \cdot K_{\mathrm{RyR}}^2)}{\tau_R \cdot (C_{oc}^2 + K_{\mathrm{RyR}^2)}} \tag{2.48}$$

$$\mu_{pcc} = \frac{[\mathrm{Ca}^{2+}]_{\mathrm{cyt}}^2 + c \cdot K_{\mathrm{RyR}}^2}{\tau_R \cdot ([\mathrm{Ca}^{2+}]_{\mathrm{cyt}}^2 + K_{\mathrm{RyR}}^2)} \tag{2.49}$$

$$\mu_{moc} = \frac{\theta_R \cdot d \cdot (C_{oc}^2 + c \cdot K_{\mathrm{RyR}}^2)}{\tau_R \cdot (d \cdot C_{oc}^2 + c \cdot K_{\mathrm{RyR}}^2)} \tag{2.50}$$

$$\mu_{mcc} = \frac{\theta_R \cdot d \cdot ([\mathrm{Ca}^{2+}]_{\mathrm{cyt}}^2 + c \cdot K_{\mathrm{RyR}}^2)}{\tau_R \cdot (d \cdot [\mathrm{Ca}^{2+}]_{\mathrm{cyt}}^2 + c \cdot K_{\mathrm{RyR}}^2)} \tag{2.51}$$

Parameter descriptions and values are listed in Table 2.4. The CaRU states are:

$$C_{co} = \frac{[\mathrm{Ca}^{2+}]_{\mathrm{cyt}} \cdot g_D + J_R \cdot [\mathrm{Ca}^{2+}]_{\mathrm{SR}}}{g_D + J_R} \tag{2.52}$$

$$C_{oc} = \begin{cases} \frac{g_D \cdot [\mathrm{Ca}^{2+}]_{\mathrm{cyt}} \left(1 - e^{-2\kappa}\right) + J_L \cdot [\mathrm{Ca}^{2+}]_o \cdot 2\kappa \cdot e^{-2\kappa}}{\left(g_D + \frac{J_L \cdot 2\kappa}{1 - e^{-2\kappa}}\right)(1 - e^{-2\kappa})} & |2\kappa| > 10^{-9} \\ \frac{g_D \cdot [\mathrm{Ca}^{2+}]_{\mathrm{cyt}} + J_L \cdot [\mathrm{Ca}^{2+}]_o}{g_D + J_L} & \text{otherwise} \end{cases} \tag{2.53}$$

$$y_{oc} = \frac{\alpha_p \cdot \beta_m \cdot (\alpha_p + \alpha_m + \beta_m + \beta_{pcc}}{y_{denom}} \tag{2.54}$$

$$y_{co} = \frac{\alpha_m \cdot (\beta_{pcc} \cdot (\alpha_m + \beta_m + \beta_{poc}) + \beta_{poc} \cdot \alpha_p)}{y_{denom}} \tag{2.55}$$

$$y_{oo} = \frac{\alpha_p \cdot (\beta_{poc} \cdot (\alpha_p + \beta_m + \beta_{pcc}) + \beta_{pcc} \cdot \alpha_m)}{y_{denom}} \tag{2.56}$$

$$y_{cc} = \frac{\alpha_m \cdot \beta_m \cdot (\alpha_m + \alpha_p + \beta_m + \beta_{poc})}{y_{denom}} \tag{2.57}$$

$$y_{denom} = (\alpha_p + \alpha_m) \cdot ((\alpha_m + \beta_m + \beta_{poc}) \cdot (\beta_m + \beta_{pcc}) + \alpha_p \cdot (\beta_m + \beta_{poc})) \tag{2.58}$$

Extracellular exchange and cell membrane fluxes

Fluxes through channels/leaks on the sarcollema are defined as follows:

$$J_{\mathrm{NCX}} = \frac{g_{\mathrm{NCX}} \cdot \left(e^{\eta\cdot\kappa} \cdot [Na^+]_i^3 \cdot [\mathrm{Ca}^{2+}]_e - e^{(\eta-1)\cdot\kappa} \cdot [Na^+]_e^3 \cdot [\mathrm{Ca}^{2+}]_{\mathrm{cyt}}\right)}{([Na^+]_e^3 + K_{mNa}^3) \cdot \left([\mathrm{Ca}^{2+}]_e + K_{\mathrm{mCa}}\right) \cdot (1 + k_{sat} \cdot e^{(\eta-1)\cdot\kappa})} \tag{2.59}$$

$$J_{\mathrm{PMCA}} = \frac{g_{\mathrm{PMCA}} \cdot [\mathrm{Ca}^{2+}]_i}{K_{\mathrm{PMCA}} + [\mathrm{Ca}^{2+}]_i} \tag{2.60}$$

$$J_{\mathrm{CaB}} = o_{\mathrm{CaB}} \cdot (E_{Ca} - U) \tag{2.61}$$

where

$$E_{Ca} = \frac{RT}{2F} \cdot \ln\left(\frac{[\mathrm{Ca}^{2+}]_o}{[\mathrm{Ca}^{2+}]_{\mathrm{cyt}}}\right) \tag{2.62}$$

$$V = \begin{cases} -0.4 \mod (t, T_{osc}) & \text{if } \mod (t, T_{osc}) \leq 200 \text{ ms} \\ V_0 & \text{otherwise} \end{cases} \tag{2.63}$$

where t is the time since the start of the simulation and T_{osc} is the period of the driving voltage. The shape of the driving voltage was altered from that described in the original Hinch et al. (55) model. Examination of the individual fluxes in simulations with reduced SERCA revealed that the original step function caused LTCCs to play a larger role than expected. As SERCA function was restricted, flux through LTCCs increased on a scale that resulted in peak amplitude increasing with reduced SERCA solely because of the influx of Ca^{2+} through LTCCs. We deemed this unlikely to be physiologically plausible and the voltage function reduced to its current form. The effects of this change in V on the $[Ca^{2+}]$ in the base model are negligible (but not shown).

Other fluxes across the SR membrane

$$J_{\mathrm{SERCA}} = \frac{g_{\mathrm{SERCA}} \cdot [\mathrm{Ca}^{2+}]_i^2}{K_{\mathrm{SERCA}}^2 + [\mathrm{Ca}^{2+}]_i^2} \tag{2.64}$$

$$J_{\mathrm{SRl}} = g_{\mathrm{SRl}} \cdot \left([\mathrm{Ca}^{2+}]_{\mathrm{SR}} - [\mathrm{Ca}^{2+}]_i\right) \tag{2.65}$$

Cytosolic buffers

The effects of cytosolic buffers troponin C, fluo-4AM, and calmodulin are described as follows.

$$J_{\mathrm{TnC}} = k_{\mathrm{TnC-}} \cdot (B_{\mathrm{TnC}} - \mathrm{TnC}) - k_{\mathrm{TnC+}} \cdot \mathrm{TnC} \cdot [\mathrm{Ca}^{2+}]_i \tag{2.66}$$

$$\beta_{\mathrm{fluo}} = \left(1 + \frac{K_{\mathrm{fluo}} \cdot B_{\mathrm{fluo}}}{\left(K_{\mathrm{fluo}} + [\mathrm{Ca}^{2+}]_i\right)^2}\right)^{-1} \tag{2.67}$$

$$\beta_{\mathrm{CaM}} = \left(1 + \frac{K_{\mathrm{CaM}} \cdot B_{\mathrm{CaM}}}{\left(K_{\mathrm{CaM}} + [\mathrm{Ca}^{2+}]_i\right)^2}\right)^{-1} \tag{2.68}$$

Parameters are described in Table 2.3

Parameter values used in modelled Ca^{2+} currents

Parameter	Description	Value
$\mathbf{N}$	Number of CaRUs in the cell	50 000
$\mathbf{V_{myo}}$	Myocyte volume	25.84×10^3 μm^3
$\mathbf{N_{IP_3R}}$	Number of IP_3R channels in the cell	20 000
$\mathbf{g_D}$	Ca^{2+} flux rate from dyadic space to cytosol	0.065 μm^{3}ms^{-1}
$\mathbf{g_{SERCA}}$	Maximum pump rate of SERCA	0.45 μM ms^{-1}
$\mathbf{K_{SERCA}}$	Half saturation constant of SERCA	0.5 μM
$\mathbf{g_{NCX}}$	Maximum pump rate of NCX	38.5 μM ms^{-1}
η	Voltage dependence of NCX	0.35
$\mathbf{K_{mNa}}$	Na^+ half saturation of NCX	87.5 mM
$\mathbf{K_{mCa}}$	Ca^{2+} half saturation of NCX	1.380 mM
$\mathbf{k_{sat}}$	Low potential saturation factor of NCX	0.1
$\mathbf{g_{PMCA}}$	Maximum pump rate of Ca^{2+}-ATPase	3.5 nM ms^{-1}
$\mathbf{K_{PMCA}}$	Half saturation constant of Ca^{2+}-ATPase	38.5 μM ms^{-1}
$\mathbf{o_{CaB}}$	Conductance of background Ca^{2+} current	2.32 $\times10^{-5}$ μM ms^{-1} mV^{-1}
$\mathbf{g_{SRl}}$	Pump rate of NCX	1.8951 $\times10^{-5}$ ms^{-1}
$\mathbf{K_t}$	IP_3R delayed response parameter	0.1 μM
$\mathbf{t_{max}}$	IP_3R recovery time parameter	1000 s^{-1}

Table 2.2: N_{IP_3R} from Harzheim et al. (50). All other values in this table are from Hinch (54)

Fixed ionic concentrations and buffer parameters

Ion	Description	Value
$[Na^+]_i$	Intracellular sodium	10 mM
$[Na^+]_e$	Extracellular sodium	140 mM
$[Ca^{2+}]_e$	Extracellular calcium	1 mM
B_{CaM}	Total cytosolic concentration of calmodulin	50 x 10^{-3} mM
K_{CaM}	Half saturation constant of calmodulin	2.38 x 10^{-3} mM
B_{TnC}	Total cytosolic concentration of troponin	70 x 10^{-3} mM
k_{TnC}^-	Dissociation rate of Ca^{2+} to troponin	0.04[3] mM^{-1} ms^{-1}
k_{TnC}^+	Binding rate of Ca^{2+} to troponin	0.04 μM^{-1} ms^{-1}
B_{fluo}	Concentration of Fluo-4AM dye	1 x 10^{-3} mM
K_{fluo}	Dissociation constant of Fluo-4AM dye	1 mM
V_0	Resting membrane potential	−80 mV

Table 2.3: K_{fluo} and B_{fluo} from (148). All other values in this table are from Hinch (54)

CaRU parameters

Parameter	Definition	Value
V_L	Potential when half LTCCs open	−2 mV
ΔV_L	Width of opening potentials	7 mV
ϕ_L	Ratio of time closed in active mode	2.35
t_L	Time spent switching between open and closed states	1 ms
τ_L	Inactivation time of LTCCs	650 ms
K_L	Ca^{2+} concentration at LTCCs inactivation	0.22 μM
a	Biasing to make inactivation function of V	0.0625
b	Biasing to make inactivation function of V	14
ϕ_R	Ratio of time open in active mode	0.05
t_R	Time spent switching between closed and open states	1.17 ms
τ_R	Inactivation time of RyRs	2.43 ms
K_{RyR}	Half concentration of RyR activation	41 μM
θ_R	Reciprocal of proportion of time inactivated in open mode	0.012
c	Biasing to make inactivation a functions of $[Ca^{2+}]_o$	0.01
d	Biasing to make inactivation a functions of $[Ca^{2+}]_o$	100
J_R	Permeability of single RyR	2×10^{-2} μm^3 ms^{-1}

Table 2.4: All parameter values in this table are from Hinch (54)

2.2.2 Output metrics

The main output metrics we examine in this chapter are maximum $[Ca^{2+}]_{cyt}$ (amplitude), full duration at half maximum (FDHM), baseline $[Ca^{2+}]$ (diastolic or basal $[Ca^{2+}]$), and duty cycle. These are shown in Figure 2.1A. As depicted in Figure 2.1A, the full duration at half maximum (FDHM) was measured as the duration for which $[Ca^{2+}]_{cyt}$ was higher than the midpoint between Max Ca^{2+} and c_0 per period. The duty cycle was calculated as the integral of $[Ca^{2+}]_{cyt}-$Basal $[Ca^{2+}]$ over time, divided by the product of the amplitude and the period of the measured transient.

2.3 Results

2.3.1 Parameter sensitivity analysis

We first conducted a parameter sensitivity analysis to determine the critical parameters related to IP_3R activation that affect the beat-to-beat cytosolic Ca^{2+} transient. While there are several experimental studies that have examined IP_3R gating properties (116, 38), and modelling studies exploring both the mechanisms (137) and gating dynamics (133) of IP_3R channels, there is still uncertainty as to the exact behaviour of IP_3R channels within cardiomyocytes during excitation contraction coupling. We can only use these studies, and our knowledge of adult rat ventricular myocyte (ARVM) structure and Ca^{2+} dynamics, as a guide to the likely behaviour of IP_3R channels within these cells. As such, a thorough parameter sensitivity analysis of the effect of the Sneyd et al. (137) IP_3R model on excitation contraction coupling simulations was required to narrow down the most important parameters in this model and their likely values in this context so that our model most accurately represents the effect of activating type II IP_3R channels in ARVMs.

We used the Jansen method (62) as detailed in Saltelli et al. (122) to calculate the 'main effect' and 'total effect' coefficients of each of the parameters associated with IP_3R channel gating in relation to changes in transient amplitude, duration, (FDHM), diastolic Ca^{2+} and duty cycle (see Table 2.5). Saltelli et al. (122) describe the main effect coefficient as 'the expected reduction in variance that would be obtained if [the parameter] could be fixed' and the total effect coefficient

as 'the expected variance that would be left if all factors but [the parameter] could be fixed', both normalised by the total variance.

Both coefficients are included here to provide a complete picture of the impact of each parameter.

Calculating the main and total effects

The Jansen method is a single parameter sensitivity analysis. Using this method, the main and total effects are calculated by generating two sampling matrices A and B of model parameter values and then, for each parameter, a matrix $A_B^{(i)}$ for which all but the ith column match those of A and the ith column is the ith column of B.

Given a model $Y = f(X_1, x_2, ..., X_k)$, with Y a scalar, such as FDHM of the Ca^{2+} transient, and X_i the model parameters, we denote $f(A)_j$ the results of the simulation with parameter in row j of the sampling matrix A; $V(Y)$ the variance in simulation results across all rows of A and B; and N the number of rows in A and B, i.e. the number of trials. The main effect, S_i, of parameter X_i is then:

$$S_i = V_{X_i}(E_{X_{\sim i}}(Y|X_i))\Big/V(Y) \tag{2.69}$$

$$= V(Y) - \sum_{j=1}^{N}\left(f(B)_j - f(A_B^{(i)})_j\right)^2\Big/2V(Y)N \tag{2.70}$$

Where $V_{X_i}(x)$ is the variance of x taken over X_i, and $E_{X_{\sim i}(Y|X_i)}$ is the expected value of Y taken over all possible values of $X_{\sim i}$ while keeping X_i fixed. $X_{\sim i}$ is the matrix of all parameters but X_i. Note this is a normalised index. The total effect, S_{T_i}, of parameter i is then:

$$S_{T_i} = E_{X_{\sim i}}(V_{X_i}(Y|X_{\sim i}))\Big/V(Y) \tag{2.71}$$

$$= \sum_{j=1}^{N}\left(f(A)_j - f(A_B^{(i)})_j\right)^2\Big/2V(Y)N \tag{2.72}$$

In our parameter analysis, we generated parameter values for the IP$_3$R gating parameters within the range [0, 100] using the MATLAB sobolset function with Skip 1×10^3 and Leap 1×10^2, scrambled with the Mattousek-Affine-Owen algorithm. N was set to 1×10^6.

Variance-based parameter sensitivity analysis

Main Effect Coefficients	$[IP_3]$	t_{max}	K_c	K_h	K_t	k_f
Amplitude	**0.27**	0.00	0.03	**0.19**	0.00	0.03
FDHM	**0.17**	0.00	0.01	**0.12**	0.00	**0.50**
Diastolic Ca^{2+}	**0.44**	0.00	0.09	0.03	0.00	0.04
Duty Cycle	**0.23**	0.00	0.01	**0.16**	0.00	**0.33**
Total Effect Coefficients	$[IP_3]$	t_{max}	K_c	K_h	K_t	k_f
Amplitude	**0.63**	0.04	**0.43**	**0.46**	0.02	**0.13**
FDHM	**0.33**	0.00	**0.19**	**0.19**	0.00	**0.54**
Diastolic Ca^{2+}	**0.79**	0.00	**0.45**	0.06	0.00	**0.18**
Duty Cycle	**0.45**	0.00	**0.25**	**0.24**	0.00	**0.38**

Table 2.5: Main and total effects of the IP_3R gating parameters on Ca^{2+} transient amplitude, duration (FDHM), diastolic $[Ca^{2+}]$, and duty cycle.

Table 2.5 shows that the delay parameters t_{max} and K_t do not have a large effect on the cytosolic Ca^{2+} transient. While they are necessary to describe the effect of IP_3R-dominated Ca^{2+} dynamics (137), they contribute only a small amount to the variance. Therefore we decided to fix these parameters in our simulations.

The coefficients show that cardiac cell Ca^{2+} dynamics during excitation contraction coupling are most highly sensitive to IP_3 concentration ($[IP_3]$) and the maximal flux through each IP_3R (k_f). The maximal flux k_f has little effect on transient amplitude, but a far greater influence on duration and duty cycle; while $[IP_3]$ has the greatest effect on the change in amplitude and diastolic Ca^{2+} concentration.

The gating parameters K_c and K_h also influence the cytosolic Ca^{2+} transient. K_h affects the $[Ca^{2+}]$ at which IP_3R channels are inhibited and K_c affects the $[Ca^{2+}]$ at which IP_3R channels open. We illustrate how these two parameters affect IP_3R open probability, P_{IP_3R}, in Figure 2.4. Figure 2.4 also shows how $[IP_3]$ affects the relationship between K_c, K_h, $[Ca^{2+}]$ and P_{IP_3R}. It can be seen that with $K_h = 80$ nM, P_{IP_3R} will be close to zero regardless of the values of Ca^{2+} or $[IP_3]$ or K_c. At $K_h = 1.6$ μM and $[IP_3] \geq 5$ μM P_{IP_3R} dependence on K_c and Ca^{2+} becomes apparent. Finally, at $K_h = 3.2$ μM, P_{IP_3R} is still dependent on K_c and Ca^{2+} values, but $[IP_3]$ does not change P_{IP_3R} significantly.

From this analysis we determine that in order for IP_3R channels to be active during excitation contraction coupling, K_h must be high enough that IP_3Rs are

not inhibited at diastolic $[Ca^{2+}]$. Conversely, K_c must be low enough that IP_3R channels are active at Ca^{2+} concentrations below the systolic Ca^{2+} peak. Therefore, in the remainder of this study, we fix K_h at 2.2 μM: high enough to fulfill this condition while low enough that IP_3R channels are still affected by $[IP_3]$. We report simulation results only within the range of K_c that exhibits experimentally plausible Ca^{2+} transient properties. Additionally, we fix t_max at 100 ms^{-1} and K_t at 0.01 mM.

With the plausible range of K_h and K_c established, we next show the effect of K_c, k_f and $[IP_3]$ on the excitation contraction coupling transient.

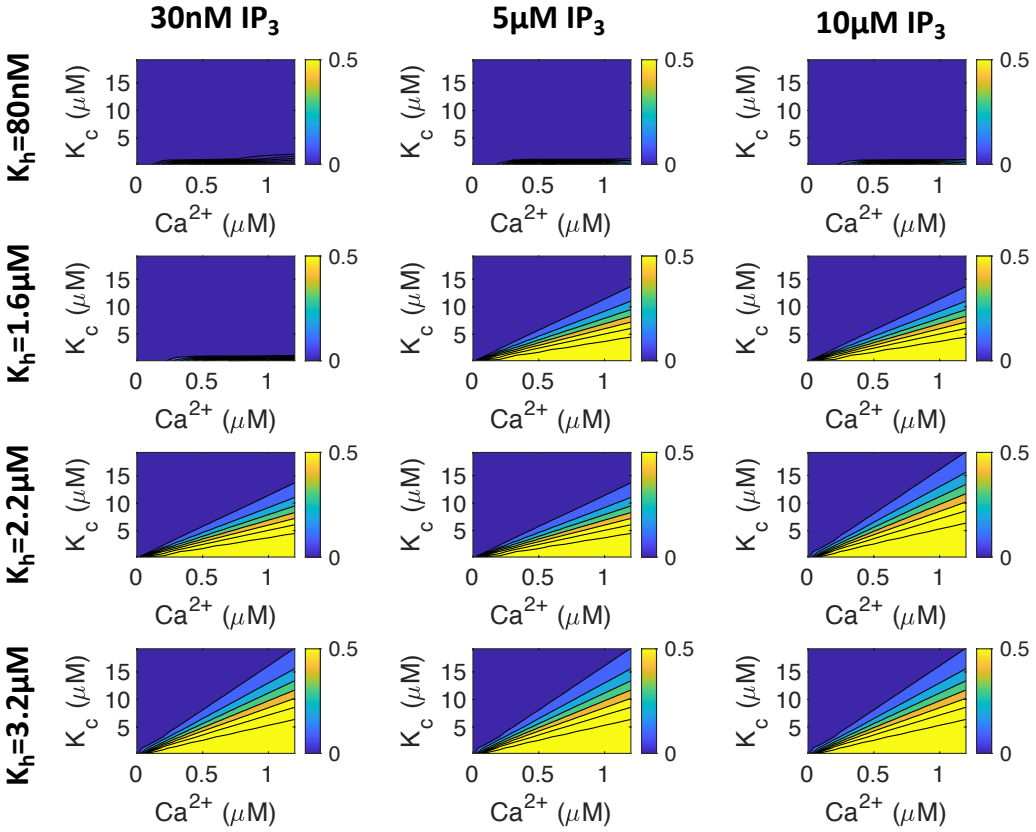

Figure 2.4: The effect of $[Ca^{2+}]$, $[IP_3]$, K_c, and K_h on P_{IP_3R} in the Siekmann-Cao-Sneyd IP_3R model (133, 18, 137). The coloured bars on the side of each plot show the proportion of IP_3R channels that will open for each set of parameters at steady state. Note that IP_3Rs do not open at physiological Ca^{2+} concentrations when K_h is low (i.e. 80 nM or less). In subsequent simulations we used the value $K_h = 2.2$ μM unless otherwise stated.

2.3.2 IP_3 concentration and IP_3R opening behaviour have the greatest impact on the Ca^{2+} transient

As summarised in Table 2.1, different experimental studies suggest different effects of IP_3R activation on the cytosolic excitation contraction coupling Ca^{2+} transient. For example, Signore et al. (136) demonstrated that mouse myocytes subjected to IP_3 stimulation exhibited increased Ca^{2+} amplitude. On the other hand, Escobar et al. (30) did not observe significant changes in the Ca^{2+} transient upon IP_3R activation. Using the model described above, we simulated the effect on cardiomyocyte calcium transients ($[Ca^{2+}]_{myo}$) when $[IP_3]$ is elevated. Figures 2.5A-C show quantitative predictions of how much Ca^{2+} transient properties could be affected by IP_3R activation across a range of $[IP_3]$ and Ca-dependent IP_3R gating parameter K_c values. k_f was fixed at 0.45 $\mu m^3 ms^{-1}$ and K_h was fixed at 2.2 μM. Refer to Figure 2.1A for illustrations of the qualities assessed. For reference, without active IP_3Rs, the amplitude of the transient would be 0.63 μM, the FDHM would be 69 ms, the basal $[Ca^{2+}]$ would be 0.1 μM, and the duty cycle would be 0.127.

The yellow region in Figure 2.5A corresponds to IP_3R activation parameters that produce the greatest increase in Ca^{2+} amplitude. This region corresponds to K_c values greater than 4 μM and $[IP_3]$ greater than 2 μM. With K_h set at 2.2 μM, this corresponds to the middle and far-right plots of P_{IP_3R} in Figure 2.4. The middle subfigure shows that with K_c greater than 4 μM IP_3R channels would open only at Ca^{2+} concentrations greater than the diastolic concentration of $\sim$0.1 μM. The plot also shows that IP_3Rs would remain active at Ca^{2+} concentrations greater than the usual peak concentration of $\sim$1 μM.

Figure 2.5B shows that the duration (FDHM) of the Ca^{2+} transient increases when IP_3Rs are active. This increase is greater with greater concentrations of IP_3 and with lower values of K_c. Figure 2.5C indicates that K_c and $[IP_3]$ have a similar effect on the diastolic Ca^{2+} concentration. However, in Figure 2.5C it can be seen that the diastolic Ca^{2+} concentration decreases in approximately the parameter range where the amplitude is maximised (Figure 2.5A). In all three figures (A-C) there is little change when $[IP_3]$ is low and K_c is high (bottom right corner of each image). This is a regime in which the IP_3R channels barely open in response to ECC transients. For comparison, Figure 2.6 shows the same simulations as Figure 2.5 at a commonly used experimental pacing frequency of 0.3 Hz, showing similar trends.

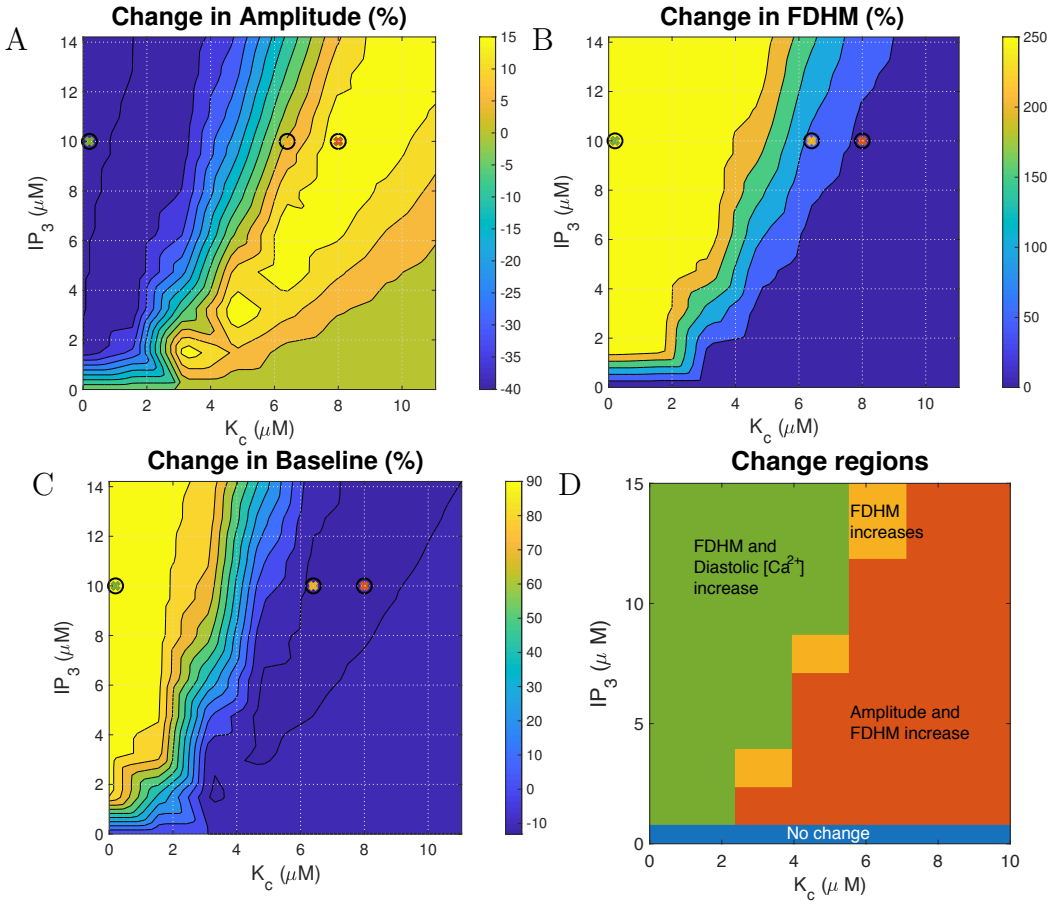

Figure 2.5: Effect of IP_3 concentration and the parameter K_c on the Ca^{2+} transient with pacing frequency 1 Hz. These two parameters, along with maximum IP_3R flux, k_f have the greatest impact when considering the effect of IP_3R activation on the Ca^{2+} transient. (D) Shows the different parameter regimes present in the model where blue indicates little to no change on in the Ca^{2+} transient on activation of]iprs, green indicates an increase in duration and diastolic $[Ca^{2+}]$, yellow indicates an increase in duration only, and orange indicates an increase in both duration and transient amplitude. See Figure 2.7 for simulated transients at parameters indicated by crosses.

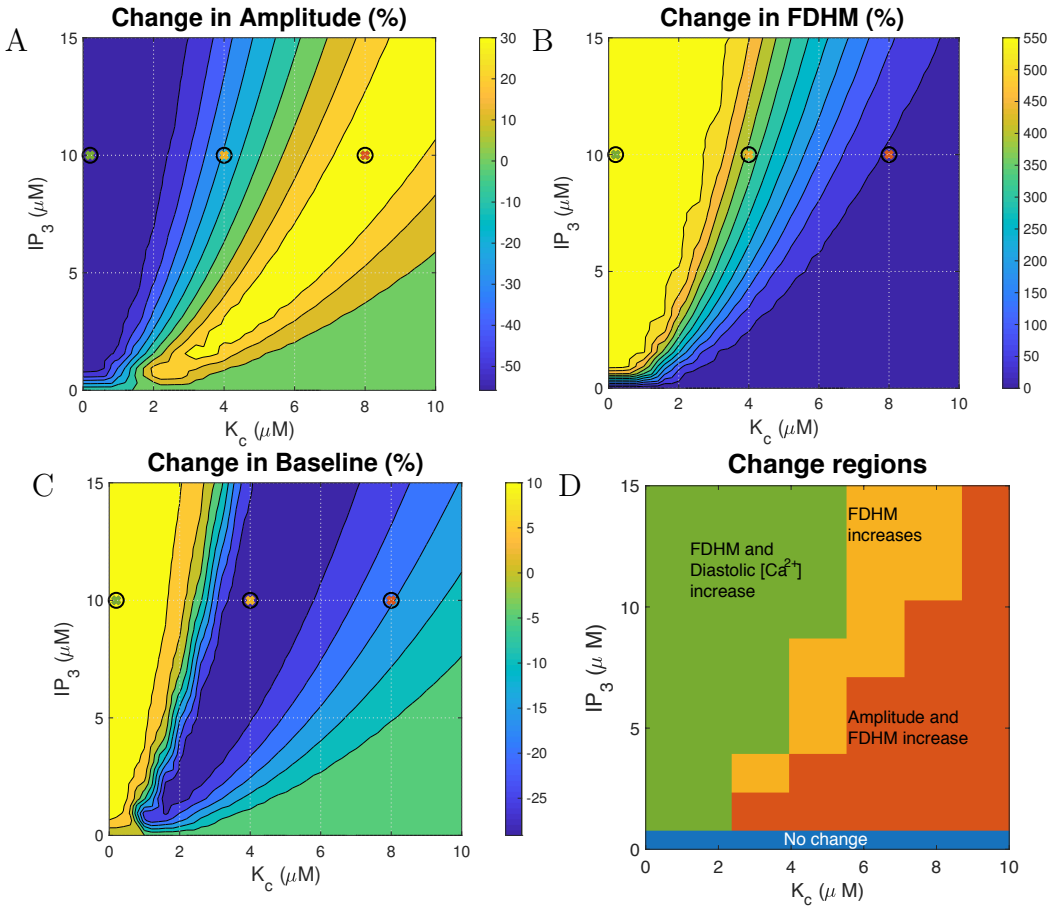

Figure 2.6: Effect of IP_3 concentration and the parameter K_c on the Ca^{2+} transient with large delay and pacing frequency of 0.3 Hz. These two parameters, along with maximum IP_3R flux, have the greatest impact when considering the effect of IP_3R activation on the Ca^{2+} transient. (D) Shows the different parameter regimes present in the model where blue indicates little to no change on in the Ca^{2+} transient on activation of]iprs, green indicates an increase in duration and diastolic $[Ca^{2+}]$, yellow indicates an increase in duration only, and orange indicates an increase in both duration and transient amplitude.

In order to compare our simulation results with the experimental observations summarised in Table 2.1 we divided the parameter space shown in Figures 2.5A-C into four regions, shown in Figure 2.5D. In the orange region amplitude and duration increase. In the yellow region only duration increases. In the green region duration and diastolic $[Ca^{2+}]$ increase but amplitude decreases. Comparing to the experimental observation of amplitude increase summarised in Table 2.1, the red region appears to describe the most plausible parameter range. Figure 2.5D also shows that there is no parameter set where both amplitude and diastolic Ca^{2+} concentration increase. Furthermore, there is no region in which transients with

increased amplitude and decreased duration are observed, as has been reported in endothelin 1 (ET-1) treated rat ventricular myocytes experiments (100) (Refer to subsection 1.2.1 for significance of ET-1). Finally, with the exception of the blue region in which there is no change, we observe that the duration increases in all parameter regimes.

To examine these results further, we investigated model behaviour in different regions of Figure 2.5D, shown in Figure 2.7. Examining the green and blue cytosolic Ca^{2+} profiles in Figure 2.7, we find that IP_3R opening at diastolic Ca^{2+} levels and IP_3R inhibition at Ca^{2+} levels below peak transient concentrations generates a flatter Ca^{2+} transient after IP_3R activation. This is the result of a gradual depletion of SR Ca^{2+} stores from IP_3Rs opening. This subsequently leads to lower Ca^{2+} release through RyR and IP_3R channels. Interestingly, a delayed time to peak is observed with IP_3R activation in all regimes selected.

The increase in duration of the transient from IP_3R activation apparent in Figure 2.5B can be explained by continued release of Ca^{2+} through IP_3R channels after RyRs have closed in Figure 2.7. The slower release through IP_3R channels after RyRs close is a result of a smaller proportion of the channels opening and a decrease in SR Ca^{2+} store load.

2.3.3 Maximum flux through IP_3Rs can increase signal duration

The parameter sensitivity analysis in Table 2.5 indicates that maximum flux through IP_3Rs (k_f) has the greatest effect on Ca^{2+} transient duration. Therefore we next examined how increased k_f values in our model affect the Ca^{2+} transient. Figure 2.8A-C show that for $K_c < 2$ μM, increasing k_f above 0.45 $\mu m^3 m s^{-1}$ mostly increases transient duration but has only marginal effects on amplitude and baseline. However for large K_c, the role of k_f in modifying transient shape becomes more noticeable. There is a clear region where amplitude increases (red region), however this is more dependent on K_c than k_f. At 1 Hz, there is no value of k_f that reduces transient duration. With IP_3R activation the transient duration increases and k_f merely determines by how much. However it is of note that, as shown in Figure 2.9, at a lower frequency of 0.3 Hz, when $k_f > 1.2$ $\mu m^3 m s^{-1}$ and $K_c > 8$ μM, there is a decrease in duration of the transient.

To compare simulation results to experimental observations in Table 2.1, we divided the parameter space shown in Figures 2.8A-C into three regions, shown

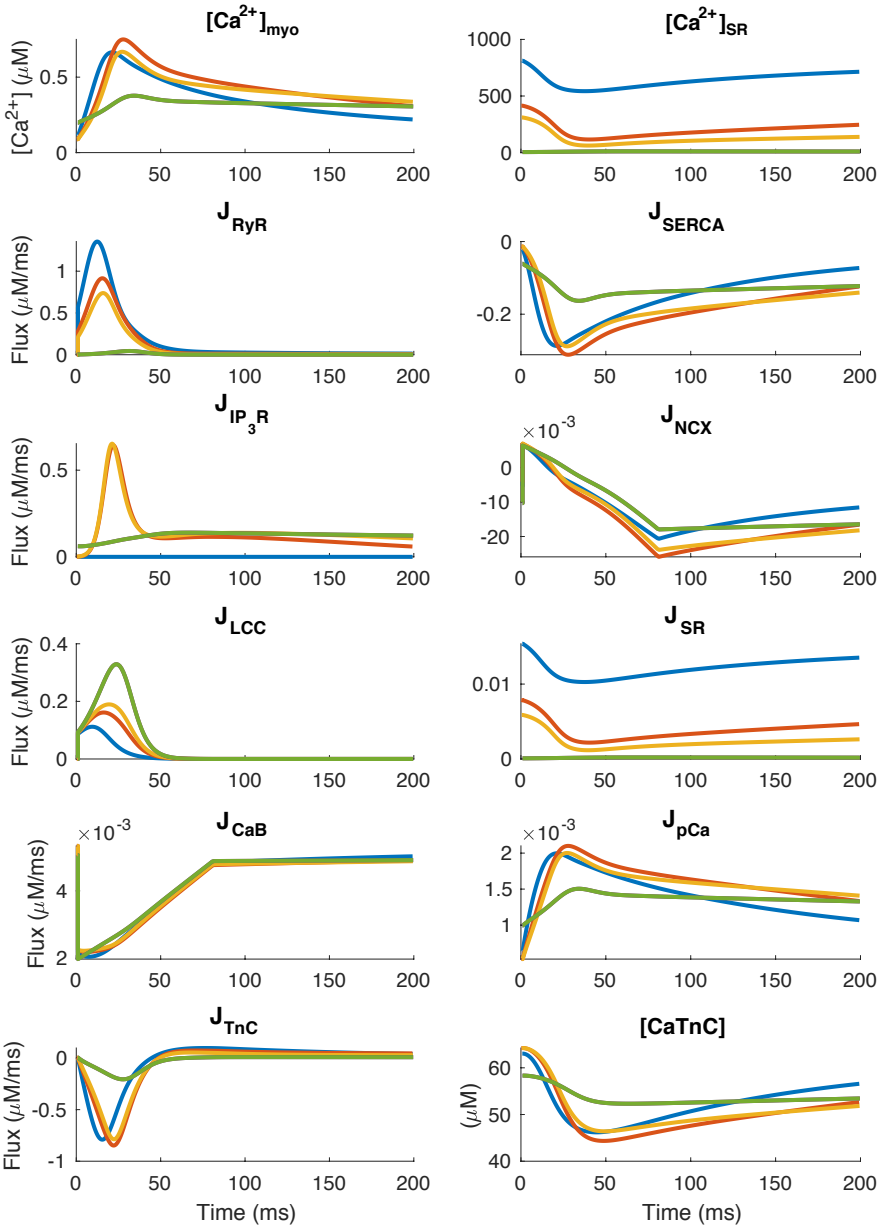

Figure 2.7: Simulated ECC transient and fluxes in the absence (blue) and presence of IP_3, corresponding to low (green), medium (orange) and high (red) values of K_c. With $K_c = 8$ μM (orange), IP_3R channels open only at Ca^{2+} concentrations greater than 0.1 μM. This results in increased peak in cytosolic Ca^{2+} transients and depleted sarcoplasmic reticulum Ca^{2+} stores. Parameters here were selected to show: absence of IP_3R channels (blue), increased transient amplitude (orange, red) and IP_3Rs parameterised as described in the original Siekmann-Cao-Sneyd model (green). IP_3 concentration is 10 μM and pacing frequency 1 Hz in all simulations. The sign of J_{NCX} indicates whether Ca^{2+} is moving into (positive) or out of (negative) the cell.

in Figure 2.8D. The regions in this figure are consistent with the regions labelled in Figure 2.5D. Figure 2.9D shows similar regions corresponding to 0.3 Hz results. It can be seen that at 0.3 Hz, $K_c > 8$ μM and $k_f > 1.2$ μ $\mathrm{m^3 m} s^{-1}$ provide transients with increased amplitude and decreased duration, consistent with Rat ET-1 experiments summarized in Table 2.1. However this value of k_f results in an unrealistic flux through IP_3R channels. Additionally, *in vivo*, the cell would be paced at a faster frequency and this result is unlikely without the cell being able to return to resting $[Ca^{2+}]$. We have not been able to identify a parameter set that would provide a simultaneous increase in both amplitude and basal Ca^{2+} .

2.3.4 RyR and IP_3R interaction increases the intracellular Ca^{2+} duty cycle

Having established reasonable parameters ranges for IP_3R activation based on the influence on ECC Ca^{2+} transient properties (amplitude, duration, and diastolic Ca^{2+}), we investigated the possibility that cytosolic $[Ca^{2+}]$ plays a role in hypertrophic remodelling through changing the duty cycle. Given the time scale involved in hypertrophic remodelling, and the signal integration properties of NFAT, the IP_3R -modified cytosolic Ca^{2+} transient could cumulatively encode hypertrophic signalling. Using optogenetic encoding of cytosolic Ca^{2+} transients in HeLa cells, Hannanta-anan and Chow (49) demonstrated that the transcriptional activity of NFAT4 can be upregulated by increasing cytosolic $[Ca^{2+}]$ duty cycle. This is a plausible mechanism of signal encoding that is likely to be less susceptible to noise than either amplitude or frequency encoding. Therefore, we examined the cytosolic $[Ca^{2+}]$ duty cycle as a hypertrophic signalling mechanism. Figure 2.11 shows the effects of $[IP_3]$, k_f, and K_c on the duty cycle of the cytosolic Ca^{2+} transient. Figure 2.11 shows that the calcium duty cycle increases with IP_3R activation across the broad parameter range shown.

2.4 Discussion

We have presented here what is, to our knowledge, the first modelling study to investigate the effect of IP_3R channel activity on the cardiac ECC Ca^{2+} transient and possible information encoding mechanisms. The model was able to replicate

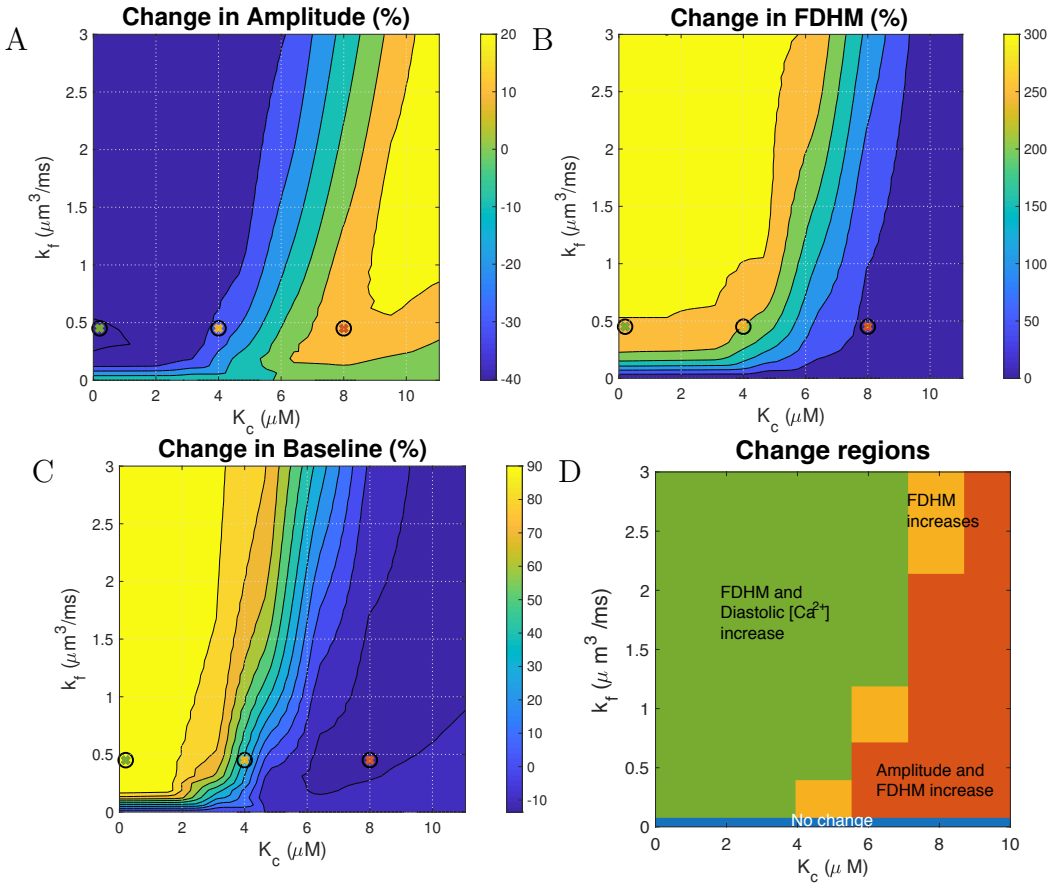

Figure 2.8: Effect of maximum IP_3R flux k_f and the $[Ca^{2+}]$ -sensitivity parameter K_c on the Ca^{2+} transient at 1 Hz. Maximum IP_3R flux has the greatest impact on transient duration. In these simulations $[IP_3] = 10$ μM. (D) Shows the different parameter regimes present in the model where blue indicates little to no change on in the Ca^{2+} transient on activation of]iprs, green indicates an increase in duration and diastolic $[Ca^{2+}]$, yellow indicates an increase in duration only, and orange indicates an increase in both duration and transient amplitude. See Figure 2.7 for simulated transients at parameters indicated by crosses.

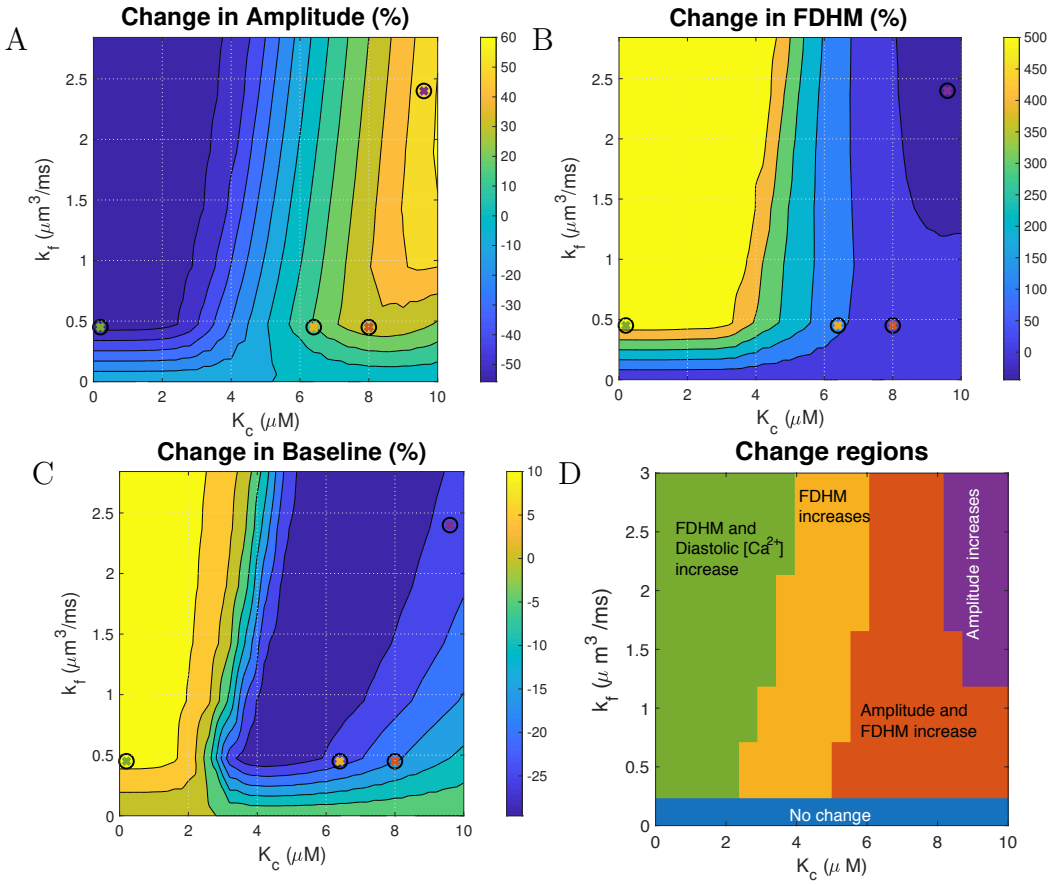

Figure 2.9: Effect of maximum IP$_3$R flux k_f and the [Ca^{2+}] sensitivity parameter K_c on the Ca^{2+} transient at 0.3 Hz. Maximum IP$_3$R flux has the greatest impact on transient duration. In these simulations [IP$_3$] = 10 μM. (D) Shows the different parameter regimes present in the model where blue indicates little to no change on in the Ca^{2+} transient on activation of]iprs, green indicates an increase in duration and diastolic [Ca^{2+}] , yellow indicates an increase in duration only, purple indicates an increase in transient amplitude only, and orange indicates an increase in both duration and transient amplitude. See Figure 2.10 for simulated transients at parameter values indicated by crosses.

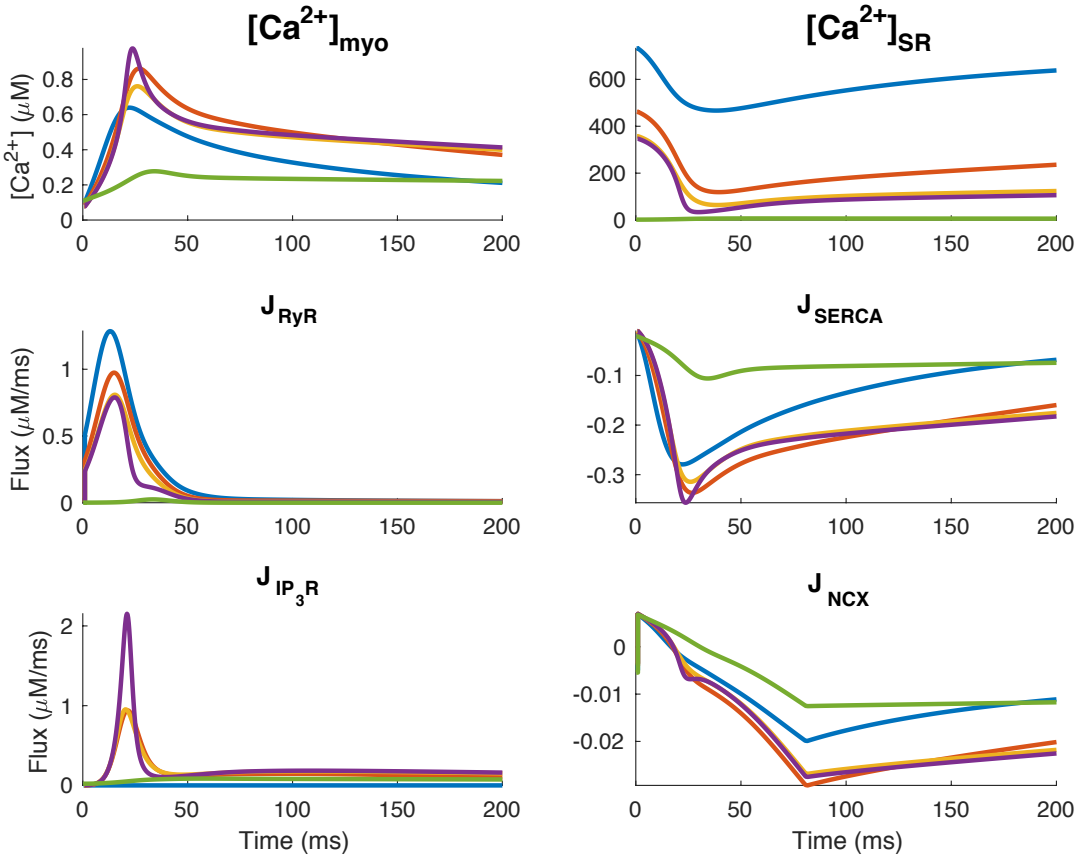

Figure 2.10: Simulated hypertrophic ECC transient and fluxes with varying k_f and K_c. The sign of I_{NCX} indicates whether Ca^{2+} is moving into (positive) or out of (negative) the cell. Parameters here are chosen to show the system behaviour at each region illustrated in Figure 2.9. The crosses in each of Figure 2.6 and Figure 2.9 match the colours of the corresponding transients in this figure. IP_3 concentration is 10μM in all simulations. The model was paced at 0.3Hz.

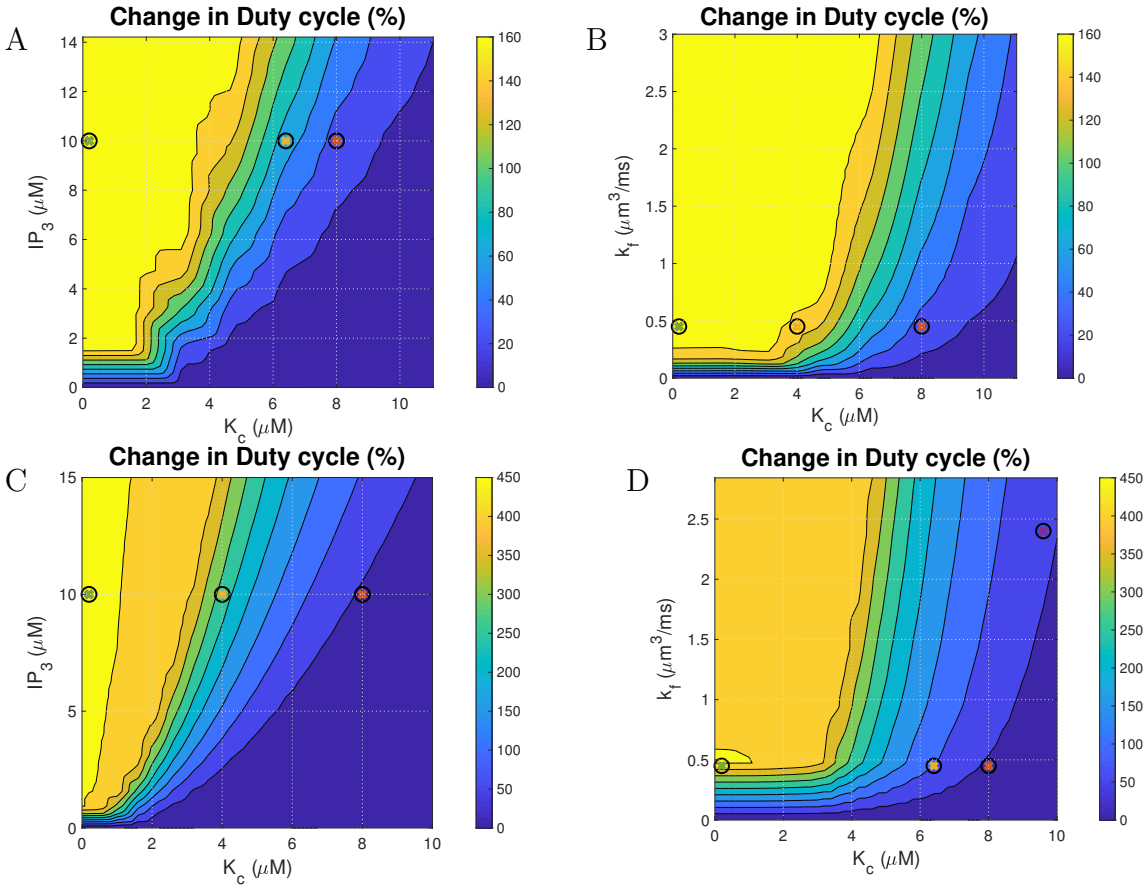

Figure 2.11: Effects on the Ca^{2+} transient duty cycle of (A) IP_3 concentration and the $[Ca^{2+}]$ sensitivity parameter K_c with pacing frequency 1 Hz; (B) of maximum IP_3R flux k_f and K_c with pacing frequency 1 Hz; (C) of IP_3 concentration and K_c with pacing frequency 0.3 Hz; and (D) of maximum IP_3R flux k_f and the K_c at pacing frequency 0.3 Hz. The colour bar indicates the % change from a simulation run with identical parameters but no IP_3R channels. The coloured crosses indicate the parameters used for the corresponding plots in Figure 2.7. Hannanta-anan and Chow (49) report a transcription rate increase of approximately 30% with a duty cycle increase of 50% in Figure 2 of their paper. The duty cycle of the Ca^{2+} transient when IP_3Rs are inactive is 0.127.

several experimentally observed effects of varying IP_3R activation and IP_3 concentration on the ECC Ca^{2+} transient. We find that under fixed maximum IP_3R flux, $k_f = 0.45\ \mu m^3 m s^{-1}$, IP_3R activation increases the duration of the Ca^{2+} transient, but that the effect on peak Ca^{2+} is IP_3-dependent. The Ca^{2+} transient duration is only reduced by increasing k_f into physiologically unrealistic values.

We showed that while amplitude, duration, and diastolic Ca^{2+} can increase or decrease depending on IP_3R parameter values and pacing frequency, the duty cycle, as defined by Hannanta-anan and Chow (49) always increases with increasing IP_3. The implication of this observation is that IP_3R activation is sufficient to provide a signal to drive NFAT translocation and hence hypertrophic gene expression in the manner described by Hannanta-anan and Chow (49).

2.4.1 The biological significance of the duty cycle

Hannanta-anan and Chow (49) found that, when comparing $[Ca^{2+}]$ oscillations of the same amplitude, oscillations with greater duty cycle had a greater effect on NFAT dephosphorylation and translocation to the nucleus. In their study, duty cycle, γ, was calculated as the integral of $[Ca^{2+}]_{myo}$−Basal $[Ca^{2+}]$ over time, divided by the maximum area under the curve (for $[Ca^{2+}]$ oscillations of the same amplitude, A, and period of oscillation, T), i.e. $\gamma = U/AT$ (see Figure 2.1A). As in Hannanta-anan and Chow (49), area under the curve is calculated as the integral of the $[Ca^{2+}]$ over time. An alternative definition is $\gamma = \Delta/T$, where Δ is the transient duration and T the period of oscillation. This alternate formulation is used by Tomida et al. (149) and Salazar et al. (121) but is less well defined for analogue signals. The duty cycle in Figure 2.11 was calculated using the former definition. This can be compared with the latter definition when remembering that duty cycle will now vary with duration (Figures 2.5C and 2.8C).

The duty cycle in this system essentially reflects the fraction of each period of the $[Ca^{2+}]$ cycle for which cytosolic $[Ca^{2+}]$ is sufficiently elevated to affect the downstream proteins in the CnA/NFAT signalling pathway. While it is difficult to determine where this threshold is, NFAT is a Ca^{2+} integrator and a clear correlation has been found between $[Ca^{2+}]$ duty cycle and NFAT activation (49). Increasing duty cycle increases the time NFAT spends in the dephosphorylated state, which is required to both enter the nucleus and effect transcription; NFAT responds to changes in duty cycle while being insensitive to both amplitude and frequency changes. In experiments, IP_3 stimulation has been shown to lead to an

increase in systolic $[Ca^{2+}]$ in cardiac cells, however significant change in duration has not been reported. Based on the duty cycle equation, the overall effect on NFAT activation in this situation is negative. Therefore we postulate that NFAT is responsive to the Ca^{2+} transient through the latter definition – the duration of time that $[Ca^{2+}]$ is elevated over a threshold divided by the period. This is more consistent with both the biological mechanism and the potential increase in peak Ca^{2+} concentration in the hypertrophic pathway. Further research, both theoretical and experimental, is required in order to determine the validity of this assumption.

2.4.2 Experimental evidence of an increase in duty cycle?

An increase in duty cycle without an increase in frequency requires an increase in transient duration. While this increase is observed in our simulations for a broad range of parameter values, it has not however been reported in experiments involving IP_3 stimulation. The possible reasons for this are many and varied, however, as discussed earlier, using different IP_3 concentrations to those that occur *in vivo* may result in different effects on the shape of the $[Ca^{2+}]$ oscillations, leading to inconsistent observations. Furthermore, small variations in Ca^{2+} concentrations may not be experimentally discernible, or may be hidden by the effect of Ca^{2+}-sensitive dyes (139). A small, but prolonged variation in transient duration can produce a comparatively large change in duty cycle. Hence it remains to be confirmed experimentally whether IP_3R-dependent Ca^{2+} flux does indeed lead to an increased Ca^{2+} duty cycle in cardiomyocytes.

2.4.3 Experimental evidence of the effect of increased IP_3R density can tell us more about IP_3R gating behaviour

In atrial (78, 57) and hypertrophic cells (50), stimulation of myocytes with IP_3 has a greater effect on the Ca^{2+} transient than stimulation of healthy ventricular myocytes, producing a far greater increase in transient amplitude. Harzheim et al. (50) found that the hypertrophic ventricular rat myocytes used in these experiments had approximately 3-fold more IP_3R channels than the healthy rat myocytes. Similarly, atrial myocytes are also known to have higher IP_3R density than ventricular myocytes (78). If we make the admittedly large assumption that the difference in IP_3R channel density is the main factor behind this change, this

puts a restriction on the possible values of IP_3R channel flux, k_f, and the IP_3R opening parameter, K_c. The values of these parameters are then restricted to those in which an increase in N_{IP_3R} will increase transient amplitude. We can estimate the range of parameters that fit this restriction using Figure 2.8 to find the values of K_c and corresponding range of k_f for which amplitude increases with k_f .

2.4.4 Limitations of the study

In this work we have considered only voltage driven Ca^{2+} transients with deterministic gating models of each channel. As such there are no stochastic events such as sparks or puffs in this model. Instead of sparks, our deterministic model can only show a small, deterministic Ca^{2+} current. This means that we do not see any of the stochastic features of Ca^{2+} transients that are described in experiments such as Harzheim et al. (50) and Proven et al. (113). However, the overall behaviour is nevertheless representative of the average transient in a cardiomyocyte.

While cell structure is known to play a role in cardiac Ca^{2+} dynamics (41, 115, 75), effects beyond the synchronising function of the dyad are beyond the scope of this study. As a compartmental model, we have ignored the spatial effects of IP_3R distribution in its formulation. In the absence of conclusive data, we base this model primarily on parameters fitted by Hinch et al. (55) and Sneyd et al. (137) and make no distinction between IP_3R channels located within or outside the dyad (96, 97). These and other structural features of the cell could alter the $[Ca^{2+}]$ available to regulate IP_3R channels and may be visible in the Ca^{2+} transient.

Distinct effects of IP_3 signalling in the nucleus and cytosol are not considered in this model. Cytosolic Ca^{2+} is thought to promote translocation of NFAT into the nucleus, while nuclear Ca^{2+} maintains it there. Hence we have only investigated one component of Ca^{2+} signalling within the CnA/NFAT pathway. Additionally, not all components of this pathway have been included in this study. Indeed Ca^{2+}/calmodulin-dependent kinases II and Class IIa histone deacetylases are both known Ca^{2+}-mediated components of the hypertrophic pathway not included in this model. Here we focus only on the impact of IP_3R activation on the cytosolic Ca^{2+} dynamics and how this relates to possible mechanisms of NFAT activation. In order to further explore through modelling the effects of

IP_3 mediated hypertrophic signalling it remains to couple this to IP_3 production (23, 24), to downstream activation of NFAT (25), and to the wider hypertrophic signalling network (120).

2.4.5 Conclusion

The sensitivity of NFAT translocation to the $[Ca^{2+}]$ duty cycle demonstrated by Hannanta-anan and Chow (49) raises the question as to whether IP_3R flux can increase the $[Ca^{2+}]$ duty cycle in cardiomyocytes. Here we have shown using mathematical modelling that an increase in cytosolic Ca^{2+} transient duration may occur following addition of IP_3. Together, these results suggest a plausible mechanism for hypertrophic signalling via IP_3R activation in cardiomyocytes. While it cannot be ruled out that a significant role is played by components of this pathway that are not considered here, the computational evidence provided in this study along with the previous experimental findings suggests encoding of the hypertrophic signal through variation of the duration of cytosolic $[Ca^{2+}]$ oscillations to be a feasible mechanism for IP_3-dependent hypertrophic signalling.

Chapter 3

Calcium transport in the nucleus

In this chapter we consider Ca^{2+} dynamics in the cell nucleus. Some of the most important processes within the cell occur in or originate from the nucleus. The nucleus is where DNA transcription occurs, and hence is integral in controlling the production of proteins, regulating the fundamental workings of the cell. There is a gap in our understanding of how Ca^{2+} regulates the hypertrophic pathway within the nucleus. We know that there must be a Ca^{2+} signal present in the nucleus for gene regulation to take place but we know very little about Ca^{2+} in the nuclear environment. Exactly how the environment of the nucleus shapes Ca^{2+} dynamics and how Ca^{2+} entry and exit is regulated is still unclear. Beginning with the fundamentals – Ca^{2+} diffusion into a cylindrical approximation of the nucleus during a single period of the cytosolic excitation contraction coupling signal– we build up a model of nuclear Ca^{2+} dynamics with what is known from experimental measurements.

3.1 Introduction

3.1.1 The role of calcium in the nucleus

As in the cytosol, Ca^{2+} plays an important role in the nucleus as a secondary messenger. Ca^{2+} dynamics within this compartment are of particular interest because of the long term, cell-wide effects that can result from gene regulation. Nuclear Ca^{2+} is known to signal cell division, differentiation, growth, and apoptosis (44, 106, 92, 114). We are especially interested in the process known as excitation-transcription coupling (ETC) – in which Ca^{2+} signals initiated by an

external factor influence gene regulation. Once again, the problem that we focus on is that of understanding the cardiac hypertrophic pathway. The cardiac hypertrophic pathway is known to be activated by stress on the heart. It is initiated through external factors sensed at the cell membrane such as increased concentrations of endothelin-1 (ET-1), angiotensin II (Ang-II), or catecholamine signals (51). The cytosolic component of this pathway, in which Ca^{2+} signals lead to dephosphorylation of NFAT by calmodulin (CaM) and calcineurin A (CnA), was explored in the previous chapter. In this chapter, we examine the downstream Ca^{2+} signalling that occurs in the nucleus. While IP_3R channels are distributed throughout the cell, there is some (mixed) evidence that they are concentrated around the nuclear compartment, indicating a potentially stronger influence on Ca^{2+} dynamics in the nuclear vicinity (50, 40). IP_3-generated hypertrophic Ca^{2+} signals in or around the nucleus activate calmodulin kinase II (CaMKII), a protein linked to gene regulation in cardiac hypertrophy (172, 28), which phosphorylates histone deacetylase 5 (HDAC5), exporting it from the nucleus (91). Specific nuclear Ca^{2+} signals are also required to ensure that CnA remains bound to NFAT. This allows NFAT to remain dephosphorylated so that it remains in the nucleus to enact gene regulation. Removal of HDAC5, which represses the hypertrophic genes, together with the presence of dephosphorylated NFAT, initiates hypertrophic gene transcription and, hence, cell remodelling (107).

Garcia and Boehning (40) found that the CnA/NFAT hypertrophic pathway was not dependent on nuclear-specific Ca^{2+} transients. This means that we must look for Ca^{2+} signalling mechanisms built around altering the heart's regular contraction-inducing Ca^{2+} dynamics that might transmit the hypertrophic signal within the nucleus. While hypertrophic Ca^{2+} signals are known to lead to hypertrophic gene transcription, regular, contraction-initiating Ca^{2+} signals which have been observed to propagate into the nucleus from the cytosol are not known to affect gene transcription (165, 8). The factors controlling Ca^{2+} dynamics in the nucleus and the elements of nuclear Ca^{2+} that are necessary in the CnA/NFAT pathway are yet to be fully determined. To this end, this, and the following chapter explore the underpinning biophysical processes controlling nuclear Ca^{2+} in cardiomyocytes and the potential effects of IP_3-induced Ca^{2+} release in the nucleus.

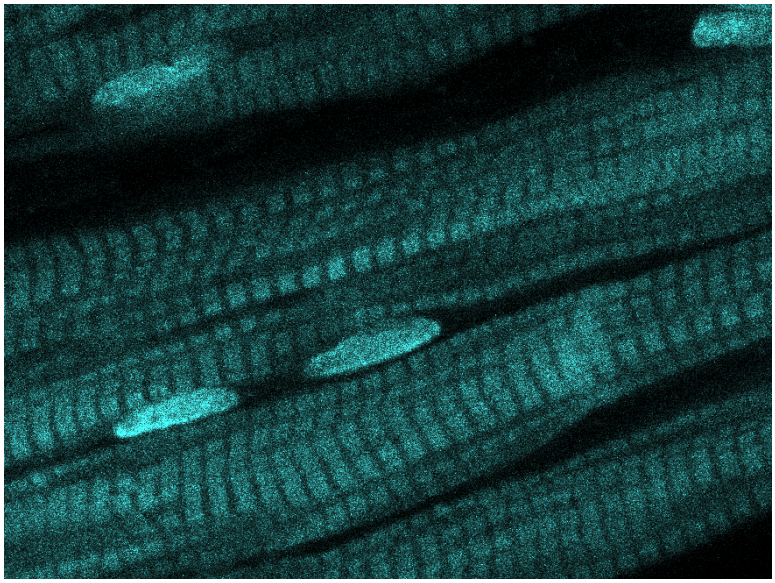

Figure 3.1: Fluorescent microscopy image of cardiac cells with visible nuclei. Unpublished image recorded by Gregory Bass (4)

3.1.2 The structure of the nucleus

Cardiac nuclei, pictured in Figure 3.1, are ellipsoidal organelles separated from the cytosol by a double membrane called the nuclear envelope (NE). This membrane is contiguous with the sarcoplasmic reticulum (SR), the cell's primary Ca^{2+} store (163). Like the SR, the outer membrane of the NE is studded with a number of Ca^{2+} channels, such as ryanodine receptor channels (RyRs) and inositol 1,4,5-trisphosphate receptor channels (IP_3Rs); and Ca^{2+} pumps, such as the sarco/endo-plasmic reticulum ATPase (SERCA) (163). A number of proteins containing nuclear localisation signals, such as nucleoplasmin, are actively transported across the NE, between the nucleus and the cytosol (89, 125). For smaller molecules, the two layers of the NE are spanned by large protein complexes known as nuclear pore complexes (NPC). NPCs allow the diffusion of molecules smaller than approximately 20kDa between the nucleus and cytosol (70). This includes charged molecules like Ca^{2+}. The NE is also known to extend inwards in temporary, nuclear invaginations. These invaginations may be extensions of just the inner membrane or both membranes and can affect the Ca^{2+} signal seen in the nucleus (47, 12, 90).

The inside of the nucleus is spanned by a mesh-like network of proteins known as the matrix. The matrix provides the structure for a host of transcriptional machinery necessary for the cell including chromatin; the nucleoli, where ribosomes

are produced; and ribonucleoproteins. The periphery of the matrix, which is in contact with the inner membrane of the NE, is known as the nuclear lamina and is primarily composed of proteins known as lamins (44). The extent of any interactions between Ca^{2+} and the matrix is unclear. However, both chromatin (26) and many gene regulatory proteins (44) are known to have Ca^{2+} binding sites.

3.1.3 Calcium entry into the nucleus

Confocal experiments clearly show that $[Ca^{2+}]$ in the nucleus can be directly correlated with $[Ca^{2+}]$ in the cytosol during regular heart cell function (95, 42, 105). Ca^{2+} is thought to diffuse directly via the NPCs. Genka et al. (42) show that there is a fast phase followed by a slow phase of Ca^{2+} diffusion into the nucleus, potentially controlled by the width of NPC pores. The main differences between the two being a delay and reduction in the peak $[Ca^{2+}]$ in the nucleus. NPC permeability is thought to be affected by available concentrations of both ATP and Ca^{2+} (42). Concentration of Ca^{2+} in the NE stores in particular is known to affect NPC permeability (111, 156, 123). Ca^{2+} diffusion within the nucleus is believed to be slower than in the cytosol (39). In the cytosol of cardiomyocytes, it is estimated to be somewhere between 0.007 $\mu m^2/ms$ and 0.22 $\mu m^2/ms$ (74, 144, 82) but, due to buffering, is dependent on the Ca^{2+} concentration.

There appears to be a constant Ca^{2+} leak through IP_3R II channels from the NE into the nucleus, increasing the resting nuclear Ca^{2+} concentration to approximately 0.11 μM, slightly higher than the resting cytosolic Ca^{2+} concentration of 0.1 μM (80). When the cell is paced, the disparity in nuclear and cytosolic $[Ca^{2+}]$ during diastole increases further (80). It is generally believed that IP_3R channels release Ca^{2+} in the perinuclear region, or directly into the nucleus as a tonic leak (80) or when activated by IP_3 (165). However, the Ca^{2+} concentration in the nucleus is still heavily influenced by the Ca^{2+} concentration in the cytosol (80).

Previously (58), we investigated how changes to cytosolic Ca^{2+} dynamics could contribute to activating the hypertrophic pathway. Here we aim to model the movement of cytosolic Ca^{2+} signals into the nucleus and detail the differences between ETC and ECC signals once they reach the nucleus to better elucidate how hypertrophic gene regulatory mechanisms can respond to one but appear insensitive to the other.

3.1.4 Calcium buffers within the nucleus

The nuclei of cardiomyocytes contain a variety of proteins and molecules that either depend on, or interact with, Ca^{2+}. We divide these proteins and molecules into five main categories (44).

Helix-loop-helix Ca^{2+}-binding proteins

These are described as 'proteins which possess one or more E-F hand helix-loop-helix structural motifs'. The helix-loop-helix structure allows dimerisation and DNA binding. It characterises a large family of dimerising transcription factors. Of these proteins, calmodulin (CaM) is one of the most well-studied for its interactions with Ca^{2+}. Calmodulin is ubiquitous within cardiomyocytes, playing various roles within the dyads, the bulk cytosol, and the nucleus. Calmodulin is found almost as universally as Ca^{2+}, as a Ca^{2+} signal decoder. It is involved in the activation of a whole family of protein kinases; regulation of RyRs; dephosphorylation of NFAT; and, in other cell types, cell-cycle progression.

In the cytosol, calmodulin has been measured at 6 μM with a Ca^{2+} dissociation constant of $0.1 - 1$ μM. Bers (10) uses the dissociation constant 7 μM and concentration 24 μM when treating the whole protein as one unit (instead of taking into account each subunit). Calmodulin concentrations in the cytosol and nucleus vary. It is concentrated at and bound to Z-lines in diastole with only around $50 - 75$ nM unbound. When $[Ca^{2+}]$ increases, it moves and binds to proteins in the nucleus, potentially in conjunction with a 'protein partner' (164). Fluorescence analysis showed the intensity of calmodulin in the nucleus at 500 nM $[Ca^{2+}]$ to be twice the concentration of calmodulin in the cytosol at 100 nM $[Ca^{2+}]$ (diastolic concentration). This indicates that calmodulin in the nucleus could be far higher than the concentration of unbound calmodulin would suggest when $[Ca^{2+}]$ is elevated.

Other cardiac proteins in this category include calpain – which alters the function of other proteins, MLC2 – a myosin subunit, and troponin C. For comparison, troponin C and myosin, have Ca^{2+} dissociation constants 0.6 μM and 0.033 μM respectively however these are not found in the nucleus.

Annexins

The second category of Ca^{2+} buffers present in the nucleus is known as annexins. These have phospholipid and Ca^{2+}-dependent binding sites and are found on the SR membrane. They may affect the structure and function of membranes and the cytoskeleton. Bers (9, 10) reports the dissociation constant of the SR membrane as 0.3 μM and estimates the concentration of binding sites to be 15 μM. The NE is contiguous with the SR with very similar embedded proteins. It is likely to have similar Ca^{2+} buffering properties.

Calreticulin-like proteins

The third is tentatively labelled 'calreticulin-like proteins' in Gilchrist et al. (44). They are typically able to bind to a large amount of Ca^{2+} but with low affinity. Calreticulin itself is most commonly studied in the ER/SR lumen but is also found in the cardiac nucleus where it is thought to play a role in transcriptional regulation (86) and NPC function (35). Each molecule is known to bind one calcium ion with high affinity and approximately 25 calcium ions with low affinity (10).

ATP

Along with these proteins, ATP is a known buffer of Ca^{2+}. The diffusion coefficient of ATP in the cytosol of myocytes is 0.14 $\mu m^2/ms$ (74). Kushmerick and Podolsky (74) that the diffusion coefficient of ATP appeared to be affected more by physical interactions than chemical so it is likely to be affected mostly by crowding in the nucleus as well. The dissociation constant is 200 μM in the cytosol but the concentration oscillates with the contraction cycle so is hard to predict. The maximum cytosolic ATP concentration is 5 mM (10) however it is likely that the concentration of ATP is lower in the nucleus as the majority of the energy requirements of a cardiomyocyte occur in the cytosol.

Chromatin

Lastly, Ca^{2+} has also been shown to bind to and alter the structure of chromatin (26). However, the binding affinity is low enough that even at the concentrations found in the nucleus, it is unlikely that chromatin buffering would affect Ca^{2+} dynamics (73).

Ca^{2+} buffers in the cardiomyocyte nucleus

Buffer	**Concentration** (μM)	**D** ($\mu m^2/ms$)	**K_b** (μM)	**k_{on}** ($\mu M^{-1}s^{-1}$)	**k_{off}** (s^{-1})
Calmodulin	$50-75\times10^{-3}$ [164] (free) 24 [10] (total)	$2-40$ [84]	7 [10]	34 [10]	238 [10]
SR (or NE)	15 [10]	0	0.3 [10]	100 [10]	30 [10]
Calreticulin (Site C)	7.2×10^4 [93]	0.027 [93]	2×10^3 [93, 2]	1×10^{-4} [93]	0.2 [93]
Calreticulin (Site P)	3.6×10^3 [93]	0.027 [93]	10 [93, 2]	1×10^8 [93]	1×10^9 [93]
ATP	5×10^3 (max.) [10]	0.14 [74]	200 [10]	–	–

Table 3.1: Non-exhaustive list of buffers we expect to be present in the nucleus and what we know about them. All buffer parameters listed are for the cytosol of myocytes except for the calreticulin parameters which are based on experiments on the ER of E. Coli and RBL (cancerous rat basophil cell-line) cells. Values are likely to differ within the nucleus due to different pH and protein contents and density.

The characteristics of known nuclear buffers are summarised in Table 3.1. Using diffusion models, and taking into account the effects of buffers, it is possible to estimate the proportion of the Ca^{2+} signal that is diffusion dependent vs gating dependent.

3.2 Experimental measurement of nuclear Ca^{2+} dynamics

Confocal line-scan images of Ca^{2+} dynamics in adult rat ventricular myocytes (ARVMs) were recorded at the Babraham Institute by Greg Bass, a PhD student in the Systems Biology Lab (unpublished data (4)). The experiments were performed on male Wistar rats. Rat hearts were extracted to recover myocytes and acclimated to a Langendorff perfusion system. Cardiac tissue was then enzymatically digested before being attached to laminin-coated coverslips.

The coverslips were immersed for 30 minutes in a solution of Fluo4-AM, a Ca^{2+}-indicator dye. The cells were transferred to a HEPES solution for another 30 minutes to allow the dye to de-esterify, trapping it within the cells. Then, the coverslips were sealed into an electrode dish. The dish was attached to a pulse stimulator box to be electrically paced at 0.3 Hz at 80 V, an order of magnitude lower than in physiological conditions to keep the cells alive for longer.

Intracellular Ca^{2+} transients were imaged using a two-photon microscope. The microscope was aligned to simultaneously measure cytoplasmic and nucleoplasmic $[Ca^{2+}]$ as functions of time. These were then imaged with a confocal scanning microscope at 3.8 MHz to generate 3D image stacks of both longitudinally (line-scan oriented along the z-axis) and transversally (line-scan oriented along the r-axis) oriented cells (See Figure 3.4). The 3D stacks were deconvolved with an appropriate point spread function derived from a fluorescent bead stack by Bass (4).

Bass (4) also measured the length and width of the nuclei in dark-field images of eight of these cardiac cells. The average length of the major axis in these nuclei was 19.08 μm with standard deviation 5.06 μm. The minor axes were measured as the largest diameter in each nucleus and the diameter of the perpendicular minor axis. These values were measured to be 4.76 ± 0.68 μm and 3.49 ± 0.64 μm respectively. The average minor axis is then 4.13 μm. These values were used as the dimensions of the nuclei in the following analysis of the recorded line-scans (See Figure 3.1 for an idea of nucleus shape).

3.2.1 Experimental observation of calcium dynamics in the nucleus

Line-scan data of ARVMs was examined at various angles to the long axis of the nucleus. The line-scans passed through the nucleus and recorded $[Ca^{2+}]$ across the breadth of the cell. Some examples of the cell nuclei measured by Bass (4), showing the intensity of the Fluo4-AM dye in the first 1000ms after cell stimulation, are shown in Figure 3.2. The fluorescent data has been smoothed, time-wise using a matlab 'bior1.1' wavelet filter which allows us to remove some of the noise inherent in the fluorescent signal with little effect on the larger transient features we are interested in. I performed the data analysis and smoothing. We can see the timing of the $[Ca^{2+}]$ peaks and troughs from this data, directly measuring the time to peak (TTP). We can only estimate $[Ca^{2+}]$ from this data because the fluorescent signal was not calibrated during the experimental study. However, the fluorescent intensity of Fluo4-AM is approximately linear over the physiological range of $[Ca^{2+}]$ in cardiomyocytes (148, 80). We can use this to calculate the approximate FDHM in each cell from the normalised fluorescence. I wrote Matlab scripts to automate each of these measurements. TTP was measured as the time from the initial rise in the smoothed data to the time of maximum intensity

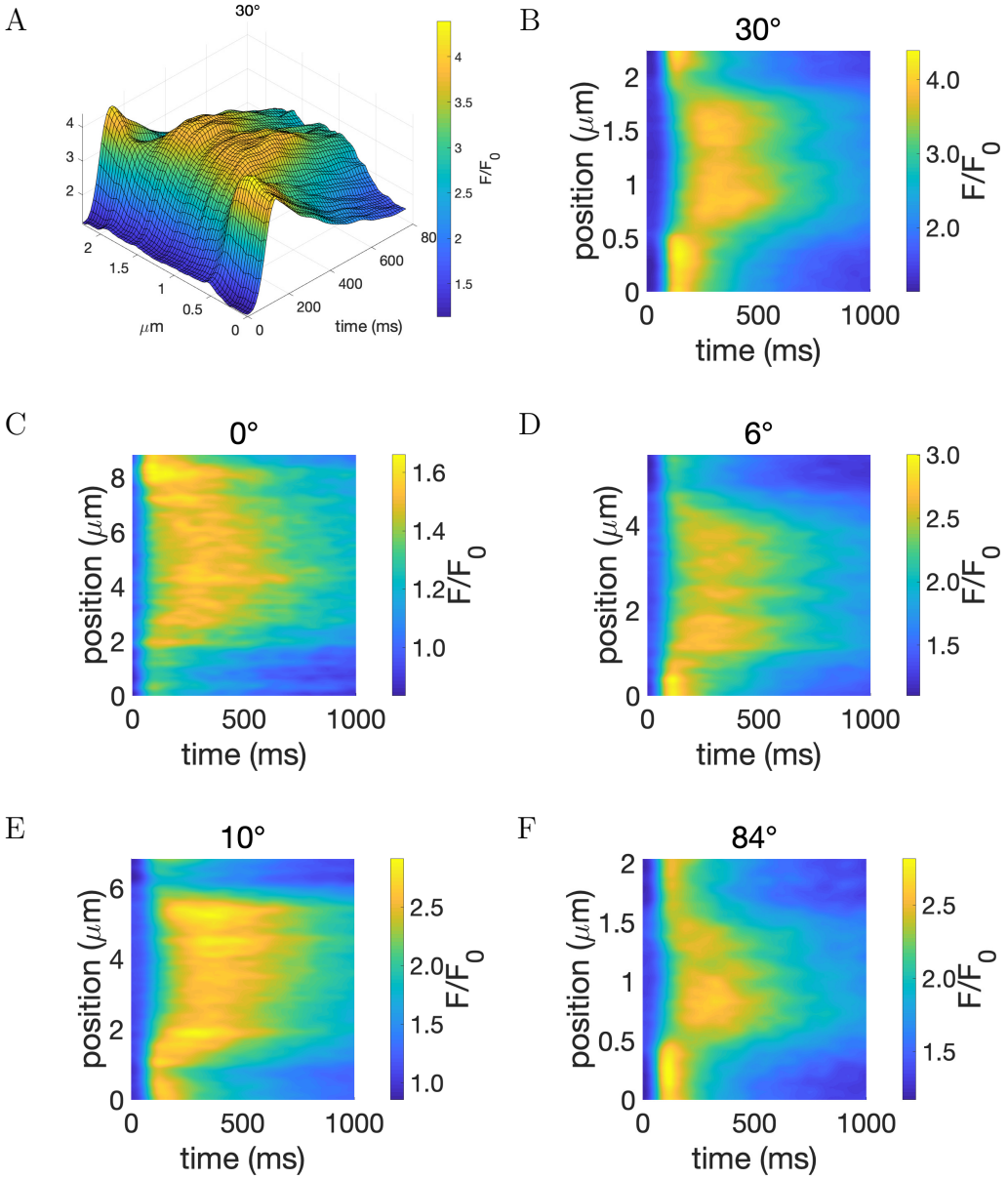

Figure 3.2: Line-scan data of $[Ca^{2+}]$ in the nucleus of rat LVM cells during the first 800ms after electrical cell stimulation to induce a global Ca^{2+} transient, mimicking Ca^{2+} dynamics in the cell. The measurements were taken at varying angles to the long axis of the nucleus, labelled above each figure. (B)-(F) show heatmaps of $[Ca^{2+}]$ across the line of the laser over time. While (A) shows the same line-scan as (B) as a mesh surface. These line-scans have been smoothed using a wavelet filter to make interpretation easier.

during each transient. FDHM was measured as the duration that each transient remained at an intensity greater than at least halfway between the maximum and minimum intensity values of that transient. Due to the amount of noise in the data, if the intensity dropped only briefly (≤ 1 datapoint) below that threshold, we counted the drop in our measure of duration. The average FDHM in the cytosol of measured cells was 431.0±172.3ms. The average TTP was 143.0±43.0ms. In the nucleus, the average FDHM was 853.5 ± 179.5ms and the average TTP was 371.7 ± 84.4ms. See Figure 3.3A, 3.3B, and 3.3C for a summary of the cytosolic and nuclear transients in each cell.

In general, we see $[Ca^{2+}]$ rising fastest at the boundary of the nucleus in each cell. However, in some nuclei, Figure 3.2C and D in particular, we see an almost instantaneous, uniform increase in $[Ca^{2+}]$ across the whole nucleus with a rise in $[Ca^{2+}]$ in the cytosol (visible in the 0.5 μm at the edges of each plot). As the line-scan for these two plots was taken close to parallel with the long axis of the nucleus, we assume that this rise is due to diffusion perpendicular to this axis, in the radial direction of the nucleus.

3.3 Methods

We aim to develop a minimalistic, biophysical model that describes $[Ca^{2+}]$ dynamics within the nucleus during a cell-side Ca^{2+} transient. We construct this model through numerical methods based on analysis of Ca^{2+} line-scan data of electrically paced rat left ventricular myocytes and known properties of the nucleus.

3.3.1 1D simulation

We model Ca^{2+} diffusion from the cytosol into the nucleus, through the NE (See Figure 3.4). The nuclei of ventricular myocytes are roughly ellipsoidal in shape with conical spindles of mitochondria at each end of the major axis (36). While these mitochondrial spindles could play a role in extending the perinuclear Ca^{2+} transient, the Ca^{2+} conductance of mitochondria is low (85), particularly in the perinuclear region (83), indicating that the majority of Ca^{2+} that diffuses into the nucleus enters from the rest of the NE, which is unobstructed by mitochondria. Hence, we approximate the nucleus as a cylinder of radius a with diffusion only through the curved surface (See Figure 3.5). For simplitcity, we calculate the

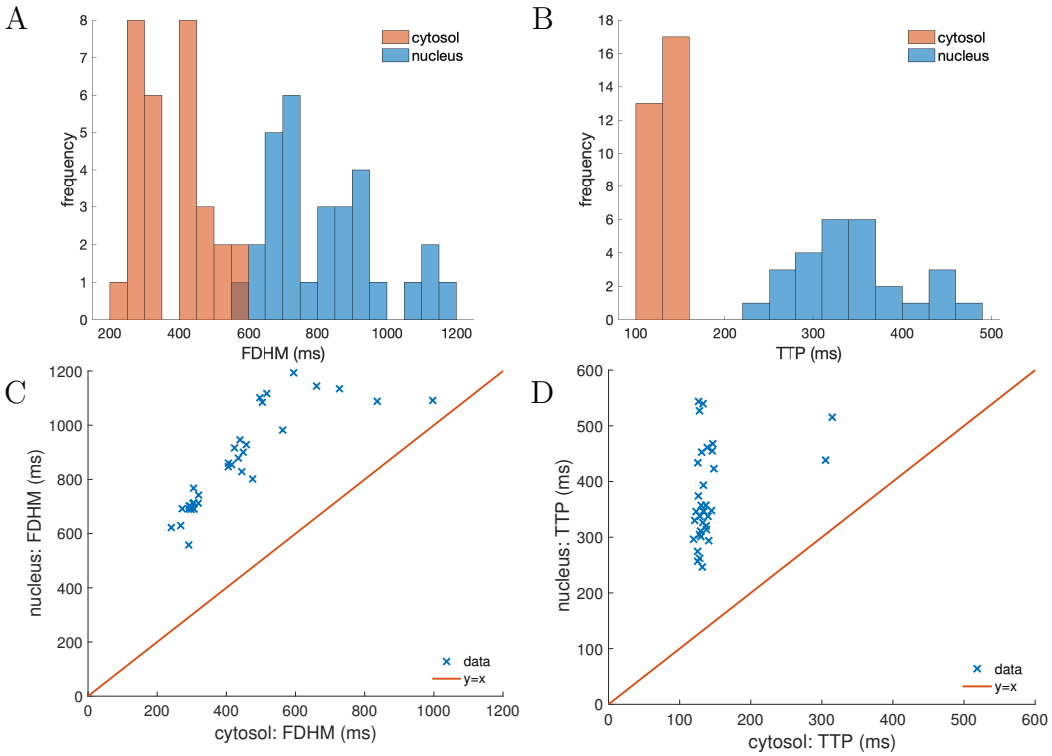

Figure 3.3: (A) Full duration at half maximum (FDHM) and (B) time to peak (TTP) of each Ca^{2+} transient in line-scan experiments. (C) Comparison of FDHM in the cytosol with FDHM in the nucleus in each cell for each transient. (D) Comparison of TTP in the cytosol with TTP in the nucleus in each cell for each transient. Data shown here was collected from 8 nuclei in 6 different cells, each paced five times.

$[Ca^{2+}]$ along a line through the centre of the nucleus. We start with the diffusion equation:

$$\frac{\partial c}{\partial t} = \nabla \left(D_c c \nabla c \right). \tag{3.1}$$

Here D_c is the Ca^{2+} diffusion coefficient and c is the Ca^{2+} concentration.

The 1D cylindrical diffusion equation for the nucleus is then:

$$\frac{\partial c}{\partial t} = D_c \left(\frac{\partial^2 c}{\partial r^2} + \frac{1}{r} \frac{\partial c}{\partial r} \right), \tag{3.2}$$

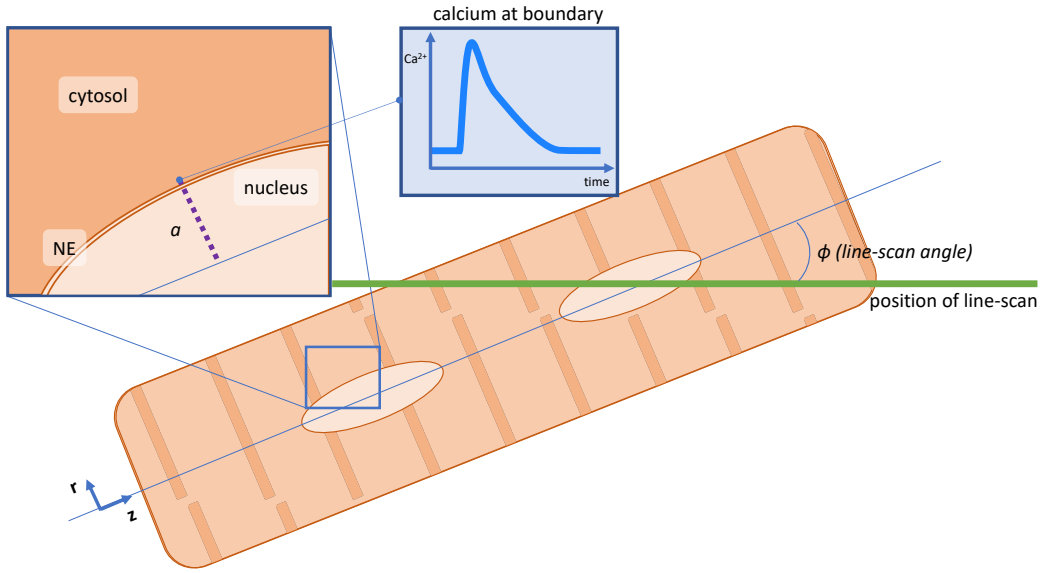

Figure 3.4: Schematic cross-section of a cardiomyocyte showing the nuclei, and an example of the Ca^{2+} transient expected at the nuclear envelops (NE) during ECC. The dotted line in the cut-out indicates the section modelled in this 1D study.

with initial boundary conditions:

$$c(r, 0) = c_0, \tag{3.3a}$$

$$c(a, t) = q(t). \tag{3.3b}$$

Here c_0 is the initial uniform Ca^{2+} concentration in the nucleus, and $q(t)$ is the Ca^{2+} concentration at the nuclear boundary.

Details on the number of buffers and their characteristics within the nucleus are sparse in the literature making it challenging to incorporate them in the model. The number of parameters introduced into our equations with each buffer means that estimating their values from just fluorescent Ca^{2+} images is impossible. Therefore, the approach we will take is to consider the influence of a single buffer on the diffusion of Ca^{2+} into the nucleus and compare it to simulated diffusion without buffers and experimental data on nuclear Ca^{2+} diffusion to determine an approximation of the buffers present.

In the case of fast dynamics, and buffering in excess or low association, we can use Equation 3.2 with D_c replaced by an effective diffusion coefficient, D_{eff}, determined by the buffers present.

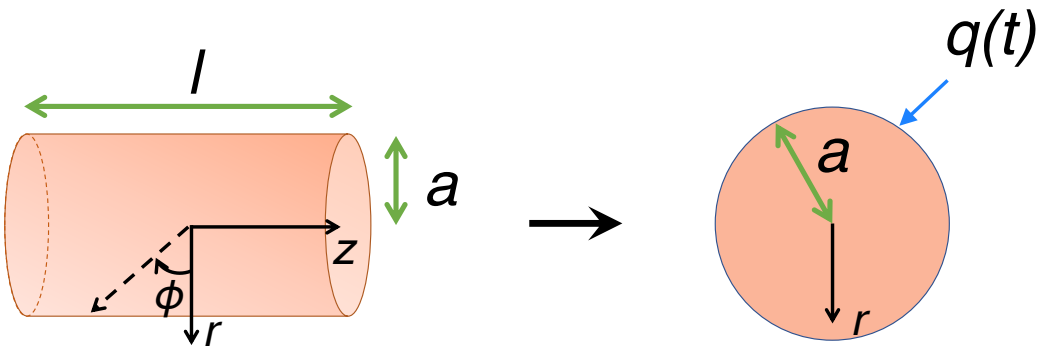

Figure 3.5: We approximate the nucleus as a cylinder of radius, a, and $[Ca^{2+}]$, $q(t)$, at the boundary. The cell structure and radial symmetry of the nucleus allows us to ignore the other dimensions and model this as a 1D system.

Starting with the equations for diffusion of Ca^{2+}, c, and a Ca^{2+}-bound buffer, b, we have

$$\frac{\partial c}{\partial t} = D_c \nabla^2 c + k_- b - k_+ c(b_T - b) + f(c) \tag{3.4}$$

$$\frac{\partial b}{\partial t} = D_b \nabla^2 b - k_- b + k_+ c(b_T - b) \tag{3.5}$$

Here k_- and k_+ are the binding and unbinding rates of the buffer, b_T is the total (free and Ca^{2+}-bound) buffer concentration, $f(c)$ describes all other reactions involving free Ca^{2+}, and D_b is the diffusion coefficient of the buffer.

If the buffer binding rates are much faster than the free Ca^{2+} dynamics, i.e. $k_-,\ k_+ \gg \nabla^2 c, f(c)$, we can assume a quasi-steady state for the concentration of bound Ca^{2+}, b, such that

$$k_- b - k_+ c(b_T - b) = 0$$

$$\implies b = \frac{b_T c}{K_b + c}, \qquad \text{where } \mathrm{K_b} = \frac{\mathrm{k_-}}{\mathrm{k_+}} \tag{3.6}$$

Combining Equations 3.4 and 3.5 we have the 'slow' part of this system

$$\frac{\partial}{\partial t}(c+b) = D_c\nabla^2 c + D_b\nabla^2 b + f(c) \tag{3.7}$$

If we also find that the buffer has a low Ca^{2+} binding affinity and the concentration of calcium is low, i.e. $K_b >> c$, as is the case with several of the mobile buffers in Table 3.1, we can further approximate b as

$$b = \frac{b_T c}{K_b} \text{where } \mathrm{K_b} = \frac{\mathrm{k_-}}{\mathrm{k_+}} >> \mathrm{c}. \tag{3.8}$$

Substituting this approximation into Equation 3.7, we arrive at:

$$\frac{\partial}{\partial t}\left(c + \frac{b_T c}{K_b}\right) = D_c\nabla^2 c + D_b\nabla^2\left(\frac{b_T c}{K_b}\right) + f(c) \tag{3.9}$$

$$\left(1 + \frac{b_T}{K_b}\right)\frac{\partial c}{\partial t} = \left(D_c + \frac{D_b b_T}{K_b}\right)\nabla^2 c + f(c) \tag{3.10}$$

$$\frac{\partial c}{\partial t} = \frac{D_c + D_b\frac{b_T}{K_b}}{1 + \frac{b_T}{K_b}}\nabla^2 c + f(c) \tag{3.11}$$

Our expression for nuclear calcium diffusion in the presence of one of these buffers is then simply

$$\frac{\partial c}{\partial t} = D_{\text{eff}}\left(\frac{\partial^2 c}{\partial r^2} + \frac{1}{r}\frac{\partial c}{\partial r}\right), \tag{3.12}$$

$$\text{where } \mathrm{D_{eff}} = \frac{\mathrm{D_c} + \mathrm{D_b}\frac{\mathrm{b_T}}{\mathrm{K_b}}}{1 + \frac{\mathrm{b_T}}{\mathrm{K_b}}} \tag{3.13}$$

In our simulations, we will use the more generic Equation 3.7 to explore those buffers whose effect on Ca^{2+} diffusion is nonlinear. In 1D cylindrical coordinates, ignoring any other reactions involving free Ca^{2+} ($f(c)$), this becomes:

$$\frac{\partial}{\partial t}(c + \frac{b_T c}{K_b + c}) = \frac{1}{r}\frac{\partial}{\partial r}\left(rD_c\frac{\partial c}{\partial r}\right) + \frac{1}{r}\frac{\partial}{\partial r}\left(rD_b\frac{\partial}{\partial r}\frac{b_T c}{K_b + c}\right) \tag{3.14}$$

$$\frac{\partial c}{\partial t} + \frac{b_T K_b + b_T c}{(K_b + c)^2}\frac{\partial c}{\partial t} - \frac{b_T c}{(K_b + c)^2}\frac{\partial c}{\partial t} = \frac{1}{r}\frac{\partial}{\partial r}\left(rD_c\frac{\partial c}{\partial r}\right) + \frac{1}{r}\frac{\partial}{\partial r}\left(rD_b\left(\frac{b_T K_b + b_T c}{(K_b + c)^2}\frac{\partial c}{\partial t} - \frac{b_T c}{(K_b + c)^2}\frac{\partial c}{\partial r}\right)\right) \tag{3.15}$$

$$\frac{\partial}{\partial t}\left(c + \frac{b_T K_b}{(K_b + c)^2}\right) = \frac{1}{r}\frac{\partial}{\partial r}\left(rD_c\frac{\partial c}{\partial r}\right) + \frac{1}{r}\frac{\partial}{\partial r}\left(rD_b\left(\frac{b_T K_b}{(K_b + c)^2}\frac{\partial c}{\partial r}\right)\right) \tag{3.16}$$

$$(1 + \theta(c))\frac{\partial c}{\partial t} = \frac{1}{r}\frac{\partial}{\partial r}\left(r\left(D_c + D_b\theta(c)\right)\frac{\partial c}{\partial r}\right) \tag{3.17}$$

where $\theta(c) = \frac{b_T K_b}{(K_b+c)^2}$, D_b is the diffusion coefficient of the buffer, b_T is the total concentration of the buffer, and K_b is the dissociation constant of the buffer. Assuming a uniform concentration of Ca^{2+} in and around the nucleus prior to cell excitation and Ca^{2+} release, the boundary conditions are:

$$c(r, 0) = c_0 \tag{3.18a}$$

$$c(a, t) = q(t) \tag{3.18b}$$

We approximate $q(t)$ from the data obtained in Section 3.2. Immediately prior to the initiation of the Ca^{2+} transient, we assume that $q(0) = c_0$ is constant over r.

3.3.2 Model Implementation

To ensure a realistic, easily integrable boundary condition, $q(t)$, five cytosolic transients, recorded by Bass (4), from each of eight cells (making a total of 40 transients) were analysed and smoothed and the closest to the median approximated with a spline interpolation using the MATLAB 'fit' function with the 'smoothingspline' algorithm (See Figure 3.6). Interpolation points were placed

1. immediately before the initial rise in $[Ca^{2+}]$ (at the last point before the point of maximum rise in $[Ca^{2+}]$ where the difference between pixels is less than the median absolute difference between pixels in the transient),

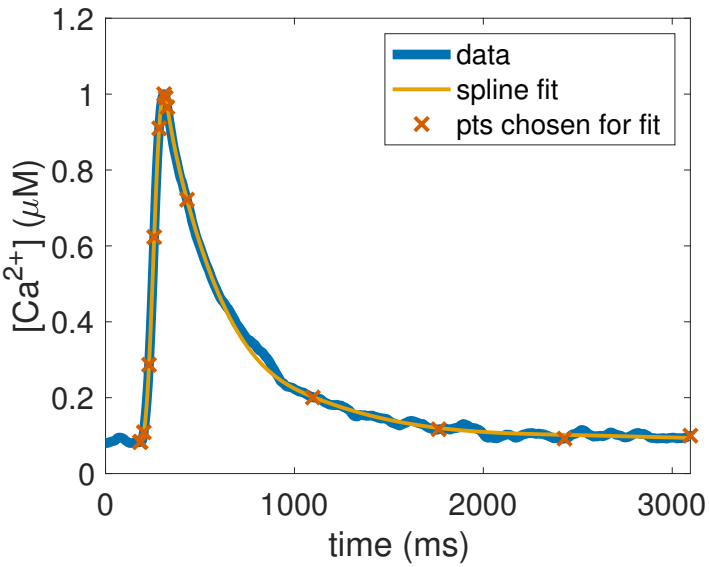

Figure 3.6: A representative, experimental, cytosolic Ca^{2+} transient (blue), with the spline approximation (yellow), and the interpolating points used to fit the spline (orange crosses).

2. at the initial rise (at the first point where the difference between pixels is greater than 0.001 F/F_0),
3. $\approx$ 4 ms after the first point,
4. halfway between that and the maximum rise in $[Ca^{2+}]$,
5. at the point of steepest ascent in $[Ca^{2+}]$ (max $\left(\frac{\partial c}{\partial t}\right)$),
6. halfway between that and the peak in $[Ca^{2+}]$,
7. at the peak in $[Ca^{2+}]$,
8. halfway between that and the point of steepest descent in $[Ca^{2+}]$,
9. at the point of steepest descent (min $\left(\frac{\partial c}{\partial t}\right)$),
10. 104 ms after the halfway point between peak $[Ca^{2+}]$ and maximum fall in $[Ca^{2+}]$,
11. one quarter of the way between that and the end of the transient,
12. halfway between the halfway point between peak $[Ca^{2+}]$ and maximum fall in $[Ca^{2+}]$ and the end of the transient,

13. three quarters of the way between the halfway point between peak $[Ca^{2+}]$ and maximum fall in $[Ca^{2+}]$ and the end of the transient,

14. at the end of the transient – after the $[Ca^{2+}]$ has returned to diastolic levels (3 s after the initial rise in $[Ca^{2+}]$).

To avoid spurious oscillations without having to add too many interpolation points, the time between a transient reaching the diastolic Ca^{2+} concentration and the next Ca^{2+} transient was approximated as a constant concentration. The fluorescent line-scan images were not calibrated so each cytosolic transient was scaled to peak at 1 μM and dip to 0.1 μM – approximately what one would expect in ECC.

To simulate the effect of changes in nuclear protein complex (NPC) conductance, we can limit the entry of Ca^{2+} into the nucleus by introducing an NPC conductance parameter, n, to the model to alter the boundary conditions. Equation 3.18a and Equation 3.18b then become:

$$c(r, 0) = c_0 \tag{3.19a}$$

$$c(a, t) = nq(t) \tag{3.19b}$$

When modifying the original spline (approximated from experimental data), $q_0(t)$, to simulate altered cytosolic $[Ca^{2+}]$ amplitude, we stretch or flatten the spline to alter the amplitude by a factor, h, to obtain a new boundary condition $q(t)$ with the same resting $[Ca^{2+}]$:

$$q(t) = h(q_0(t) - \min(q_0)) + \min(q_0) \tag{3.20}$$

When modifying $q_0(t)$ to simulate altered cytosolic $[Ca^{2+}]$ FDHM, we obtain a new boundary condition $q(t)$ by stretching or shortening the spline to alter the FDHM by a factor, w, after the peak time, t_{peak}, without changing the TTP:

$$q(t) = \begin{cases} q_0(t) & t \leq t_{\text{peak}} \\ h(q_0(t_{\text{peak}} + w(t - t_{\text{peak}})) - \min(q_0)) + \min(q_0) & t > t_{\text{peak}} \end{cases} \tag{3.21}$$

The full system we are simulating is thus

$$(1 + \theta(c)) \frac{\partial c}{\partial t} = \frac{1}{r} \frac{\partial}{\partial r} \left(r \left(D_c + D_b \theta(c) \right) \frac{\partial c}{\partial r} \right) \tag{3.22}$$

with boundary conditions

$$c(r,0) = c_0 \tag{3.23a}$$

$$c(a,t) = nq(t) \tag{3.23b}$$

where

$$q(t) = \begin{cases} h(q_0(t) - \min(q_0(t))) + \min(q_0(t)) & t \leq t_{\text{peak}} \\ q_0(t_{\text{peak}} + w(t - t_{\text{peak}})) & t > t_{\text{peak}} \end{cases} \tag{3.24}$$

In this chapter, we set $a = 2$ μm, approximately the average radius of the measured nucleii, unless otherwise specified. When there we ignore the effect of NE conductance on Ca^{2+} movement, $n = 1$. To simulate the effect of the measured cytosolic transient, we set $h = 1, w = 1$. If there are no buffers, $b_T = 0$.

The model (Equation 3.22) was implemented in MATLAB 2019a (The MathWorks Inc., Natick, Massachusetts) using the *pdepe* function. Code can be found at git@github.com:hilaryh/Nucleus.git. The FDHM, TTP, and maximum $[Ca^{2+}]$ amplitude at the centre of the nucleus were determined for each simulation (See Figure 3.7). In this chapter, we show only simulations based on an approximation of Figure 3.2D.

3.3.3 Output metrics

The two main output metrics we examine in this chapter are full duration at half maximum (FDHM) and time to peak (TTP). Although we could not accurately compare the $[Ca^{2+}]$ with the data, we also look at the maximum $[Ca^{2+}]$ reached by the transient at the centre of the nucleus (Max Ca^{2+}).

As depicted in Figure 3.7, the FDHM was measured as the duration for which the concentration of the simulated Ca^{2+} transient was higher than the midpoint between Max Ca^{2+} and c_0. The TTP was measured as the time between initiation of the cytosolic transient and the time at which Max Ca^{2+} was achieved.

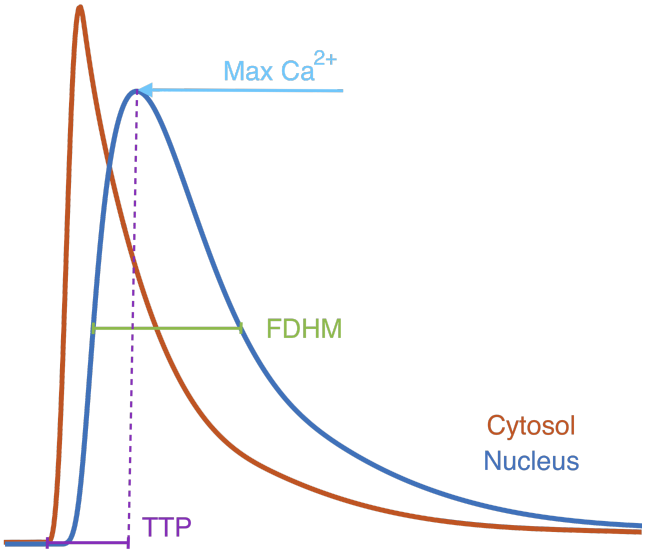

Figure 3.7: Aspects of the nuclear Ca^{2+} transient that were used to fit parameters and analyse model solutions. While the data we analysed wasn't calibrated to allow for calculation of the exact Ca^{2+} concentration from the fluorescence intensity values, we were still able to compare the FDHM and TTP of the simulations with fluorescent data (Figure 3.3). The maximum Ca^{2+} concentration in the nucleus as a proportion of the maximum Ca^{2+} concentration in the cytosol was used to compare between simulations.

3.4 Results

3.4.1 The effective diffusion coefficient in the nucleus is approximately 0.0174 $\mu m^2/ms$ at physiological Ca^{2+} concentrations

We can naively estimate the effective diffusion coefficient from the TTP and FDHM of our recorded Ca^{2+} transients using our base diffusion model (Equation 3.2). In doing so, we obtain a different estimate of D_{eff} from the TTP and the FDHM (See Figure 3.8). This estimate assumes approximately linear diffusion in the physiological range of Ca^{2+} concentrations in the nucleus and is not able to fully reproduce the nuclear transients we see in the data (See Figure 3.10). Collating the D_{eff} estimates calculated from the TTP and FDHM of each transient, we find the median D_{eff} is 0.0174 $\mu m^2/ms$. The estimated values for D_{eff} are shown in Figure 3.9. Note that the variance in the estimations from FDHM is much narrower than that of those from TTP. This is likely a result of the greater

TTP variance in the nucleus compared to the variance in the cytosol of the same cell (See Figure 3.3B).

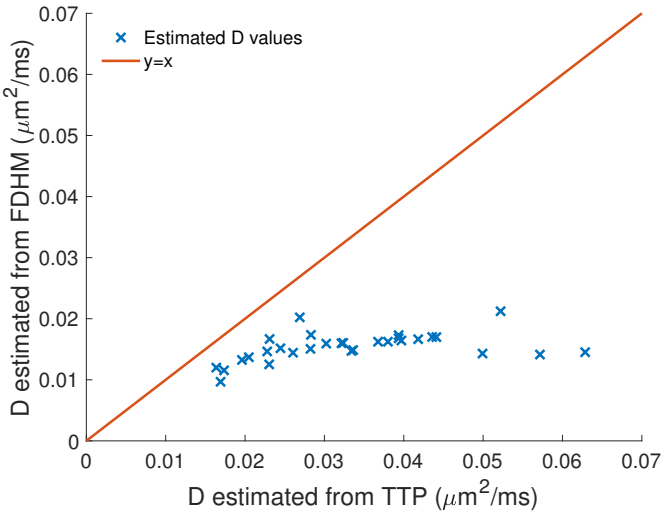

Figure 3.8: Comparison of estimated diffusion coefficient of Ca^{2+} in the nucleus for each transient based on the time to peak vs the FDHM in a single parameter diffusion model. Data shown here was collected from 8 nuclei in 6 different cells, each paced five times.

3.4.2 Calcium dynamics in the nucleus cannot be replicated with unbuffered diffusion

A surprisingly small range of D_c values were estimated based on comparisons of cell cytosolic transients and nuclear FDHM (between approximately 0.01 and 0.02 $\mu m^2/ms$). The range of estimates based on the TTP of $[Ca^{2+}]$ in the nucleus was wider (almost an order of magnitude between 0.01 and 0.7 $\mu m^2/ms$. Ultimately, the TTP and the FDHM of the nuclear transient could not be matched to the data concurrently. Simulations in which the Ca^{2+} concentration in the nucleus peaked at the same time as nuclear $[Ca^{2+}]$ peaked *in vitro* had a comparatively shorter FDHM while simulations in which the FDHM matched the data had a far slower TTP. Figures 3.10 and 3.11 show the differences between the simulation at D_{eff} and line-scan data. To further investigate the causes of this discrepancy, we performed a parameter sensitivity analysis to explore how the FDHM, TTP, and amplitude achieved were affected by the various parameters in our simulations such as the radius of the nucleus, NE conductance, and buffering.

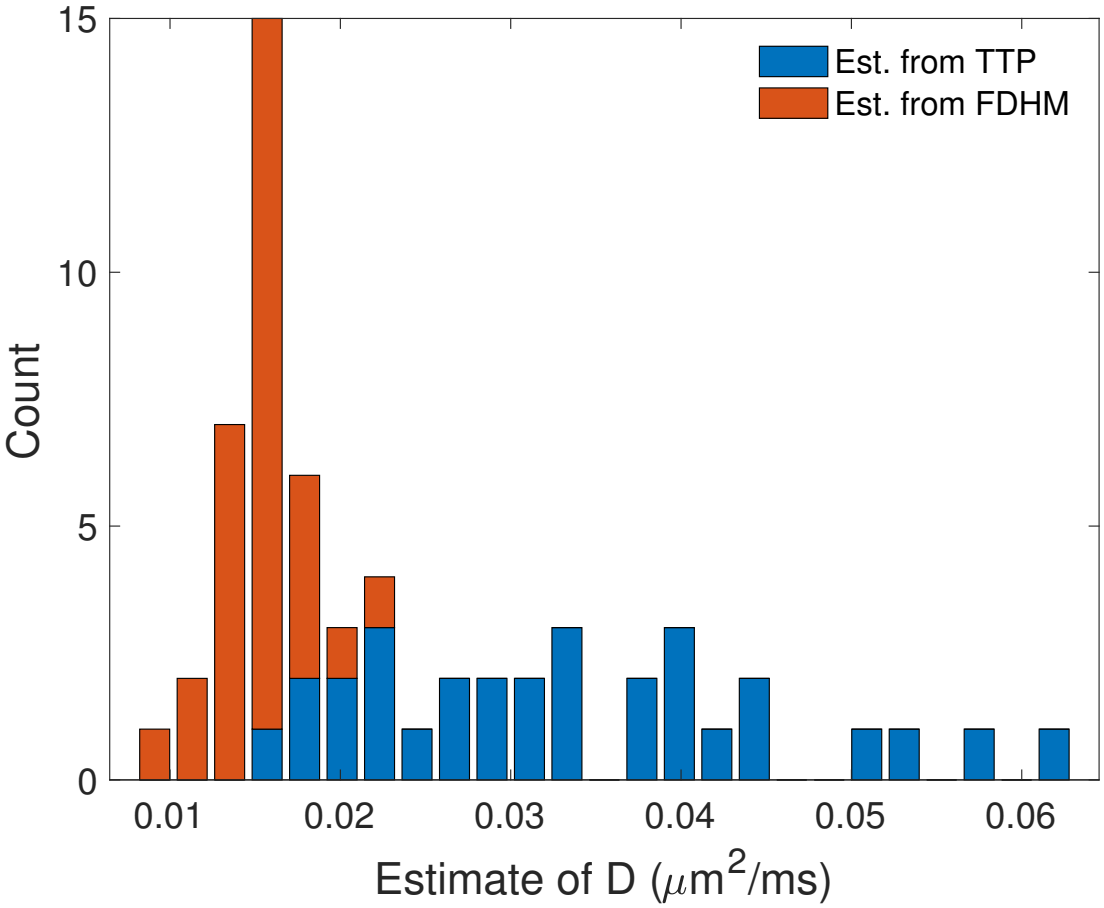

Figure 3.9: The estimated Ca^{2+} diffusion coefficient within the nucleus assuming average nuclear size and given recorded TTP and FDHM of nuclear transients.

For ease of comparison, we compare these qualities at the centre of the nucleus for the majority of this chapter.

3.4.3 Full duration at half maximum

FDHM is most strongly affected by D_c. When the Ca^{2+} diffusion coefficient is high enough, the FDHM of the nuclear Ca^{2+} transient is the same as that of the cytosol. Lowering the Ca^{2+} diffusion coefficient increases the FDHM (See Figure 3.12A & B), up until the point at which the diffusion coefficient is so low that it delays the time it takes to peak more than it delays the time it takes Ca^{2+} to diffuse back out (See Figure 3.12A, B, C, & D). As one would expect, with a low enough diffusion coefficient there is eventually no nuclear Ca^{2+} transient. Smaller Ca^{2+} diffusion coefficients result in a longer TTP and FDHM (See Figure 3.13).

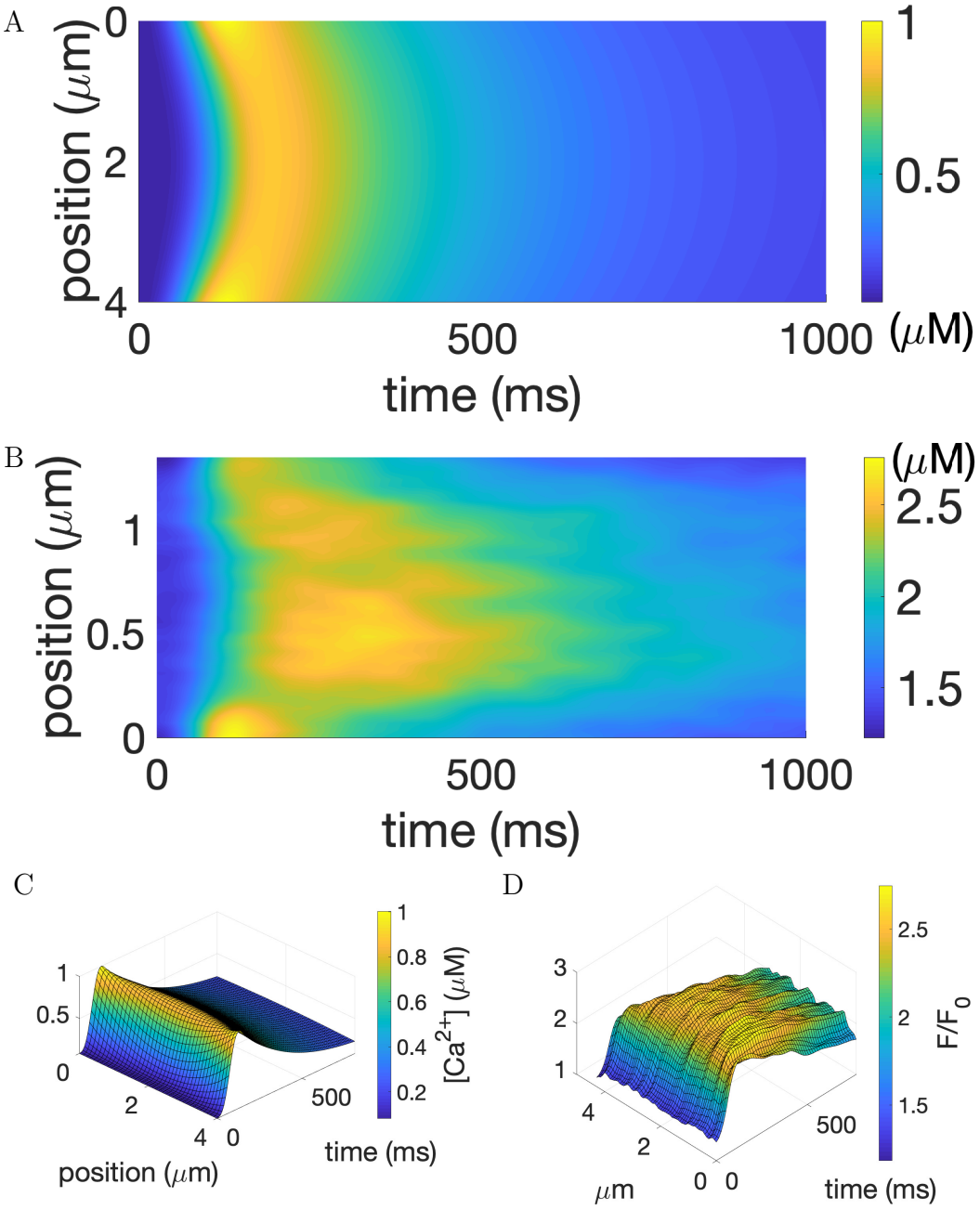

Figure 3.10: Simulation of $[Ca^{2+}]$ diffusion in the nucleus during ECC (A) and line-scan image of $[Ca^{2+}]$ in the nucleus (B). (C) and (D) show surface plots of (A) and (B) respectively. The rise of $[Ca^{2+}]$ in the nucleus (TTP) appears similar in both simulation and data however $[Ca^{2+}]$ appears to decrease faster in the simulation than in the nucleus indicating that something other than diffusion is also affecting nuclear $[Ca^{2+}]$ dynamics.

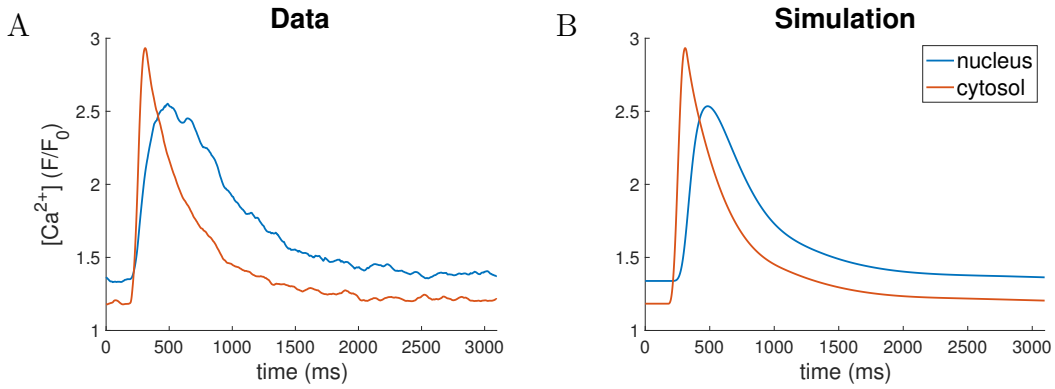

Figure 3.11: (A) The fluorescence intensity in the cytosol and nucleus of a representative cell. This is the average intensity measured over the centre half micron of the nucleus and the average intensity over the cytosol from a line-scan measurement. (B) The spline approximation of the cytosol of the same cell and the projected $[Ca^{2+}]$ in the nucleus using Equation 3.2 to Equation 3.3b. The simulated nuclear transient has been shifted up to better align with the data (i.e. $c_0 = c_{\text{nuc data}}$). As in Figure 3.10, while the TTP match, the FDHM of the simulated data is noticeably shorter. Note that this is uncalibrated fluorescent data so we cannot read too much into the relative amplitudes between the data and simulations.

The radius of the nucleus and the conductivity of the nuclear envelope have little effect on the FDHM. In nuclei with smaller radii, or lower conductivity, the nucleus peaks earlier than in nuclei with larger radii and then drains slowly resulting in long FDHM. However, the difference is comparatively minor (See Figure 3.12).

With the addition of a buffer into the system, we find that the effect of the buffer is dependent on the relative magnitudes of the buffer diffusion coefficient and the Ca^{2+} diffusion coefficient. If the buffer diffusion coefficient is smaller than that of Ca^{2+}, the addition of the buffer generally increases the FDHM of the Ca^{2+} transient in the nucleus, with some exceptions: at higher concentrations of buffer, and when the Ca^{2+} diffusion coefficient is low, i.e. approximately $< 10^{-2}$ $\mu m^2/ms$. If the diffusion coefficients are the same, the buffer has a far smaller effect on the nuclear Ca^{2+} transient. If the buffer diffusion coefficient is greater than the Ca^{2+} diffusion coefficient, the addition of the buffer decreases the FDHM (See Figure 3.14A). As one might expect, stationary buffers have a similar effect on the nuclear Ca^{2+} transient to mobile buffers with low diffusion coefficient (See Figure 3.15A). The primary difference between these two types of buffers is that the stationary buffers can completely stop Ca^{2+} movement when the buffer

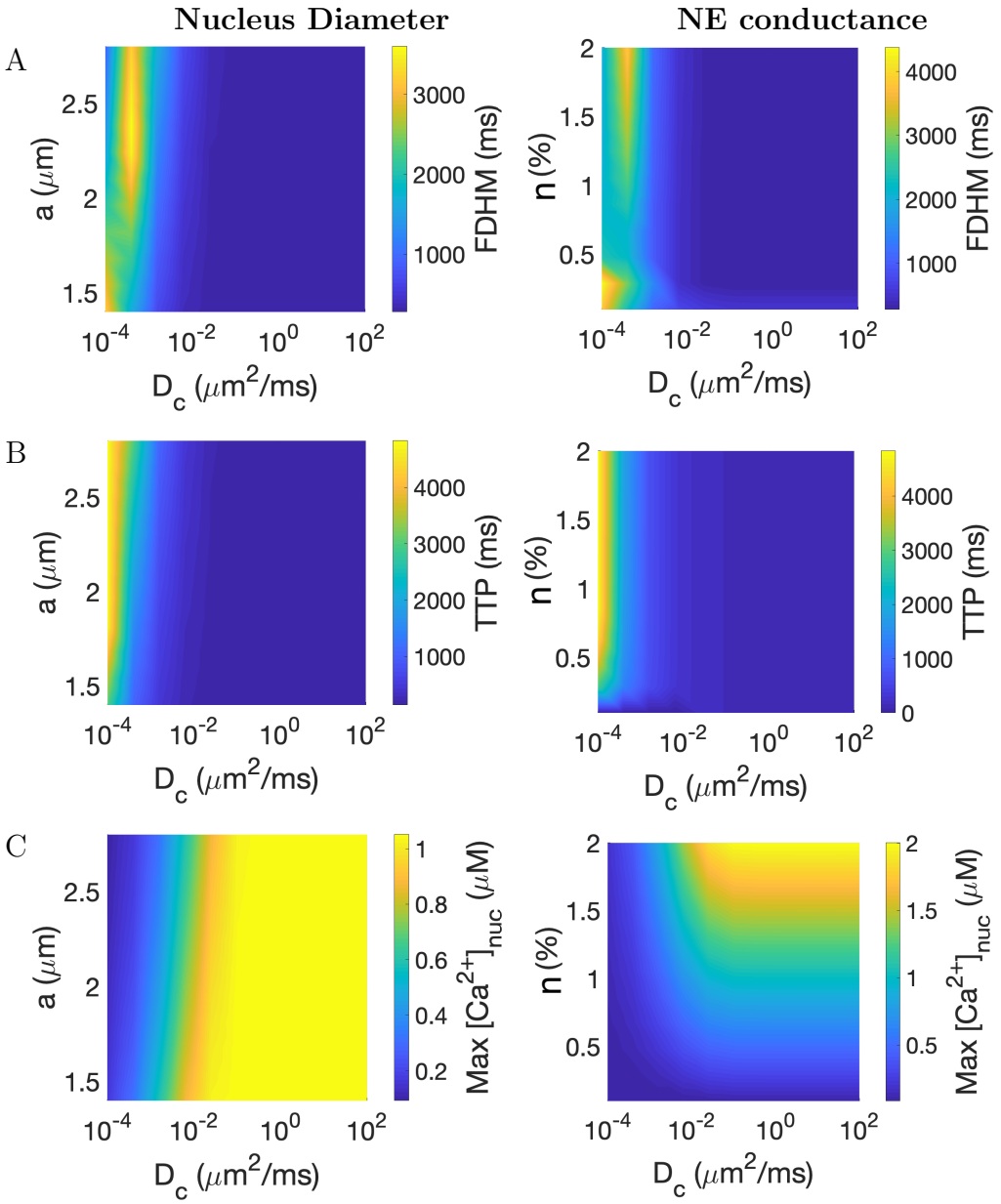

Figure 3.12: The effect of the conductance of the nuclear envelope and diameter of the nucleus on the FDHM, $[Ca^{2+}]$ amplitude, and time to peak at the centre of the nucleus over a range of Ca^{2+} diffusion coefficients. D_c has the greatest effect on the nuclear Ca^{2+} transient. In small nuclei, low a, calcium ions reach the centre of the nucleus faster so that we see a larger peak amplitude than in larger nuclei simulated with the same value of D_c. In larger nuclei, if D_c is too small, calcium ions from cytosolic Ca^{2+} transients barely reach the centre of the nucleus, resulting in a very small FDHM. The Ca^{2+} diffusion coefficient necessary to see the longest FDHM in the nucleus increases with nucleus size. As D_c increases, the nuclear transient becomes closer to the cytosolic input transient (Figure 3.13). Past approximately 0.1 $\mu m^2/ms$, the nucleus is indistinguishable from the cytosol.

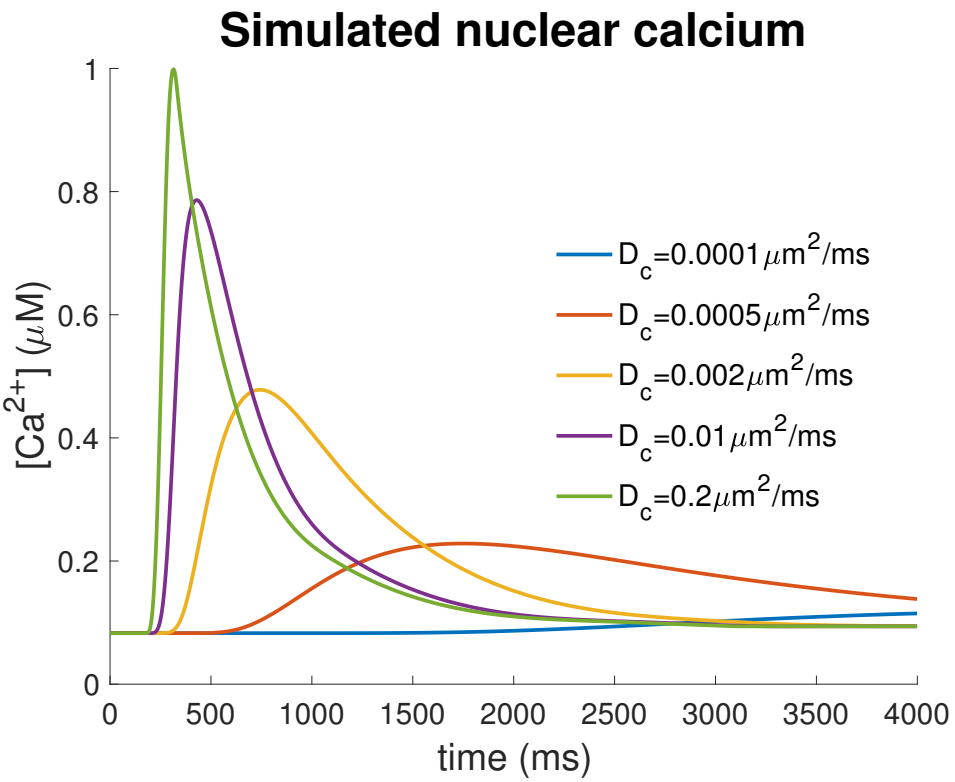

Figure 3.13: Ca^{2+} transients at the centre of the nucleus for different values of D_c. Simulations were all unbuffered with a nucleus radius of 2 μm and no obstruction from the NE, i.e. $n = 1$. As D_c decreases, the amount of Ca^{2+} that reaches the centre of the nucleus decreases and the FDHM increases. The nuclear transient mirrors the cytosolic transient, $q(t)$, when $D_c = 0.2$ $\mu m^2/ms$

concentration is high enough, preventing any Ca^{2+} from reaching the cytosol, whereas slow mobile buffers just slow down Ca^{2+} diffusion to their own speed of diffusion.

We can see from Figure 3.21 that high values of FDHM in the nucleus are achieved only when either the calcium diffusion coefficient or the buffer diffusion coefficient are small. The maximum increase in Ca^{2+} transient FDHM with the addition of a buffer is achieved along a narrow range of K_b and b_T combinations. At the left most edge of each plot in Figure 3.21, we can see the FDHM of the nuclear transient at that D_c without the buffer. In general, as we move right through each plot (b_T increases), the FDHM increases if D_b is smaller than D_c and decreases if D_b is greater than D_c. At $D_b = D_c$, the buffer has a minimal effect on the FDHM of the nuclear Ca^{2+} transient. These dynamics are easier to see in Figure 3.14A. In Figure 3.14A, we see a clear division between when the buffers have little to no effect on the Ca^{2+} transient (the left half of both

plots) and when the buffers are at saturating concentrations (the right half of both plots). The differences visible across the range of saturating concentrations are due to different binding rates (dissociation constants, K_b) leading to different concentrations of Ca^{2+} being bound during saturation.

3.4.4 Time to peak

The effects of each model parameter on the time it takes for the nuclear transient to peak (TTP) are very similar to their effects on the FDHM. At high D_c, the TTP is the same in both the nucleus and the cytosol. At low D_c, it takes longer for Ca^{2+} to diffuse to the centre of the nucleus so the TTP is increased.

Similarly, the radius of the nucleus and the conductance of the NE have little effect. Smaller radii mean that Ca^{2+} reaches the centre of the nucleus faster, hence the TTP decreases. At low enough NE conductance and low D_c, barely any Ca^{2+} makes it to the centre of the nucleus so the TTP is very short but the $[Ca^{2+}]$ amplitude is correspondingly low (See 3.12C & D).

The addition of a buffer increases the TTP if the buffer diffusion coefficient is less than D_c, but decreases it when the buffer diffusion coefficient is greater than D_c (See Figure 3.14B). Stationary buffers also increase the TTP of the nuclear Ca^{2+} transient up until the point where the buffer is at a high enough concentration to soak up all of the incoming Ca^{2+} and prevent it from reaching the cytosol (See Figure 3.15B).

3.4.5 Peak Ca^{2+} concentration

At high values of D_c ($> 10^{-1}$ $\mu m^2/ms$), the Ca^{2+} transient in the nucleus corresponds so closely to the concentration in the cytosol that the difference between them is negligible. The maximum amplitude decreases with lower D_c values but is relatively unaffected by changes in the radius of the nucleus (See Figure 3.12E). In contrast, there is a linear relationship between the maximum amplitude and the conductance of the NE with constant D_c.

Compared to FDHM and TTP, the addition of a buffer has almost the opposite effect on the maximum amplitude.When the buffer diffusion coefficient is greater than the Ca^{2+} diffusion coefficient, the buffer increases the maximum amplitude as Ca^{2+} is carried faster into the nucleus. When the buffer diffusion coefficient is less than the Ca^{2+} diffusion coefficient, the buffer decreases the maximum

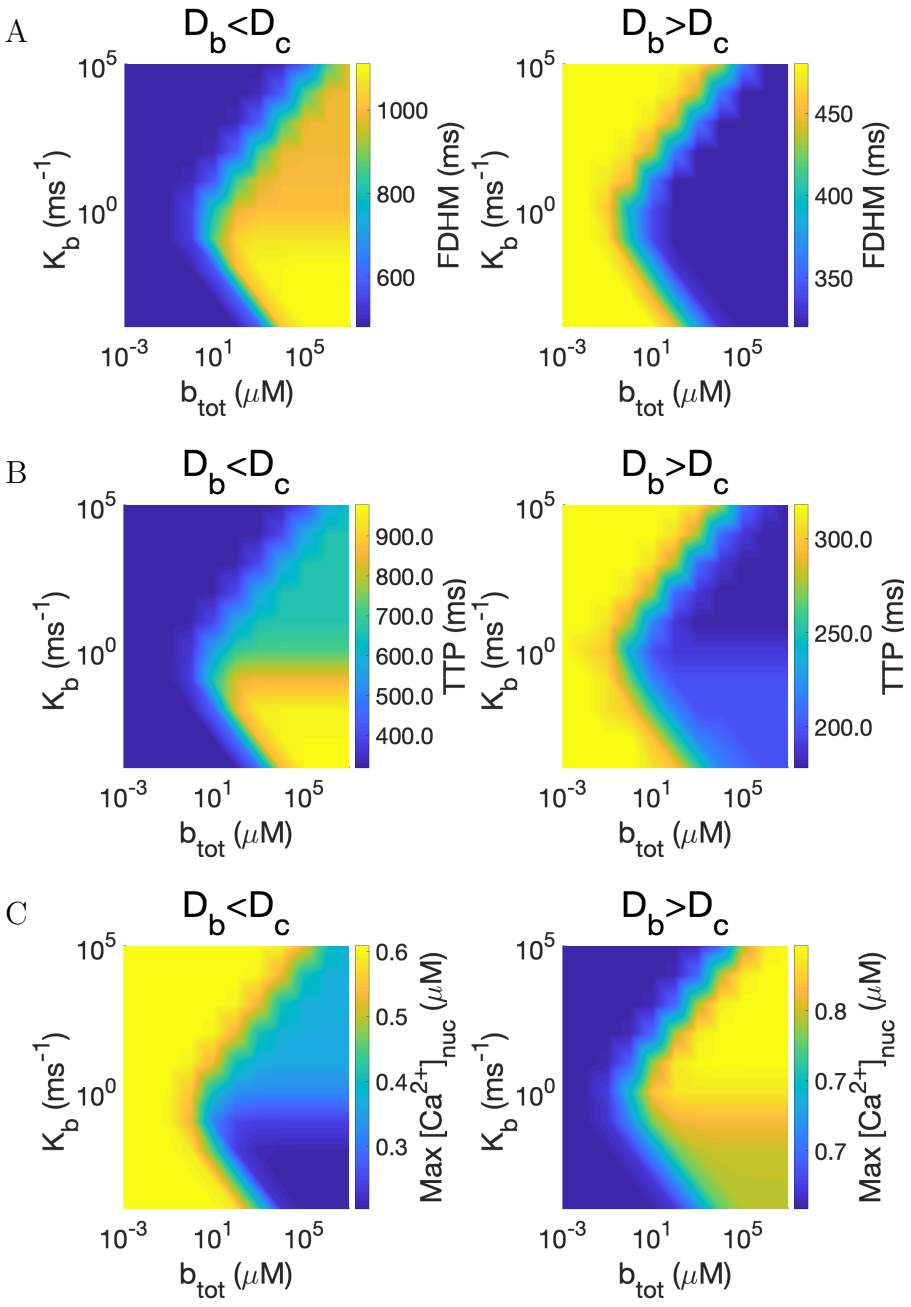

Figure 3.14: The effects of a buffer on Ca^{2+} transport into the nucleus. The effects of buffers with a higher diffusion coefficient than Ca^{2+} are contrasted with those with a lower diffusion coefficient. When the buffer diffusion coefficient and the Ca^{2+} diffusion coefficient are similar, the buffer has far less impact on Ca^{2+} diffusion (See Figures 3.21 to 3.23). There is a clear division between when the buffers have little to no effect on the Ca^{2+} transient (the left half of both plots) and when the buffers are at saturating concentrations (the right half of both plots). The differences visible across the range of saturating concentrations are due to different binding rates (dissociation constants, K_b) leading to different concentrations of Ca^{2+} being bound during saturation.

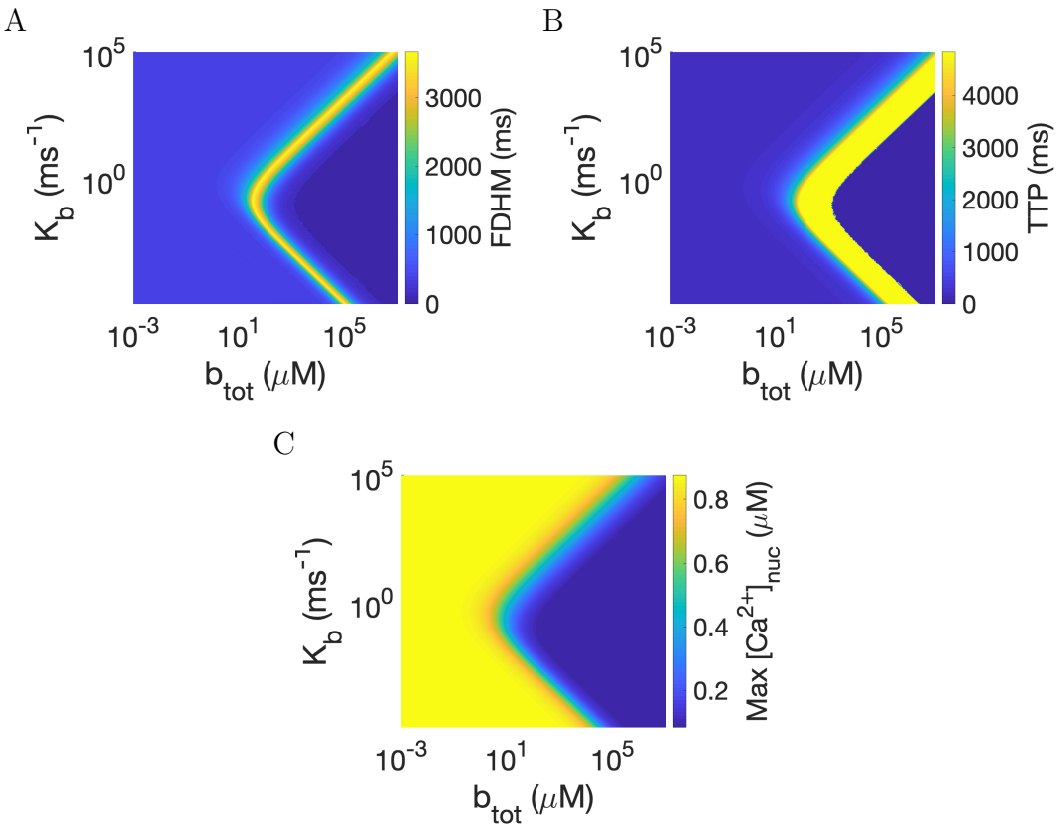

Figure 3.15: Effects of stationary buffers on the nuclear Ca^{2+} transient at the centre of the nucleus. Stationary buffers in the nucleus can greatly increase the FDHM and TTP of the nuclear transient within a narrow concentration whose range is dependent on the buffer binding properties. We show the effect of dissociation constant and concentration of a stationary buffer on nuclear transient (A) FDHM, (B) TTP, and (C) maximum $[Ca^{2+}]$. The highest values of FDHM occur within the range of buffer concentrations for which there is just enough buffer to keep the concentration of Ca^{2+} in the nucleus stable during a Ca^{2+} transient. The highest values of TTP occur when the concentration of buffer is high enough that $[Ca^{2+}]$ in the centre of the nucleus only rises towards the end of our simulations, long after the cytosolic Ca^{2+} transient. Once the buffer concentration is over a certain threshold, the drop in FDHM and TTP is due to the high concentration of buffer binding all available Ca^{2+} ions and preventing any rise in nuclear Ca^{2+} in the centre of the nucleus during the cytosolic Ca^{2+} transient. We know from nuclear Ca^{2+} imaging that both of these situations correspond to an implausible concentration of the buffer as nuclear Ca^{2+} clearly rises with each cytosolic Ca^{2+} transient throughout the nucleus. We see a decline in the amplitude of the Ca^{2+} transient with buffer concentration in (C). In all three plots, the stationary buffer is most efficient in altering the nuclear Ca^{2+} transient when the binding and unbinding rates have similar orders of magnitude ($K_b \approx 1\text{ms}^{-1}$). This simulation was run with $D_c = 0.0174\ \mu\text{m}^2/\text{ms}$.

amplitude as buffers slow down the overall rate of Ca^{2+} diffusion (See Figure 3.14C and Figure 3.23). Stationary buffers decrease the amplitude in the nucleus as they stop the diffusion of Ca^{2+} when bound. At high enough concentrations, a stationary buffer will prevent any $[Ca^{2+}]$ change in the nucleus (See Figure 3.15C).

3.4.6 Cytosolic transients of greater duration result in nuclear transients with both greater duration and greater amplitude

So far we have explored the parameter space relating to the size of the nucleus, NE conductance, and buffers. There is evidence, however, of Ca^{2+} release either in or around the nucleus from IP_3Rs (165, 80). Additionally, perinuclear Ca^{2+} release could explain some of the variance we see in nuclear TTP vs cytosolic TTP, even within the same cell (See Figure 3.3B and D). In Chapter 2 we explored the effect of IP_3R channel activation on the cytosolic transient. Our results indicate that we should see an increase in FDHM and could see a change in amplitude. Modifying these characteristics of the cytosolic transient, by modifying the $[Ca^{2+}]$ at the nuclear boundary ($q(t)$), we find that cytosolic transients with greater peak $[Ca^{2+}]$ result in nuclear transients with a greater peak $[Ca^{2+}]$ but the change does not affect the TTP or FDHM in the nucleus (See Figure 3.17). However, longer cytosolic Ca^{2+} transients, those with greater FDHM, result in transients that are both longer and have greater peak $[Ca^{2+}]$ (See Figures 3.16 and 3.17).

In our simulations, Ca^{2+} diffuses into the nucleus from the cytosol as long as the Ca^{2+} concentration in the cytosol is higher than in the nucleus. When the cytosolic transient is longer, it remains higher than the nuclear transient for longer so more Ca^{2+} is able to diffuse into the nucleus, contributing to a greater nuclear amplitude. Similarly, the delay before the cytosolic Ca^{2+} concentration falls below the nuclear Ca^{2+} concentration contributes to a longer nuclear Ca^{2+} transient.

The extent of the effect of the shape of the cytosolic Ca^{2+} transient on the nuclear Ca^{2+} transient is dependent on D_c. In general, the greater D_c, the more of an effect the shape of the cytosolic transient has on the nuclear transient (See Figure 3.18).

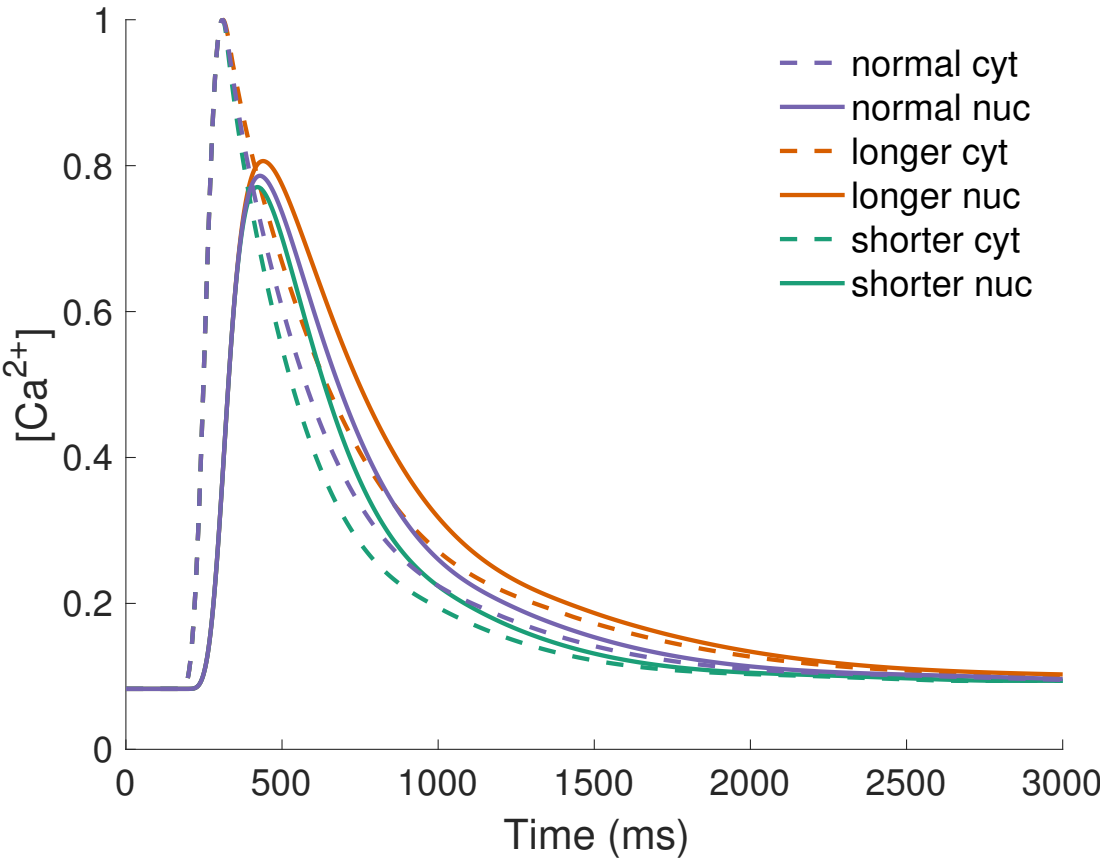

Figure 3.16: Comparison of the effects of varying the duration of cytosolic transients on Ca^{2+} dynamics in the nucleus (no buffers). The FDHM of the cytosolic Ca^{2+} transient affects both the duration and amplitude of the Ca^{2+} transient seen in the nucleus. The cytosolic transients were all approximations of a typical transient measured at the edge of the nucleus. The altered transient lengths were achieved by dilating the transient after Ca^{2+} concentration had peaked to simulate the changes to the Ca^{2+} transient seen in our compartmental model.

3.4.7 Buffering and increased FDHM are required to match experimental FDHM and TTP in the nucleus

Having explored the effects of buffering and alterations to the $[Ca^{2+}]$ at the nuclear boundary separately, we can now investigate the combined effects of these two aspects of Ca^{2+} dynamics. Any Ca^{2+} release from perinuclear IP_3Rs could increase the diastolic $[Ca^{2+}]$, the TTP, the FDHM, and/or the peak $[Ca^{2+}]$ of the Ca^{2+} transient at the boundary of the nucleus. Exploring the effects of these changes on the $[Ca^{2+}]$ within the nucleus, we find that an increase in FDHM brings our nuclear Ca^{2+} simulations closer to what we see in line-scans. Figure

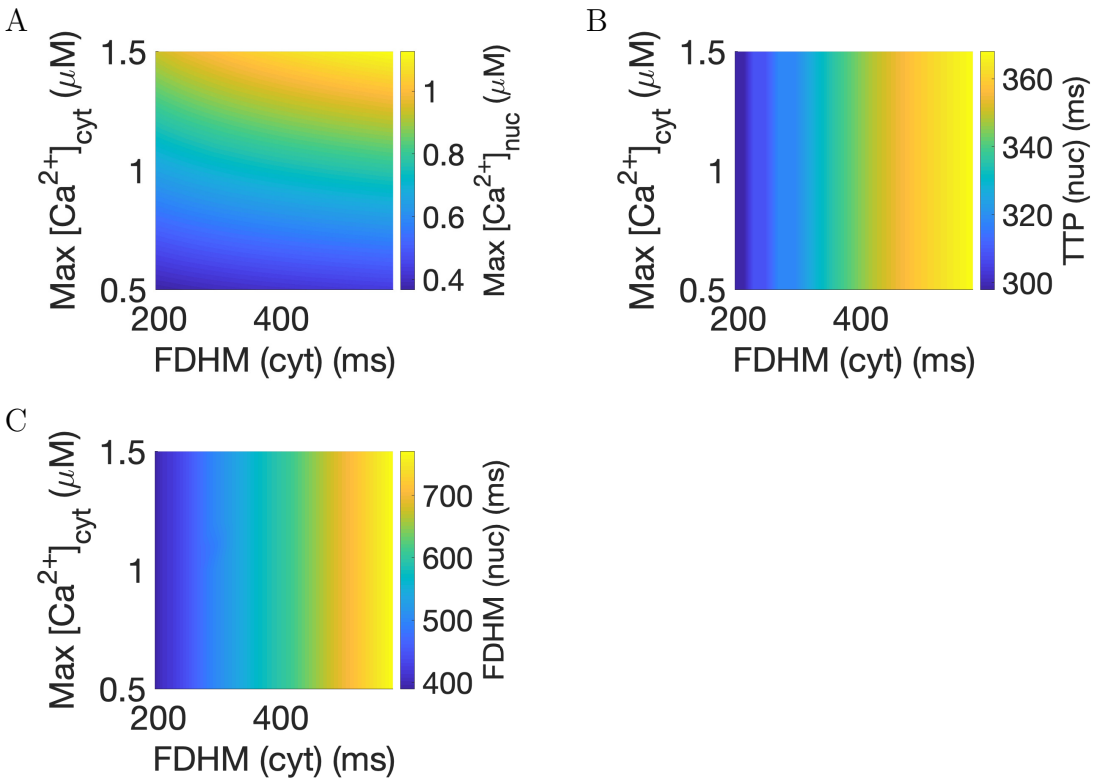

Figure 3.17: These plots illustrate the relationship between the amplitude and FDHM of the cytosolic Ca^{2+} transient and the amplitude (A), TTP (B), and FDHM (C) of the nuclear transient without buffers. The Ca^{2+} diffusion coefficient used in these simulations is 0.0063 μm^2/ms. As in Figure 3.18, the amplitude of the cytosolic Ca^{2+} transient has little effect on the TTP or FDHM of the nuclear transient. It's effect on the amplitude of the nuclear transient is dependent on the Ca^{2+} diffusion coefficient in the nucleus. The FDHM of the cytosolic transient affects the amplitude, TTP, and FDHM of the resulting nuclear Ca^{2+} transient.

3.19 shows the range of TTP and FDHM for solutions with buffering but no change to $q(t)$ estimated from cell data (blue) and the range of TTP and FDHM for the same simulations but where $q(t)$ is altered to have a greater FDHM (pink). Regardless of the combination of buffer parameters, nucleus size, and NE conductance, we cannot match the FDHM and TTP of the nuclear Ca^{2+} transient that we see in line-scan data. However, increasing the FDHM of the incoming cytosolic transient results in a greater FDHM to TTP ratio, bringing our simulations closer to what we see in data. Of the simulations that fall within one standard deviation of the average temporal characteristics of the cell simulated in Figure 3.19, the common feature of the parameter sets that generate these nuclear

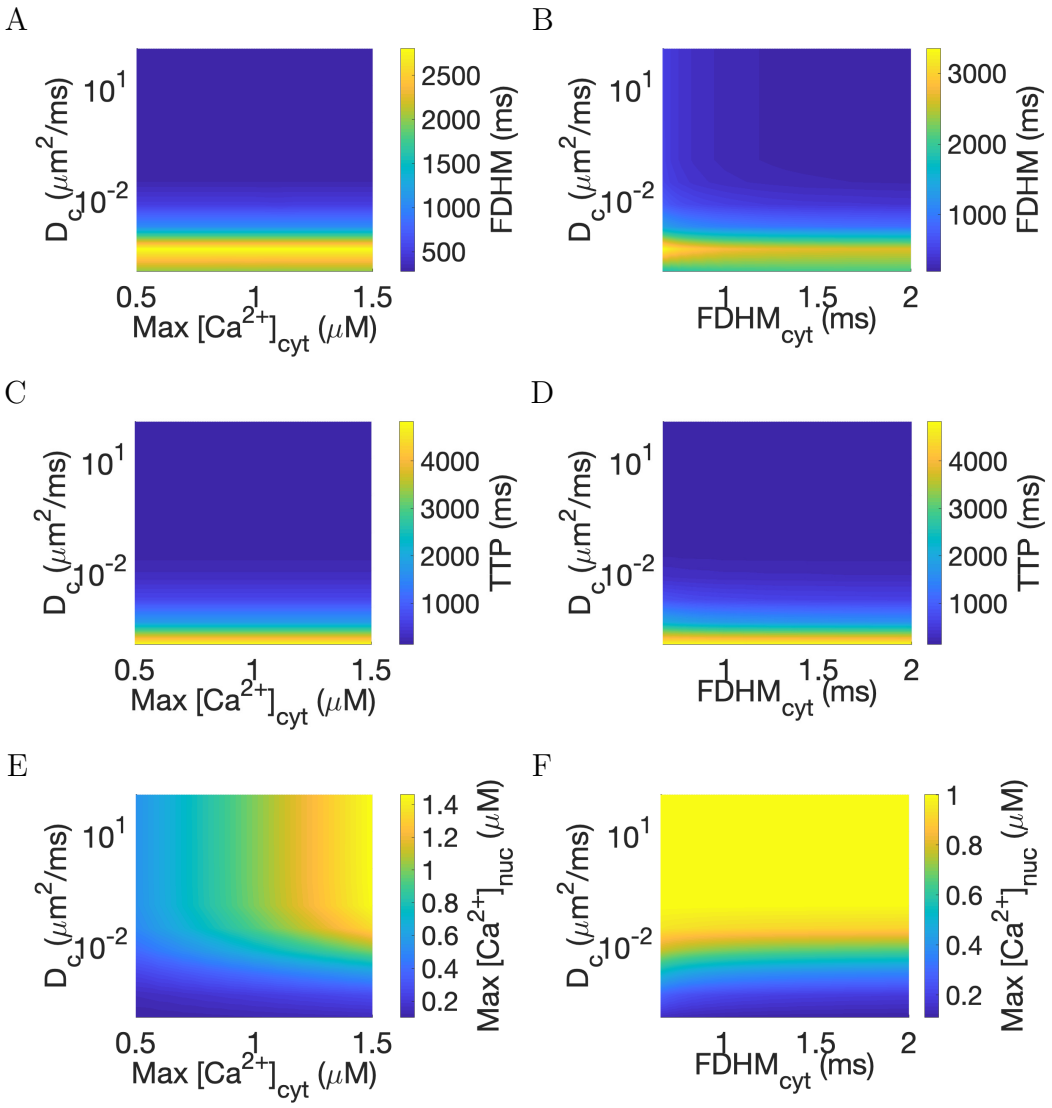

Figure 3.18: These plots illustrate the relationship between (A) the amplitude and (B) the FDHM of the cytosolic Ca^{2+} transient and the shape of the nuclear transient without buffers for different Ca^{2+} diffusion coefficients in the nucleus. The amplitude of the cytosolic Ca^{2+} transient has little effect on the TTP or FDHM of the nuclear transient. It's effect on the amplitude of the nuclear transient is dependent on the Ca^{2+} diffusion coefficient in the nucleus. The FDHM of the cytosolic transient affects the amplitude, TTP, and FDHM of the resulting nuclear Ca^{2+} transient. There is an apparent anomaly in its effect on the FDHM of the nuclear transient at $D_c = 0.0001$ μm^2/ms where the slow Ca^{2+} diffusion coefficient results in such a slow TTP that the FDHM is noticeably decreased.

Ca^{2+} transients is that they all include buffers (however, the parameters of these buffers vary). A simulation of one such parameter set is shown in Figure 3.20. These results suggest that to explain observed nuclear calcium dynamics, calcium release in the vicinity of the nuclear envelope is required.

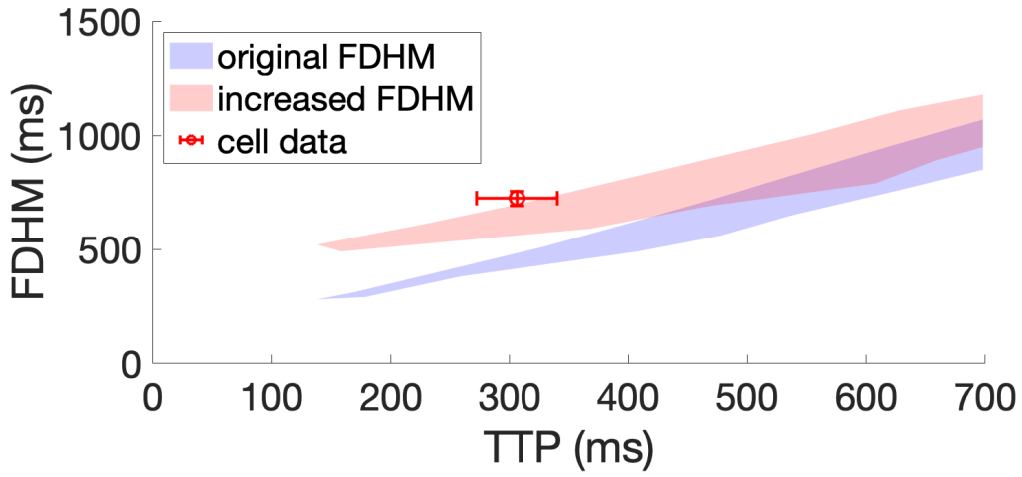

Figure 3.19: Depicted here is the range of temporal characteristics of nuclear Ca^{2+} transient simulations at the centre of the nucleus when modelling buffer induced nonlinear diffusion (blue) and the range for those same parameters when the duration of $q(t)$ after its peak is doubled (pink). The red cross indicates the mean nuclear TTP and FDHM of the cell that $q(t)$ was estimated from. The error bars show the standard deviation from measurements of successive nuclear Ca^{2+} transients in the same cell.

3.5 Discussion

In this chapter we have developed a model of Ca^{2+} dynamics into the nucleus based on buffered diffusion of cytosolic Ca^{2+} into the nucleus. The effects of Ca^{2+} release and obstruction, i.e. through NPC gating, are also simulated through modification of our model's boundary conditions.

We have shown that while the size of the nucleus plays a role in the shape of the nuclear Ca^{2+} transient, and a simple scaling of the Ca^{2+} transient as it passes through the NE can affect its shape, by far the most important factor determining the nuclear Ca^{2+} transient is the nuclear Ca^{2+} diffusion coefficient. The apparent diffusivity is primarily determined by buffering. With the number of buffers that are likely to be present in the nucleus and the complications involved in estimating diffusion in such a small compartment, we cannot determine the

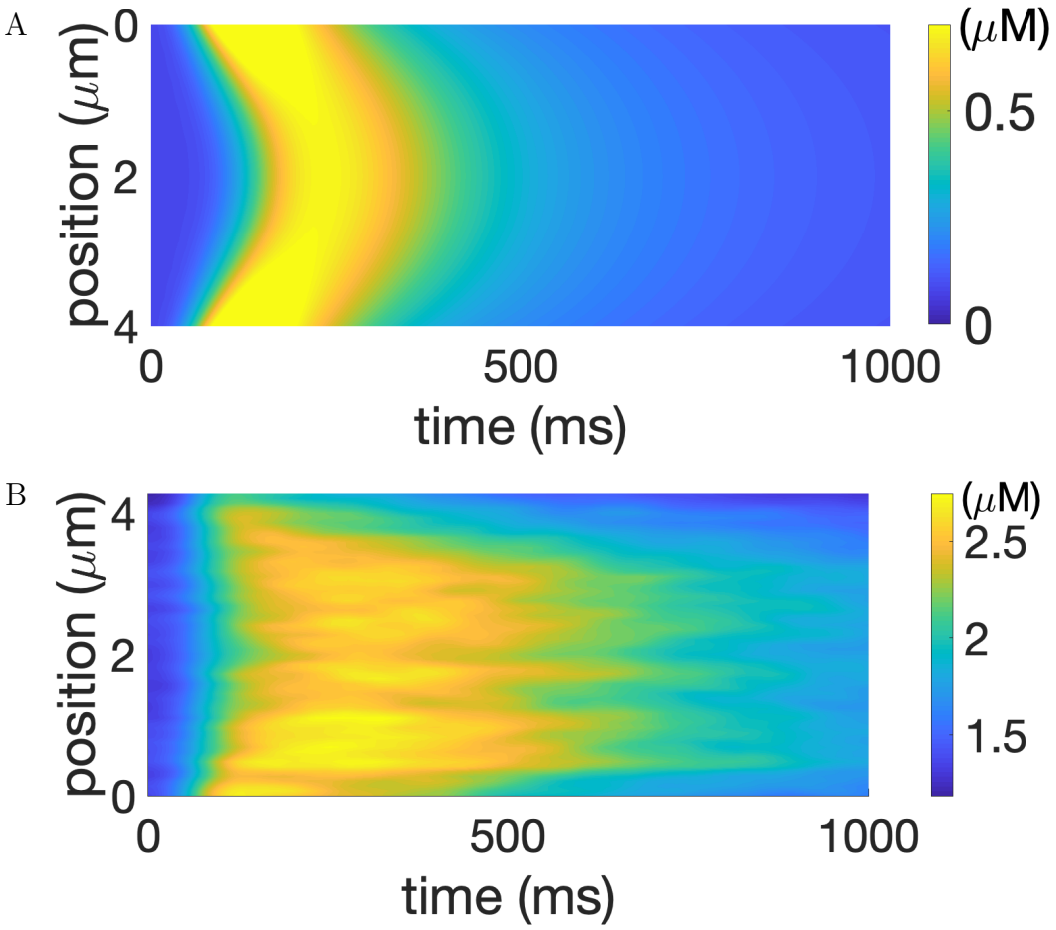

Figure 3.20: (A) Simulation of $[Ca^{2+}]$ diffusion in the nucleus during ECC and (B) line-scan image of $[Ca^{2+}]$ in the nucleus.

exact number and properties of the buffers from just fluorescent line-scan data. We can, however, narrow down the likely properties of the most dominant Ca^{2+} buffers and how they affect the nuclear Ca^{2+} transient.

3.5.1 Likely properties of nuclear calcium buffers based on the FDHM and TTP of the nuclear calcium transient

In simulations of nuclear $[Ca^{2+}]$ based only on Ca^{2+} diffusion, we cannot match both the TTP and the FDHM of measured nuclear Ca^{2+} transients. By matching the TTP, we find that the FDHM is always longer *in vitro* than in our simulations. The modelled buffers that come closest to matching the temporal characteristics of the experimental data are the stationary buffers. The only stationary Ca^{2+}

buffers that we have mentioned so far are the annexins which are generally linked to the NE membrane. However, we cannot draw too many conclusions from this result due to the uncertainty in the number of buffers that contribute to the nonlinear Ca^{2+} diffusion we see.

3.5.2 Increased amplitude and FDHM of cytosolic calcium transients results in increased amplitude of nuclear transients

It has been hypothesised that cytosolic Ca^{2+} signals are transmitted through localisation, or changing amplitude, frequency, diastolic $[Ca^{2+}]$, or duty cycle (7, 49). Nuclear Ca^{2+} signals must be transmitted through similar means. Our simulations indicate that an increase in the average $[Ca^{2+}]$ seen at the edge of the nucleus will result in an increase in nuclear transient amplitude (Figure 3.17). In particular we have shown that an increase in the duration of a cytosolic Ca^{2+} transient will result in an increase in duration and amplitude of the corresponding nuclear Ca^{2+} transient. This is because the increased period that cytosolic $[Ca^{2+}]$ is elevated allows for the net movement of Ca^{2+} into the nucleus to remain positive for a correspondingly increased period. This means that more Ca^{2+} is able to enter the nucleus and results in an overall greater $[Ca^{2+}]$ within the nucleus as well as a greater peak $[Ca^{2+}]$.

3.5.3 The necessary increase in the FDHM of the calcium transient at the nuclear boundary could indicate perinuclear calcium release

To match temporal characteristics of the observed nuclear Ca^{2+} transient in our simulations, we needed to significantly increase the FDHM of the boundary Ca^{2+} transient. This modification to the transient is reminiscent of the modifications we observed when modelling the effect of IP_3R activation on the ECC. This could be evidence of the presence of active IP_3R channels in the perinuclear region. There is evidence of IP_3R channel activity outside of cells undergoing hypertrophic remodelling (80) as well as increased IP_3R density around the nucleus in some myocytes (3, 165). It appears possible that IP_3R channels are modifying the

global ECC signal as it enters the nucleus. However, further investigation is required to confirm this hypothesis.

3.5.4 Calcium transport into the nucleus on buffers

While we have so far explored only the consequences of unbound Ca^{2+} entering the nucleus, given the size of NPCs and the movement of Ca^{2+} buffers, notably calmodulin, Ca^{2+} must also be diffusing in as part of a buffer complex (164). This means that any buffers we do not model are an unexplored source of nuclear Ca^{2+}. This phenomenon has several implications. Ca^{2+} being carried in by buffers could explain the instances of nuclear Ca^{2+} concentrations exceeding cytosolic peak amplitudes (80) – carrier buffers could potentially release more Ca^{2+} in the different environment of the nucleus. Additionally, release of Ca^{2+} from carrier buffers could be crucial to determining the TTP and FDHM of the nuclear transient. While some of this buffering effect is accounted for in our model, the full effect will require an approximation of all of the most relevant buffers. The extent of the influence of carrier buffers on nuclear Ca^{2+} dynamics remains to be seen.

3.5.5 Alternate models for NPC gating of calcium

We have used a relatively simple model of the effect of Ca^{2+} diffusion across the NE in which we investigated the implications of the NPCs restricting Ca^{2+} diffusion by reducing the amount of Ca^{2+} that entered the nucleus by a constant fraction. Genka et al. (42) observed bi-modal Ca^{2+} diffusion across the NE and attributed this to Ca^{2+} gated NPCs. In this study, we have focussed more on the effects of buffers and perinuclear Ca^{2+} release. In future work, exploring the effects of NPC gating being determined by a Hill function of the initial Ca^{2+} transient recorded at the boundary of the nucleus or as a Hill function controlling the flux across the NE would be worth considering.

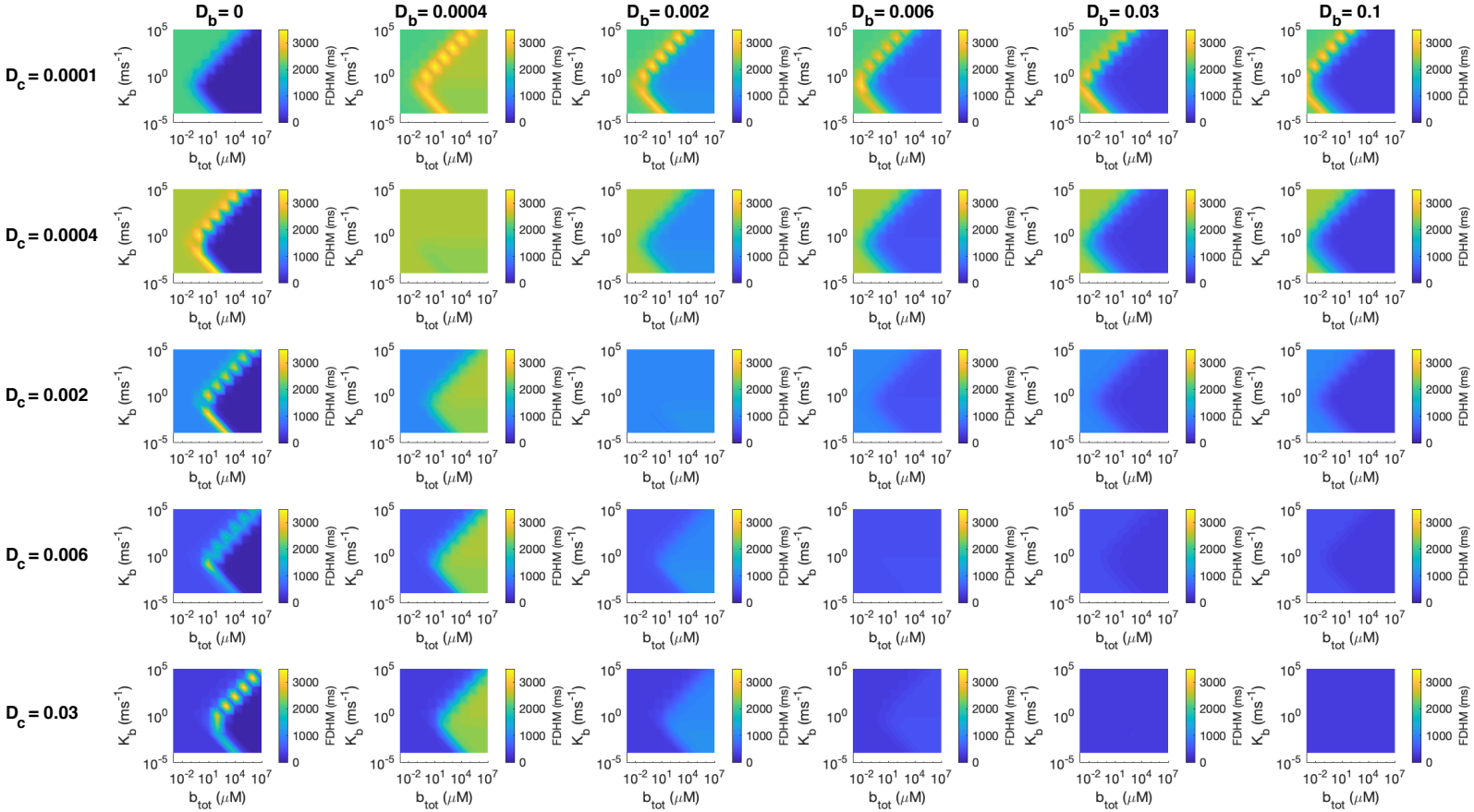

Figure 3.21: Effect of the Ca^{2+} and buffer diffusion coefficients on the FDHM of the Ca^{2+} transient in the nucleus. Diffusion coefficients are given in units of $\mu m^2/ms$.

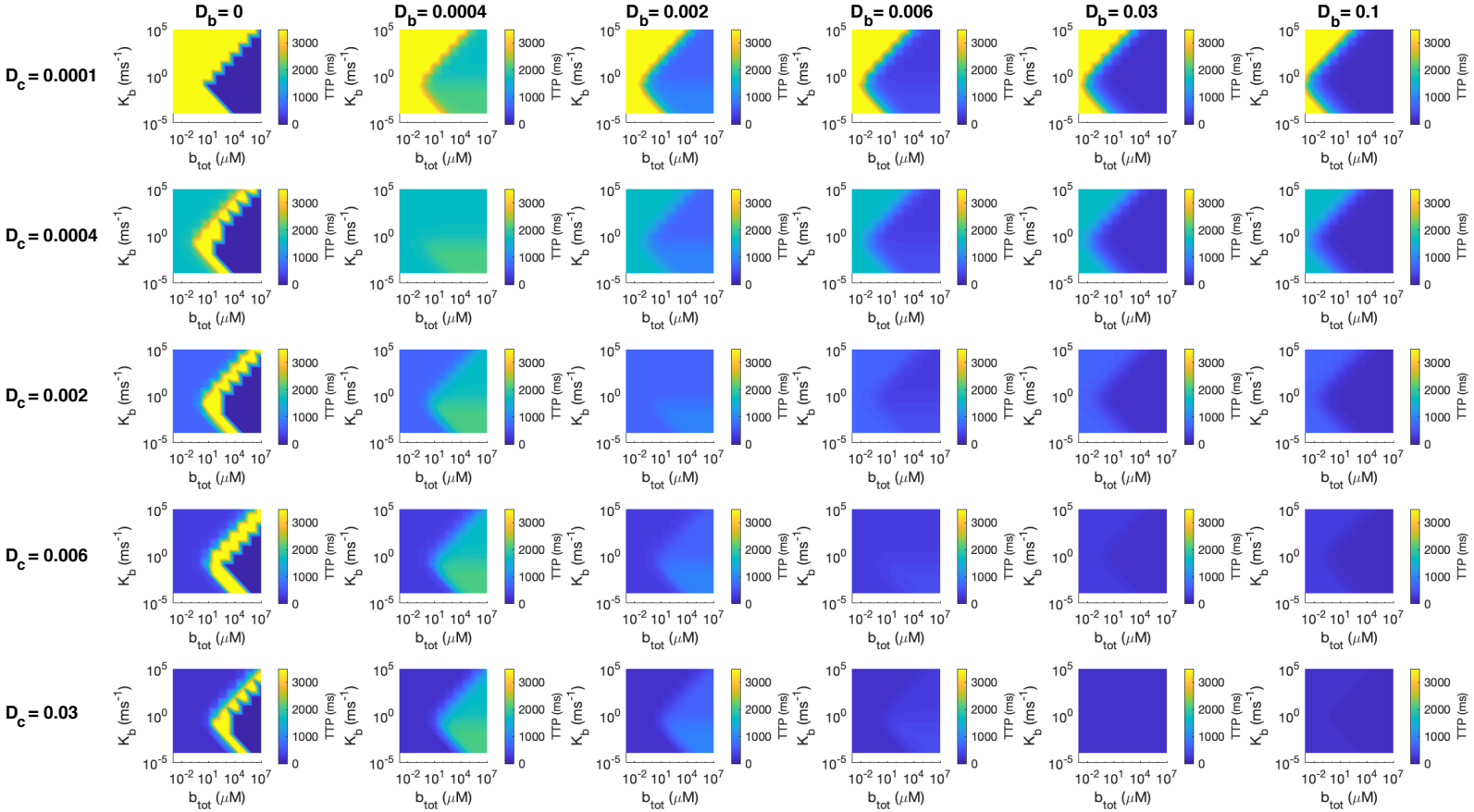

Figure 3.22: Effect of the Ca^{2+} and buffer diffusion coefficients on the TTP of the Ca^{2+} transient in the nucleus. Diffusion coefficients are given in units of $\mu m^2/ms$.

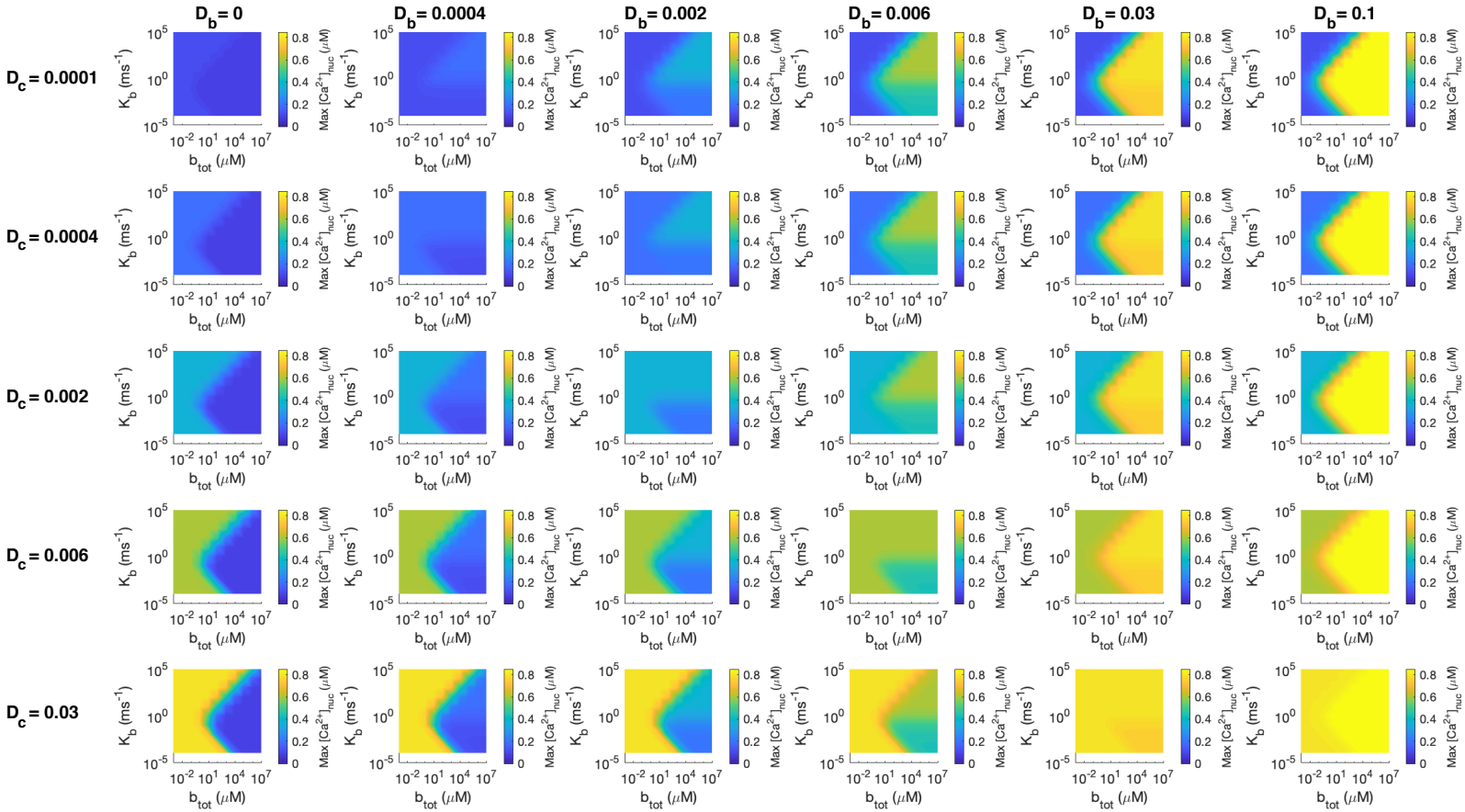

Figure 3.23: Effect of the Ca^{2+} and buffer diffusion coefficients on the amplitude of the Ca^{2+} transient in the nucleus. Diffusion coefficients are given in units of $\mu m^2/ms$.

Chapter 4

An analytical analysis of calcium diffusion into a cylindrical nucleus

In the previous chapter, we simplified Ca^{2+} dynamics in the nucleus into a 1D numerical diffusion model and examined the effects of buffers on the nuclear Ca^{2+} transient. In this chapter, we take a closer look at the geometry of the nucleus and the effect of Ca^{2+} diffusion in the longitudinal direction on the nuclear Ca^{2+} transient. We analytically solve the diffusion model in both 1D and 3D. We use the analytical solution to verify our numerical solution and assumptions. We also investigate the effect of Ca^{2+} diffusion through the ends of the nucleus on the concentration within the nucleus. The 3D model allows us to better describe the spatial variation throughout the nucleus. Additionally, it gives us a better understanding of the effect the angle of a line-scan has on the $[Ca^{2+}]$ observed in the nucleus when viewing a line-scan image. We show that in the average nucleus, assuming homogeneous diffusion, a 1D simulation is sufficient to model $[Ca^{2+}]$ in the centre of the nucleus.

4.1 Introduction

Cardiac nuclei, pictured in Figures 3.1 and 4.1, are varied in size and fluid in shape (see Figure 4.2). They can broadly be described as ellipsoids, capped at each end by 'spindles' of mitochondria (36). This relatively regular shape is occasionally broken by transient invaginations of the NE into the nucleus (47, 12, 90). In the

previous chapter we assumed that these mitochondrial spindles would prevent Ca^{2+} diffusion into the nucleus to the extent that we should only need to model diffusion in from the perpendicular direction to the long axis. Ca^{2+} line-scan images of the nucleus during a global Ca^{2+} transient appear to support this. However, as we discussed in Chapter 2, even subtle changes to intracellular Ca^{2+} dynamics can affect downstream signalling outcomes. Given the noise inherent in the system, the line-scan data is not sufficient to conclude that diffusion through the ends of the nucleus is insignificant.

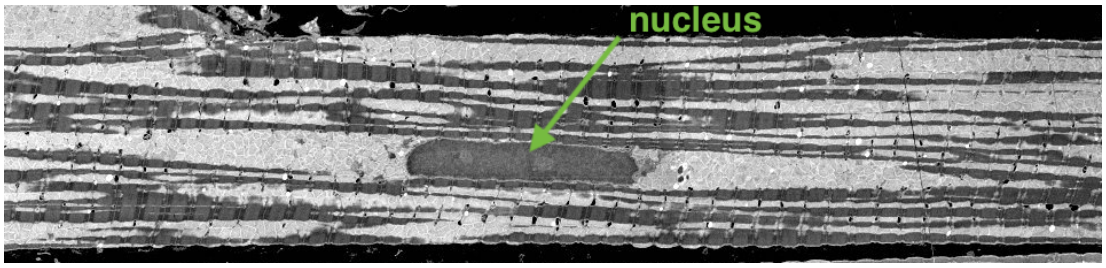

Figure 4.1: Image of a cardiomyocyte captured using serial-block-face scanning electron microscopy by Hussain et al. (59). The nucleus is visible as a dark, cylindrical object in the centre of the image. The mitochondria are shown as pale grey streaks in the cell while the myofibrils are darker, striped lines.

Additionally, the critical aspects of nuclear $[Ca^{2+}]$ dynamics that affect the hypertrophic pathway are still unclear. Consequently, in this chapter, we take a closer look at the spatial variation in $[Ca^{2+}]$ within the nucleus. Specifically, how diffusion along the long axis of the nucleus, here defined as the z-axis, affects $[Ca^{2+}]$ dynamics throughout the nucleus. We again model the cardiac nucleus as a cylinder, as it appears in scanning electron microscopy images (Figure 4.1), and analytically solve our model to find the $[Ca^{2+}]$ in the nucleus as a function of time and the cytosolic Ca^{2+} transient. The analytical solution has the benefit of allowing us to easily simplify back to the 1D model and determine the Ca^{2+} concentration over several beats with minimal computation.

The size variation between nuclei must impact on the influence of cytosolic $[Ca^{2+}]$ and any other external factors (i.e. perinuclear Ca^{2+} release) on nuclear Ca^{2+} dynamics. Therefore, we investigate the effect of nucleus size on the nuclear transient. We also investigate the effect of different measurement methods on measured nuclear Ca^{2+} transients, which may be significant in the interpretation of fluorescent Ca^{2+} measurements.

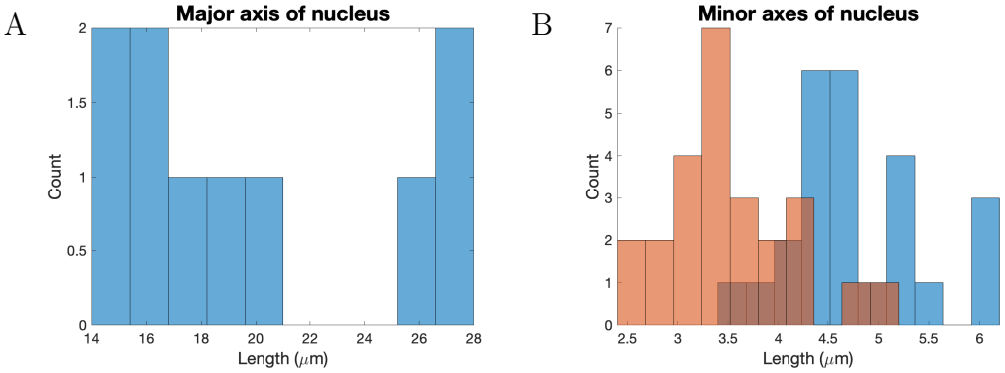

Figure 4.2: Distribution of nucleus sizes measured along each axis. The average length of the major axis in these nuclei was 19.08 μm with standard deviation 5.06 μm. The minor axes were measured as the largest diameter in each nucleus and the diameter of the perpendicular minor axis. These values were measured to be 4.76 ± 0.68 μm and 3.49 ± 0.64 μm respectively. (4)

4.2 Analytical solution of diffusion into a 3D cylinder

To analytically solve the Ca^{2+} diffusion equation, we approximate the geometry of the nucleus as a cylinder of length, l, and radius, a, as in Figure 4.3. The diffusion equation in cylindrical coordinates is

$$\frac{\partial c}{\partial t} = D\left(\frac{\partial^2 c}{\partial r^2} + \frac{1}{r}\frac{\partial c}{\partial r} + \frac{1}{r^2}\frac{\partial^2 c}{\partial \theta^2} + \frac{\partial^2 c}{\partial z^2}\right) \tag{4.1}$$

In this analysis we will fold all nuclear buffers into the effective diffusion coefficient, D, i.e. assume rapid and saturating or low affinity Ca^{2+} buffering. If we assume Ca^{2+} diffuses into the nucleus from all directions, the boundary conditions for Equation 4.1 are:

$$c(r, \theta, 0, t) = c(r, \theta, l, t) = q(t) \tag{4.2a}$$
$$c(r, \theta, z, 0) = c_0 \tag{4.2b}$$
$$c(a, \theta, z, t) = q(t) \tag{4.2c}$$
$$c(r, \theta, z, t) = c(r, \theta + 2\pi, z, t) \tag{4.2d}$$

where c_0 is the initial concentration in the nucleus and $q(t)$ is the Ca^{2+} concentration at the boundary of the nucleus, representative of either the effects of a global Ca^{2+} transient as seen from the nucleus, or the Ca^{2+} being released at

the nuclear envelope. Note that this is a spatially independent, inhomogeneous boundary condition. In order to solve this equation, we first need to solve the same problem but with a homogeneous boundary condition.

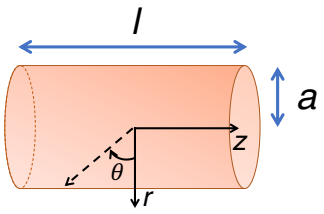

Figure 4.3: We approximate the nucleus as a cylinder of radius, a, and length, l. Our coordinates are r, θ, and z.

4.2.1 Inhomogeneous boundary condition

To convert between a system with an inhomogeneous boundary condition and one with a homogeneous boundary condition, we subtract a non-differential function from the whole system that will give $c = 0$ on the boundaries. Let $v(r, \theta, z, t) = c(r, \theta, z, t) - q(t)$

$$\frac{\partial v}{\partial t} = \frac{\partial c}{\partial t} - \frac{\partial q}{\partial t} \tag{4.3a}$$

$$\frac{\partial v}{\partial r} = \frac{\partial c}{\partial r} - \frac{\partial q}{\partial r} = \frac{\partial c}{\partial r} \tag{4.3b}$$

$$\frac{\partial v}{\partial \theta} = \frac{\partial c}{\partial \theta} - \frac{\partial q}{\partial \theta} = \frac{\partial c}{\partial \theta} \tag{4.3c}$$

$$\frac{\partial^2 v}{\partial z^2} = \frac{\partial^2 c}{\partial z^2} - \frac{\partial^2 q}{\partial z^2} = \frac{\partial^2 c}{\partial z^2} \tag{4.3d}$$

Then

$$\frac{\partial v}{\partial t} = D\left(\frac{\partial^2 v}{\partial r^2} + \frac{1}{r}\frac{\partial v}{\partial r} + \frac{1}{r^2}\frac{\partial^2 v}{\partial \theta^2} + \frac{\partial^2 v}{\partial z^2}\right) - \frac{\partial q}{\partial t} \tag{4.4}$$

with

$$v(r,\theta,0,t) = v(r,\theta,l,t) = 0 \tag{4.5a}$$
$$v(r,\theta,z,0) = c_0 - q_0 = v_0 \tag{4.5b}$$
$$v(a,\theta,z,t) = 0 \tag{4.5c}$$
$$v(r,\theta,z,t) = v(r,\theta+2\pi,z,t) \tag{4.5d}$$

Giving a system with homogeneous boundary conditions.

4.2.2 Solving for $q(t) = 0$ using separation of variables

Upon examination, we find that $v(r,\theta,z,t)$ is separable. Let

$$v(r,\theta,z,t) = R(r)\Theta(\theta)Z(z)T(t) \tag{4.6}$$

Then substituting this into Equation 4.4:

$$R\Theta ZT_t = D\left(R_{rr}\Theta ZT + \frac{1}{r}R_r\Theta ZT + \frac{1}{r^2}R\Theta_{\theta\theta}ZT + R\Theta Z_{zz}T\right) \tag{4.7}$$

where the subscripts indicate the differential. Dividing through by $DR(r)\Theta(\theta)Z(z)T(t)$, we have

$$\frac{T_t}{DT} = \frac{R_{rr}}{R} + \frac{1}{r}\frac{R_r}{R} + \frac{1}{r^2}\frac{\Theta_{\theta\theta}}{\Theta} + \frac{Z_{zz}}{Z} \tag{4.8}$$

The left side of Equation 4.8 varies with t while the rights side varies with r, θ, and z. This can only be true if both sides are equal to some constant, $-\gamma^2$. We choose a negative constant here because we expect the solution to decay over time, i.e. $T_t < 0$.

$$\frac{T_t}{DT} = \frac{R_{rr}}{R} + \frac{1}{r}\frac{R_r}{R} + \frac{1}{r^2}\frac{\Theta_{\theta\theta}}{\Theta} + \frac{Z_{zz}}{Z} = -\gamma^2 \tag{4.9}$$

This yields a differential equation for $T(t)$. Continuing in this vein, we can find differential equations for each of R, Θ, and Z.

$$-\frac{Z_{zz}}{Z} = \frac{R_{rr}}{R} + \frac{1}{r}\frac{R_r}{R} + \frac{1}{r^2}\frac{\Theta_{\theta\theta}}{\Theta} + \gamma^2 = \mu^2 \tag{4.10}$$

$$-\frac{\Theta_{\theta\theta}}{\Theta} = \frac{R_{rr}}{R}r^2 + \frac{R_r}{R}r + \left(\gamma^2 - \mu^2\right)r^2 = \phi^2 \tag{4.11}$$

where μ and ϕ are constants. As in Equation 4.9, we rely on our knowledge of the physical properties of the system to determine the sign of these constants. The boundary conditions translate to:

$$Z(0) = Z(l) = 0 \tag{4.12a}$$

$$R(a) = 0 \tag{4.12b}$$

$$\Theta(\theta) = \Theta(\theta + 2\pi) \tag{4.12c}$$

These can now be solved to find v.

(i) Solve for Z

$$\frac{Z_{zz}}{Z} = -\mu^2 \tag{4.13}$$

Define constants $f, g \in \mathbb{R}$. Then

$$Z(z) = f\sin(\mu z) + g\cos(\mu z) \tag{4.14}$$

Substituting in $z = 0$ we can remove the cos term:

$$Z(0) = f0 + g\cos(\mu z) = 0 \tag{4.15}$$

$$\implies g = 0 \tag{4.16}$$

Substituting in $z = l$ allows us to find solutions for μ.

$$Z(l) = f\sin(\mu l) = 0 \tag{4.17}$$

$$\implies \mu_j = \frac{j\pi}{l} \quad j \in \mathbb{N} \tag{4.18}$$

We now have eigenfunction solutions

$$Z_j(z) = \sin\left(\frac{j\pi z}{l}\right) \tag{4.19}$$

where $j \in \mathbb{N}$. Note that we have deliberately chosen the constant, $-\mu^2$, such that $\frac{Z_{zz}}{Z}$ is negative. With our constraints on Z, Equation 4.12a, we find that assuming this term is nonnegative leads to the trivial solution for Z, i.e. $Z(z) = 0$.

(ii) Solve for Θ

$$\frac{\Theta_{\theta\theta}}{\Theta} = -\phi^2 \tag{4.20}$$

As above, define constants $a, b \in \mathbb{R}$. Then

$$\Theta(\theta) = a\sin(\phi\theta) + b\cos(\phi\theta) \tag{4.21}$$

Using the rotational symmetry of the nucleus, we have:

$$\Theta(\theta) = \Theta(\theta + 2\pi) \tag{4.22}$$

$$a\sin(\phi\theta) + b\cos(\phi\theta) = a\sin(\phi(\theta + 2\pi)) + b\cos(\phi(\theta + 2\pi)) \tag{4.23}$$

$$\implies \phi = k \text{ where } k \in \mathbb{N} \cup \{0\} \tag{4.24}$$

We now have eigenfunction solutions

$$\Theta_k(\theta) = a_k\sin(k\theta) + b_k\cos(k\theta) \tag{4.25}$$

where $k \in \mathbb{N} \cup \{0\}$ and $a_k, b_k \in \mathbb{R}$. Note again that we have deliberately chosen the constant, $-\phi^2$, such that $\frac{\Theta_{\theta\theta}}{\Theta}$ is negative. Had we chosen a positive constant, we would have found an expression for Θ of the form

$$\Theta(\theta) = ae^{\phi\theta} + be^{-\phi\theta} \tag{4.26}$$

This is not periodic and would not have been able to satisfy rotational symmetry. Alternatively, choosing $-\phi^2 = 0$ results in solutions of Θ of a linear form. These would satisfy the periodic boundary condition only if $\Theta = b_0$, a constant.

(iii) Solve for R

$$\frac{R_{rr}}{R}r^2 + \frac{R_r}{R}r + \lambda^2 r^2 = \phi^2 \tag{4.27}$$

Where $\lambda^2 = \gamma^2 - \mu^2$. Note that, from Equation 4.24, $\phi = k$, $k = 0, 1, 2, ...$ Rearranging, we have

$$R_{rr}r^2 + R_r r + \left(\lambda^2 r^2 - k^2\right) R = 0 \tag{4.28}$$

If $\lambda^2 > 0$, $k \in \mathbb{N} \cup \{0\}$ this is the Bessel equation. Then for each $k \in \mathbb{N} \cup \{0\}$ we have

$$R_k(r) = g_k J_k(\lambda r) + h_k Y_k(\lambda r) \tag{4.29}$$

where $J_k(r)$ and $Y_k(r)$ are Bessel functions of the first and second kinds and $g_k, h_k \in \mathbb{R}$.

Since $R(0)$ must be finite, and $|Y_k(r)| \to \infty$ as $r \to 0$, we must have $h_k = 0 \; \forall \; k$. Additionally, λ must be chosen such that $R(a) = 0 = g_k J_k(\lambda a)$ to satisfy our other boundary condition on R. Define $\nu_m^{(k)}$ as the mth root of $J_k(\nu) = 0$. Thus the eigenfunction solutions are

$$R_{km}(r) = J_k(\lambda_{km} r) \tag{4.30}$$

where $\lambda_{km} = \frac{\nu_m^{(k)}}{a}$ $m \in \mathbb{N}, k \in \mathbb{N} \cup \{0\}$

Note that when $\lambda^2 < 0$, Equation 4.28 is the modified Bessel equation which admits a complex solution. Further note that when $\lambda^2 = 0$, Equation 4.28 is a second order Cauchy-Euler equation with solution.

$$R(r) = c_1 r^i k + c_2 r^{-ik} \tag{4.31}$$

where $c_a, c_2 \in \mathbb{R}$ and $i^2 = -1$. Taking into account the boundary conditions, this means the solution must be either complex or constant at zero. Hence, we expect $\lambda^2 > 0$ in this system.

(iv) Solve for T

$$\frac{T_t}{DT} = -\gamma^2 \tag{4.32}$$

We have $\gamma^2 = \lambda^2 + \mu^2$. $\gamma^2 > 0$ as both λ^2 and μ^2 are positive. Then the eigenfunction solution is

$$T_{jkm}(t) = e^{-D\gamma_{jkm}^2 t}, \text{ where } \gamma_{jkm} = \left(\frac{\nu_m^{(k)}}{a}\right)^2 + \left(\frac{j\pi}{l}\right)^2 \tag{4.33}$$

(v) General solution

Using the Principle of Superposition, each of R, Θ, Z and T are given by linear combinations of their eigenfunctions (Equations 4.30, 4.25, 4.19, and 4.33). The general solution is

$$v(r,\theta,z,t) = \sum_{j=1}^{\infty}\sum_{k=0}^{\infty}\sum_{m=1}^{\infty} R)km(r)\Theta k(\theta)Z_j(z)T_{jkm}(t) \tag{4.34}$$

$$\begin{aligned} v(r,\theta,z,t) = \sum_{j=1}^{\infty}\sum_{k=0}^{\infty}\sum_{m=1}^{\infty} & g_{km}J_k(\lambda_{km}r)\left(a_k\sin(k\theta) + b_k\cos(k\theta)\right) \\ & \times f_j \sin\left(\frac{j\pi z}{l}\right) h_{kmj} e^{-D\gamma_{jkm}^2 t} \end{aligned} \tag{4.35}$$

The constants can be combined to give

$$\begin{aligned} v(r,\theta,z,t) = \sum_{j=1}^{\infty}\sum_{k=0}^{\infty}\sum_{m=1}^{\infty} & J_k(\lambda_{km}r)\sin\left(\frac{j\pi z}{l}\right) e^{-D\gamma_{jkm}^2 t} \\ & \times \left(A_{jkm}\sin(k\theta) + B_{jkm}\cos(k\theta)\right) \\ & \text{where } A_{jkm}, B_{jkm} \in \mathbb{R} \;\forall\; j,k,m \end{aligned} \tag{4.36}$$

For ease of notation, we will redefine the eigenfunctions of Θ to include these constants and denote them $\Theta_{jkm} = A_{jkm}\sin(k\theta) + B_{jkm}\cos(k\theta)$.From Equation 4.36, and remembering that we have assumed the concentration to be constant across

our entire domain at $t = 0$, we have

$$v(r, \theta, z, 0) = v_0 = R(r)\Theta(\theta)Z(z) \tag{4.37}$$

$$v_0 = \sum_{j=1}^{\infty}\sum_{k=0}^{\infty}\sum_{m=1}^{\infty} J_k(\lambda_{km} r)\sin\left(\frac{j\pi z}{l}\right)\left(A_{jkm}\sin(k\theta) + B_{jkm}\cos(k\theta)\right) \tag{4.38}$$

To determine the values of each constant, we can take advantage of the orthogonality of the eigenfunctions. Multiplying both sides by $\sin(k'\theta)$ and integrating over θ yields:

$$\int_0^{2\pi} \sin(k'\theta) v_0 d\theta = \sum_{j=1}^{\infty}\sum_{k=0}^{\infty}\sum_{m=1}^{\infty} J_k(\lambda_{km} r)\sin\left(\frac{j\pi z}{l}\right) \times \int_0^{2\pi} \sin(k'\theta)\left(A_{jkm}\sin(k\theta) + B_{jkm}\cos(k\theta)\right) d\theta \tag{4.39}$$

$$0 = \sum_{j=1}^{\infty}\sum_{m=1}^{\infty} J_{k'}(\lambda_{k'm} r)\sin\left(\frac{j\pi z}{l}\right) A_{jk'm} \int_0^{2\pi} \sin^2(k'\theta) d\theta \tag{4.40}$$

$$\implies \sum_{j=1}^{\infty}\sum_{m=1}^{\infty} J_{k'}(\lambda_{k'm} r)\sin\left(\frac{j\pi z}{l}\right) A_{jk'm} = 0 \ \forall k' \in \mathbb{N} \cup \{0\} \tag{4.41}$$

Doing the same with $\cos(k'\theta)$ we have:

$$\int_0^{2\pi} \cos(k'\theta) v_0 d\theta = \sum_{j=1}^{\infty}\sum_{k=0}^{\infty}\sum_{m=1}^{\infty} J_k(\lambda_{km} r)\sin\left(\frac{j\pi z}{l}\right) \times \int_0^{2\pi} \cos(k'\theta)\left(\left(A_{jkm}\sin(k\theta) + B_{jkm}\cos(k\theta)\right)\right) d\theta \tag{4.42}$$

$$\forall k' \in \mathbb{N} \ \ 0 = \sum_{j=1}^{\infty}\sum_{m=1}^{\infty} J_{k'}(\lambda_{k'm} r)\sin\left(\frac{j\pi z}{l}\right) B_{jk'm} \int_0^{2\pi} \cos^2(k'\theta) d\theta \tag{4.43}$$

$$\implies \sum_{j=1}^{\infty}\sum_{m=1}^{\infty} J_{k'}(\lambda_{k'm} r)\sin\left(\frac{j\pi z}{l}\right) B_{jk'm} = 0 \ \forall k' \in \mathbb{N} \tag{4.44}$$

when $k = 0$:

$$2\pi v_0 = \sum_{j=1}^{\infty}\sum_{m=1}^{\infty} B_{j0m} J_0(\lambda_{0m} r) \sin\left(\frac{j\pi z}{l}\right) 2\pi \tag{4.45}$$

$$v_0 = \sum_{j=1}^{\infty}\sum_{m=1}^{\infty} B_{j0m} J_0(\lambda_{0m} r) \sin\left(\frac{j\pi z}{l}\right) \tag{4.46}$$

Combining Equation 4.36 with Equations 4.41, 4.44, and 4.46, we can simplify $v(r, \theta, z, t)$.

$$\begin{aligned} v(r,\theta,z,t) = &\sum_{j=1}^{\infty}\sum_{k=0}^{\infty}\sum_{m=1}^{\infty} J_k(\lambda_{km} r) \sin\left(\frac{j\pi z}{l}\right) e^{-D\gamma_{jkm}^2 t} \\ &\times \left(A_{jkm}\sin(k\theta) + B_{jkm}\cos(k\theta)\right) \end{aligned} \tag{4.47}$$

$$\begin{aligned} v(r,\theta,z,t) = \sum_{k=0}^{\infty} e^{-D\gamma_{jkm}^2 t} \Bigg(&\left(\sum_{j=1}^{\infty}\sum_{m=1}^{\infty} J_k(\lambda_{km} r) \sin\left(\frac{j\pi z}{l}\right) A_{jkm}\right) \sin(k\theta) \\ &+ \left(\sum_{j=1}^{\infty}\sum_{m=1}^{\infty} J_k(\lambda_{km} r) \sin\left(\frac{j\pi z}{l}\right) B_{jkm}\right) \cos(k\theta)\Bigg) \end{aligned} \tag{4.48}$$

$$v(r,\theta,z,t) = \sum_{j=1}^{\infty}\sum_{m=1}^{\infty} B_{j0m} J_0(\lambda_{0m} r) \sin\left(\frac{j\pi z}{l}\right) e^{-D\gamma_{j0m}^2 t} \tag{4.49}$$

We can do the same in the z dimension, multiplying both sides of Equation 4.46 by $\sin\left(\frac{j'\pi z}{l}\right)$ and integrating over z.

$$2\int_0^l \sin\left(\frac{j'\pi z}{l}\right) v_0 dz = \sum_{j=1}^{\infty}\sum_{m=1}^{\infty} \int_0^l B_{j0m} J_0(\lambda_{0m} r) \sin\left(\frac{j\pi z}{l}\right) \sin\left(\frac{j'\pi z}{l}\right) dz \tag{4.50}$$

$$2v_0 \frac{l}{j'\pi}(1 - cos\,(j'\pi)) = \sum_{m=1}^{\infty} B_{j'0m} J_0(\lambda_{0m} r) \frac{l}{2} \tag{4.51}$$

$$v_0 = \sum_{m=1}^{\infty} J_0(\lambda_{0m} r) \frac{B_{j'0m} j'\pi}{4(1 - (-1)^{j'})} \; j \in \mathbb{N} \tag{4.52}$$

In the r dimension, we multiply Equation 4.52 by $r\lambda_{0m'}^2 J_0(\lambda_{0m'}r)$ and integrate over r.

$$\int_0^a r\lambda_{0m'}^2 J_0(\lambda_{0m'}r)v_0 dr$$

$$= \sum_{m=1}^{\infty} \int_0^a r\lambda_{0m'}^2 J_0(\lambda_{0m'}r)J_0(\lambda_{0m}r)\frac{B_{j'0m}j'\pi}{4(1-(-1)^{j'})}dr \tag{4.53}$$

$$v_0 \int_0^{\lambda_{0m'}a} \lambda_{0m'}rJ_0(\lambda_{0m'}r)d(\lambda_{0m'}r)$$

$$= \sum_{m=1}^{\infty} \frac{B_{j'0m}j'\pi}{4(1-(-1)^{j'})} \int_0^{\lambda_{0m'}a} r\lambda_{0m'}J_0(\lambda_{0m'}r)J_0(\lambda_{0m}r)d\left(\lambda_{0m'}r\right) \tag{4.54}$$

$$v_0\left(\lambda_{0m'}aJ_1(\lambda_{0m'}a)\right) = \frac{B_{j'0m'}j'\pi}{4(1-(-1)^{j'})}\left(\frac{\lambda_{0m'}^2a^2}{2}\left(J_1^2(\lambda_{0m'}a)\right)\right) \tag{4.55}$$

$$B_{j0m} = \frac{8v_0(1-(-1)^{j'})}{j'\pi\lambda_{0m'}aJ_1(\lambda_{0m'}a)} \text{ where } j' \in \mathbb{N}, m' \in \mathbb{N} \tag{4.56}$$

Note that to reach Equation 4.55, we used the relations

$$\int_0^a J_0(x)dx = aJ_1(a) \tag{4.57}$$

$$\int_0^a J_0^2(x)dx = \frac{a^2}{2}J_1^2(a) \tag{4.58}$$

$$\int_0^a J_0(c_1x)J_0(c_2x)dx = 0 \text{ where } c_1 \neq c_2 \tag{4.59}$$

Substituting Equation 4.56 into Equation 4.49, we have

$$v(r,\theta,z,t) = \sum_{j=1}^{\infty}\sum_{m=1}^{\infty} \frac{8v_0(1-(-1)^j)}{j\pi\lambda_{0m}aJ_1(\lambda_{0m}a)}J_0(\lambda_{0m}r)\sin\left(\frac{j\pi z}{l}\right)e^{-D\gamma_{j0m}^2t} \tag{4.60}$$

Since only the B_{j0m} are nonzero, we can eliminate k from our notation leaving us with

$$v(r,\theta,z,t) = \sum_{j=1}^{\infty}\sum_{m=1}^{\infty} R_m(r)\Theta_{jm}Z_j(z)T_{jm}(t) \tag{4.61}$$

$$\text{where } B_{jm} = B_{j0m}, R_m = R_{0m}, \Theta_{jm} = \Theta_{j0m} = B_{jm}, T_{jm} = T_{j0m}$$

$$v(r,\theta,z,t) = \sum_{j=1}^{\infty}\sum_{m=1}^{\infty} \frac{8v_0(1-(-1)^j)}{j\pi\lambda_{0m}aJ_1(\lambda_{0m}a)} J_0(\lambda_{0m}r)\sin\left(\frac{j\pi z}{l}\right) e^{-D\gamma_{j0m}^2 t} \tag{4.62}$$

Hence, we now have an algebraic description of the Ca^{2+} diffusion out of a cylindrical nucleus with homogeneous boundary conditions. This solution can be found in Myers (102). What remains to be evaluated is how this changes when we consider the changing $[Ca^{2+}]$ in the cytosol and solve the diffusion problem with an inhomogeneous boundary.

4.2.3 Solve for q(t)$\neq 0$

We solve the inhomogeneous case using a similar approach. First, we expand the function $\frac{dq}{dt}$ as a generalised Fourier series of the eigenfunctions of R, Z, and Θ with time-dependent coefficients Q_{jm}.

$$\frac{\partial q}{\partial t} = \sum_{j=1}^{\infty}\sum_{k=0}^{\infty}\sum_{m=1}^{\infty} Q_{jkm}(t)R_{km}(r)\Theta_{jkm}(\theta)Z_j(z) \tag{4.63}$$

Substituting Equation 4.34 and Equation 4.63 into Equation 4.4:

$$\begin{aligned}
&\sum_{j=1}^{\infty}\sum_{k=0}^{\infty}\sum_{m=1}^{\infty} R_{km}Z_j\Theta_{jkm}\frac{dT_{jkm}}{dt} = \\
&\quad D\Bigg(\sum_{j=1}^{\infty}\sum_{k=0}^{\infty}\sum_{m=1}^{\infty} T_{jkm}\Bigg(\left(\frac{d^2R_{km}}{dr^2}+\frac{1}{r}\frac{dR_{km}}{dr}\right)\Theta_{jkm}Z_j \\
&\qquad + \frac{1}{r^2}R_{km}\frac{d\Theta_{jkm}}{d\theta}Z_j + R_{km}\Theta_{jkm}\frac{d^2Z_j}{dz^2}\Bigg)\Bigg) \\
&\qquad - \sum_{j=1}^{\infty}\sum_{k=0}^{\infty}\sum_{m=1}^{\infty} Q_{jkm}(t)R_{km}(r)\Theta_{jkm}(\theta)Z_j(z)
\end{aligned} \tag{4.64}$$

From subsection 4.2.2, we know that $v = R(r)\Theta(\theta)Z(z)T(t)$ satisfies $\frac{\partial v}{\partial t} = D\nabla^2 v$. Following a similar procedure and substituting $v = R(r)\Theta(\theta)Z(z)T(t)$ and $\frac{\partial q}{\partial t} = Q(t)R(r)\Theta(\theta)Z(z)$ into Equation 4.4, Equations 4.27, 4.13, and 4.20 can again be obtained for $R(r)$, $Z(z)$, and $\Theta(\theta)$. Hence, we have the same eigenfunctions and eliminate k from the notation, as in Equation 4.61.

$$\begin{aligned}\sum_{j=1}^{\infty}\sum_{m=1}^{\infty} R_m Z_j \Theta_{jm}\frac{dT_{jm}}{dt} = \\ D\Bigg(\sum_{j=1}^{\infty}\sum_{m=1}^{\infty} T_{jm}\Bigg(-\left((\gamma_{jm}^2 - \mu_j^2) - \frac{1}{r^2}\phi^2\right) R_m\Theta_{jm}Z_j \\ + \frac{\phi^2}{r^2}R_m\Theta_{jm}Z_j - \mu_j^2 R_m\Theta_{jm}Z_j\Bigg)\Bigg) \\ - \sum_{j=1}^{\infty}\sum_{m=1}^{\infty} Q_{jm}(t)R_m(r)\Theta_{jm}(\theta)Z_j(z) \qquad (4.65) \\ \text{where } Q_{jm} = Q_{j0m}\end{aligned}$$

$$\sum_{j=1}^{\infty}\sum_{m=1}^{\infty} R_m Z_j \Theta_{jm}\frac{dT_{jm}}{dt} = \sum_{j=1}^{\infty}\sum_{m=1}^{\infty}\left(-D\gamma_{jm}^2 T_{jm} - Q_{jm}\right)\left(R_m\Theta_{jm}Z_j\right) \qquad (4.66)$$

Using the orthogonality of R, Θ, and Z, we see that

$$\frac{dT_{jm}}{dt} = -D\gamma_{jm}^2 T_{jm} - Q_{jm} \qquad (4.67)$$

As $\gamma = \gamma_{jm} = \gamma_{j0m}$ from the eigenvalues of the solutions for R, Θ, and Z, the eigenfunctions T_{jm} satisfy

$$T_{jm}(t) = -e^{-D\gamma_{jm}^2 t}\int_0^t e^{D\gamma_{jm}^2 s}Q_{jm}(s)ds + C_{jm}e^{-D\gamma_{jm}^2 t} \qquad (4.68)$$

Without loss of generality, at $t = 0$ we set

$$T_{jm}(0) = C_{jm} = 1 \qquad (4.69)$$

Returning to Equation 4.63, we find Q_{jm} by taking advantage of the orthogonality of the eigenfunctions again. Then

$$Q_{jm}(t) = \frac{\int_0^l \int_0^{2\pi} \int_0^a \frac{\partial q}{\partial t}(t) R_m(r) \Theta_{jm}(\theta) Z_j(z) r dr d\theta dz}{\int_0^a R_m^2(r) r dr \int_0^{2\pi} \Theta_{jm}^2(\theta) d\theta \int_0^l Z_j^2(z) dz} \quad \text{where } j, m \in \mathbb{N} \tag{4.70}$$

Resolving the integrals in Equation 4.70, we have:

$$\begin{aligned}
Q_{jm}(t) &= \frac{\partial q}{\partial t}(t) \frac{\lambda_m^2 \int_0^a R_m(r) r dr \int_0^{2\pi} \Theta_{jm}(\theta) d\theta \int_0^l Z_j(z) dz}{\lambda_m^2 \int_0^a R_m^2(r) r dr \int_0^{2\pi} \Theta_{jm}^2(\theta) d\theta \int_0^l Z_j^2(z) dz} \qquad (4.71) \\
&= \frac{\partial q}{\partial t} \frac{\int_0^a \lambda_m r J_0(\lambda_m r) d(\lambda_m r) \int_0^{2\pi} B_{jm} d\theta \int_0^l \sin(\frac{j\pi z}{l}) dz}{\int_0^a J_0^2(\lambda_m r) \lambda_m r d(\lambda_m r) \int_0^{2\pi} B_{jm}^2 d\theta \int_0^l \sin^2(\frac{j\pi z}{l}) dz} \\
&= \frac{\partial q}{\partial t} \frac{\left[\lambda_{m'} r J_1(\lambda_m r)\right]_0^a (2\pi B_{jm}) \left(\frac{(1-(-1)^j)l}{j\pi}\right)}{\left[\frac{1}{2}\lambda_m^2 r^2 \left(J_0^2(\lambda_m r) + J_1^2(\lambda_m r)\right)\right]_0^a \left(2\pi B_{jm}^2\right) \left(\frac{l}{2}\right)} \\
&= \frac{\partial q}{\partial t} \frac{\left(\lambda_m a J_1(\lambda_m a)\right) (2\pi B_{jm}) \left(\frac{l(1-(-1)^j)}{j\pi}\right)}{\left(\frac{1}{2}\lambda_m^2 a^2 \left(J_0^2(\lambda_m a) + J_1^2(\lambda_m a)\right)\right) \left(2\pi B_{jm}^2\right) \left(\frac{l}{2}\right)} \\
&= \frac{\partial q}{\partial t} \frac{1}{B_{jm}} \frac{4(1-(-1)^j)}{j\pi \lambda_m a J_1(\lambda_m a)} \\
&= \frac{\partial q}{\partial t} \frac{j\pi \left(\lambda_m a \left(J_1(\lambda_m a)\right)\right)}{4v_0(1-(-1)^j)} \frac{4(1-(-1)^j)}{j\pi \lambda_m a J_1(\lambda_m a)} \\
Q_{jm}(t) &= \frac{1}{v_0} \frac{\partial q}{\partial t} \qquad (4.72)
\end{aligned}$$

Substituting C_{jm} and Q_{jm} into Equation 4.68 we have:

$$T_{jm} = -\frac{1}{v_0} e^{-D\gamma_{jm}^2 t} \int_0^t e^{D\gamma_{jm}^2 s} \frac{\partial q}{\partial t}(s) ds + e^{-D\gamma_{jm}^2 t} \tag{4.73}$$

Combining these functions, we find $v(r, \theta, z, t)$:

$$v(r, \theta, z, t) = RZ\Theta T \tag{4.74}$$

$$v(r, \theta, z, t) = \sum_{j=1}^{\infty}\sum_{m=1}^{\infty} \left(J_0(\lambda_m r)\right)\left(\sin\left(\frac{j\pi z}{l}\right)\right)\left(\frac{8v_0(1-(-1)^j)}{(j\pi\lambda_m a J_1(\lambda_m a)}\right) \tag{4.75}$$

$$\times\left(-\frac{1}{v_0}e^{-D\gamma_{jm}^2 t}\int_0^t e^{D\gamma_{jm}^2 s}\frac{\partial q}{\partial t}(s)ds + e^{-D\gamma_{jm}^2 t}\right) \tag{4.76}$$

$$v(r, \theta, z, t) = -\sum_{j=1}^{\infty}\sum_{m=1}^{\infty}\frac{8(1-(-1)^j)\sin\left(\frac{j\pi z}{l}\right)J_0(\lambda_m r)}{j\pi\lambda_m a J_1(\lambda_m a)}$$

$$\times\left(e^{-D\gamma_{jm}^2 t}\int_0^t e^{D\gamma_{jm}^2 s}\frac{\partial q}{\partial t}(s)ds - v_0 e^{-D\gamma_{jm}^2 t}\right) \tag{4.77}$$

$$c(r, \theta, z, t) = v(r, \theta, z, t) + q(t) \tag{4.78}$$

Hence, the solution to our model is:

$$c(r, \theta, z, t) = -\sum_{j=1}^{\infty}\sum_{m=1}^{\infty}\frac{\sin\left(\frac{j\pi z}{l}\right)J_0(\lambda_m r)(1-(-1)^j)}{j\pi\lambda_m a J_1(\lambda_m a)}$$

$$\times\left(e^{-D\gamma_{jm}^2 t}\int_0^t e^{D\gamma_{jm}^2 s}\frac{\partial q}{\partial t}(s)ds - v_0 e^{-D\gamma_{jm}^2 t}\right) + q(t) \tag{4.79}$$

where $\gamma_{jm}^2 = \lambda_m^2 + \left(\frac{j\pi}{l}\right)^2$.

4.2.4 1D solution

We can solve the 1D system in a similar manner. The system is described as:

$$\frac{\partial c}{\partial t} = D\left(\frac{\partial^2 c}{\partial r^2} + \frac{1}{r}\frac{\partial c}{\partial r}\right) \tag{4.80}$$

With boundary conditions:

$$c(r, 0) = c_0, \tag{4.81}$$

$$\text{and } c(a, t) = q(t). \tag{4.82}$$

We let $v(r,t) = c(r,t) - q(t)$, and assuming no spatial dependence in q,

$$\begin{aligned}\frac{\partial v}{\partial t} &= \frac{\partial c}{\partial t} - \frac{\partial q}{\partial t} \\ \frac{\partial v}{\partial r} &= \frac{\partial c}{\partial r} - \frac{\partial q}{\partial r} \\ &= \frac{\partial c}{\partial r}.\end{aligned}$$

Then

$$\frac{\partial v}{\partial t} = D\left(\frac{\partial^2 v}{\partial r^2} + \frac{1}{r}\frac{\partial v}{\partial r}\right) - \frac{\partial q}{\partial t} \tag{4.83}$$

subject to

$$v(r,0) = c_0 - q_0 = v_0, \text{constant}, \tag{4.84}$$

$$\text{and } v(a,t) = 0. \tag{4.85}$$

We now have a system with homogeneous boundary conditions. $v(r,t)$ is again separable so

$$v(r,t) = R(r)T(t) \tag{4.86}$$

where the eigenfunction solutions can be shown to be $R(r) = J_0(\lambda_k r)$ and $T(t) = e^{-D\lambda_k^2 t}$ in the same manner as above where λ_k^2 is the separation constant. As above, λ_k^2 must be positive to obtain a nontrivial solution. Then

$$c(r,t) = -\sum_{k=1}^{\infty} \frac{2J_0(\lambda_k r)}{\lambda_k a J_1(\lambda_k a)} \left(e^{-D\lambda_k^2 t}\int_0^t e^{D\lambda_k^2 s}\frac{\partial q}{\partial t}(s)ds - v_0 e^{-D\lambda_k^2 t}\right) + q(t) \tag{4.87}$$

$$\text{where } \lambda_k = \frac{\nu_k}{a} \tag{4.88}$$

Here ν_k is the kth root of $J_0(\nu) = 0$.

Relevant integrals for implementation

To find a completely analytical solution, we need algebraic solutions to the integrals in Equations 4.79 and 4.87:

$$e^{-D\gamma_{jm}^2 t}\int_0^t e^{D\gamma_{jm}^2 s}\frac{\partial q}{\partial t}(s)ds \tag{4.89}$$

If $q(t)$ is a spline, we can integrate each section independently. Approximating $q(t)$ as a cubic spline, with

$$q(t) = ut^3 + vt^2 + wt + x \qquad u, v, w, x \in \mathbb{R} \tag{4.90}$$

$$\frac{\partial q}{\partial t}(t) = 3ut^2 + 2vt + w \tag{4.91}$$

we can now evaluate the definite integral with each term independently on an interval $[t_1, t_2]$. For constant

w:

$$e^{-D\gamma_{jm}^2 t}\int_{t_1}^{t_2} e^{D\gamma_{jm}^2 s}w ds = e^{-D\gamma_{jm}^2 t}\left[\frac{w}{D\gamma_{jm}^2}e^{D\gamma_{jm}^2 s}\right]_{t_1}^{t_2} \tag{4.92}$$

$$= \frac{w}{D\gamma_{jm}^2}\left(e^{D\gamma_{jm}^2(t_2-t)} - e^{D\gamma_{jm}^2 s(t_1-t)}\right) \tag{4.93}$$

2vt:

$$e^{-D\gamma_{jm}^2 t}\int_{t_1}^{t_2} e^{D\gamma_{jm}^2 s}2vs ds = e^{-D\gamma_{jm}^2 t}\frac{2v}{\left(D\gamma_{jm}^2\right)^2}\left[e^{D\gamma_{jm}^2 s}\left(\left(D\gamma_{jm}^2\right)s - 1\right)\right]_{t_1}^{t_2}$$

$$= \frac{2v}{\left(D\gamma_{jm}^2\right)^2}\Bigg(e^{D\gamma_{jm}^2(t_2-t)}\left(\left(D\gamma_{jm}^2\right)t_2 - 1\right)$$

$$- e^{D\gamma_{jm}^2(t_1-t)}\left(\left(D\gamma_{jm}^2\right)t_1 - 1\right)\Bigg) \tag{4.94}$$

$3ut^2$:

$$
\begin{aligned}
& e^{-D\gamma_{jm}^2 t}\int_{t_1}^{t_2} e^{D\gamma_{jm}^2 s} 3us^2 ds \\
&= e^{-D\gamma_{jm}^2 t}\frac{3u}{\left(D\gamma_{jm}^2\right)^3}\left[e^{D\gamma_{jm}^2 s}\left(\left(D\gamma_{jm}^2\right)^2 s^2 - 2\left(D\gamma_{jm}^2\right)s + 2\right)\right]_{t_1}^{t_2} \qquad (4.95)\\
&= \frac{3u}{\left(D\gamma_{jm}^2\right)^3}\Bigg(e^{D\gamma_{jm}^2(t_2-t)}\left(\left(D\gamma_{jm}^2\right)^2 t_2^2 - 2D\gamma_{jm}^2 t_2 + 2\right) \\
&- \left(e^{D\gamma_{jm}^2(t_1-t)}\left(\left(D\gamma_{jm}^2\right)^2 t_1^2 - 2D\gamma_{jm}^2 t_1 + 2\right)\right)\Bigg) \qquad (4.96)
\end{aligned}
$$

Then the full solution to Equation 4.89 over the interval $[t_1, t_2]$ is:

$$
\begin{aligned}
& e^{-D\gamma_{jm}^2 t}\int_{t_1}^{t_2} e^{D\gamma_{jm}^2 s}\frac{\partial q}{\partial t}(s)ds \\
&= e^{-D\gamma_{jm}^2 t}\int_{t_1}^{t_2} e^{D\gamma_{jm}^2 s}\left(3us^2 + 2vs + w\right)ds \\
&= e^{D\gamma_{jm}^2(t_2-t)}\left(\frac{w}{D\gamma_{jm}^2} + \frac{2v}{\left(D\gamma_{jm}^2\right)^2}\left(\left(D\gamma_{jm}^2\right)t_2 - 1\right) + \frac{3u}{\left(D\gamma_{jm}^2\right)^3}\left(\left(D\gamma_{jm}^2\right)^2 t_2^2 - 2D\gamma_{jm}^2 t_2 + 2\right)\right) \\
&- e^{D\gamma_{jm}^2(t_1-t)}\left(\frac{w}{D\gamma_{jm}^2} + \frac{2v}{\left(D\gamma_{jm}^2\right)^2}\left(\left(D\gamma_{jm}^2\right)t_1 - 1\right) + \frac{3u}{\left(D\gamma_{jm}^2\right)^3}\left(\left(D\gamma_{jm}^2\right)^2 t_1^2 - 2D\gamma_{jm}^2 t_1 + 2\right)\right)
\end{aligned} \qquad (4.97)
$$

Adding together the solutions for each interval of the spline gives us a solution over the entire transient.

4.2.5 Numerical Implementation

The models (Equation 4.79 and Equation 4.87) were implemented using MATLAB 2019a. To save computation time, the infinite sums were truncated to a sum to 300. Code can be found at git@github.com:hilaryh/Nucleus.git. As in Chapter 3, for the majority of simulations run for this chapter, $q(t)$ represents a cubic spline approximating the cytosolic Ca^{2+} transient at the boundary of the nucleus. The same function for $q(t)$ is used in this chapter as in the previous chapter. Example $[Ca^{2+}]$ cross sections of the nucleus from a 3D simulation are shown in Figure 4.4. In this chapter, we show only simulations based on an approximation of Figure 3.2D. Simulated nuclei have radius 2 μm and length 20 μm, approximately the average dimensions measured in experiments.

4.2.6 Output metrics

As in the last chapter, the two main output metrics we examine in this chapter are full duration at half maximum (FDHM) and time to peak (TTP). Although we could not accurately compare the $[Ca^{2+}]$ with the data, we also look at the maximum $[Ca^{2+}]$ reached by the transient at the centre of the nucleus (Max Ca^{2+}).

As depicted in Figure 3.7, the FDHM was measured as the duration for which the concentration of the simulated Ca^{2+} transient was higher than the midpoint between Max Ca^{2+} and c_0. The TTP was measured as the time between initiation of the cytosolic transient and the time at which Max Ca^{2+} was achieved. We also briefly discuss the time to base. This is the length of time between the transient peak and the time at which the $[Ca^{2+}]$ returns to its diastolic concentration.

Measurements are often based on the $[Ca^{2+}]$ at the centre of the simulated nucleus or, if stated, on the average $[Ca^{2+}]$ over a longitudinal cross section of the simulated nucleus.

4.3 Results

4.3.1 Comparison of 1D and 3D analytical solutions

We compare the 1D and 3D solutions of our system in Figure 4.5. Cross-sections of the nucleus are generated from the 1D model by assuming constant $[Ca^{2+}]$ in the z-direction. As one would expect, the differences between the simulations are most apparent at the long ends of the nucleus. However, as we see in Figures 4.6 and 4.7, there is very little difference (less than 0.1% of the minimum output) between them at the centre of the nucleus. Figures 4.6C and 4.7C plot the differences between the 1D and 3D solutions at the centre of the nucleus. Diffusion in from the ends appears to have little impact on the centre of the nucleus even with a faster rate of diffusion. In Figures 4.6 and 4.7, the difference between the 1D and 3D simulations is most apparent at the tail end of the transient, when Ca^{2+} from the ends of the nucleus has had time to reach the centre.

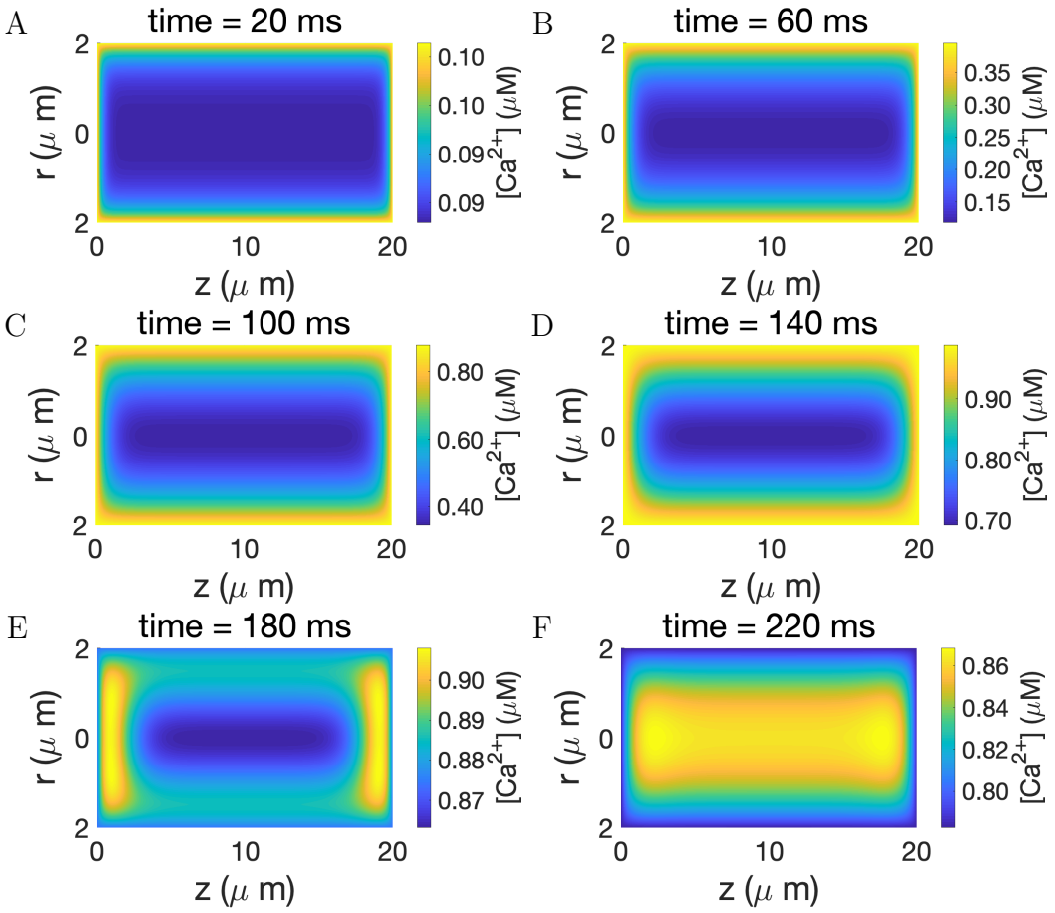

Figure 4.4: $[Ca^{2+}]$ over a cross section of the nucleus at different time points. Plots are all shown at different scales to highlight the diffusion in the z-direction vs diffusion in the r-direction. The diffusion coefficient in these simulations is 0.0174 $\mu m^2/ms$. Times are given post-initiation of the cytosolic Ca^{2+} transient.

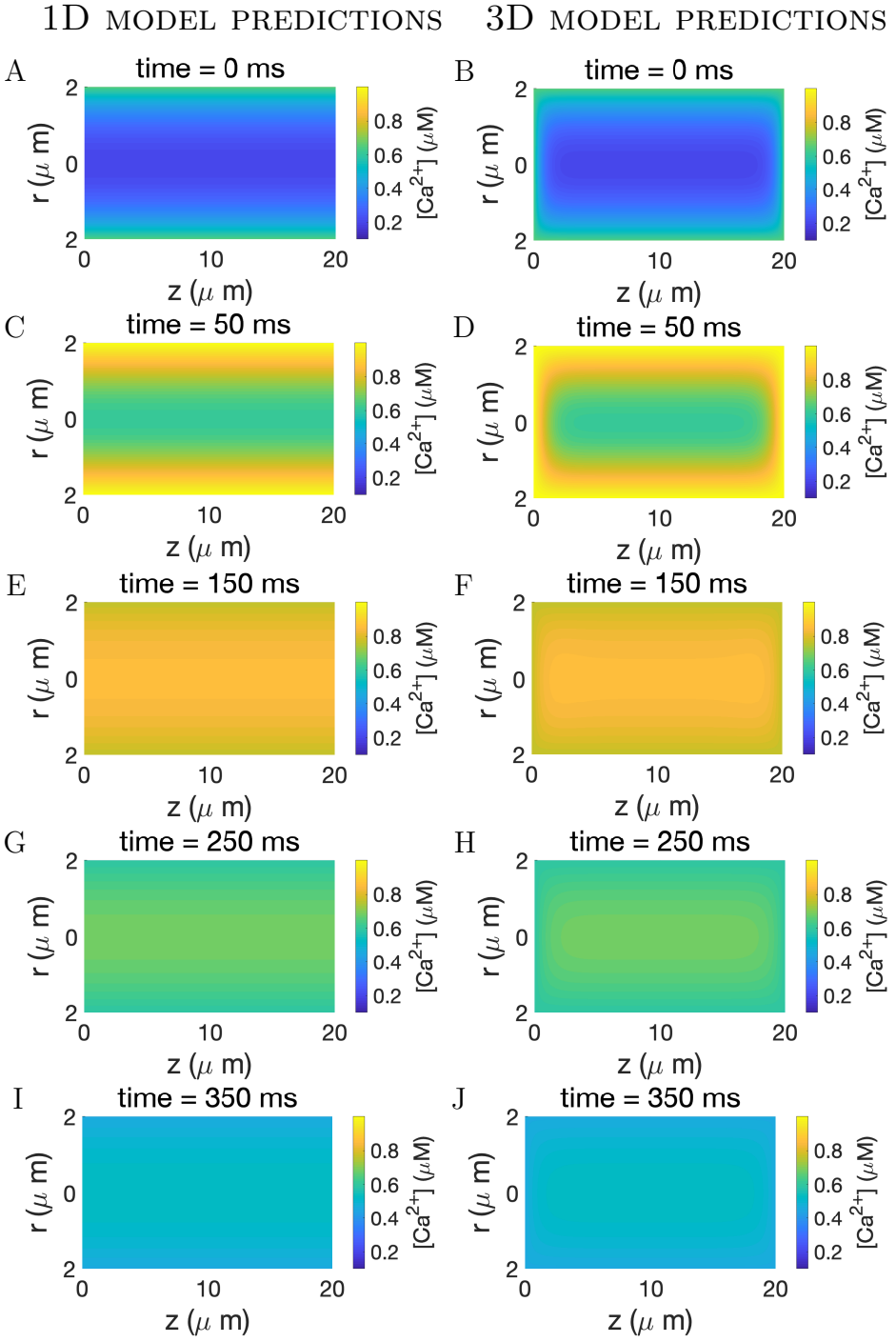

Figure 4.5: Comparison of 1D and 3D models of the nucleus over time. Note the 1D solution does not depend on z. The left column shows the Ca^{2+} concentration in a cross section of the nucleus simulated by our 1D model. The right column shows the Ca^{2+} concentration simulated by our 3D model. Note the differences at the extreme ends of the z-axis are most apparent in plots A-F. Average Ca^{2+} concentration, particularly in the centre of the nucleus, is similar across both simulations. Simulations were run on nuclei of length 20 μm and radius 2 μm with diffusion coefficient 0.0174 $\mu m^2/ms$.

4.3.2 Comparison of 1D analytical solution and the numerical solution

We use our 1D analytical solution to the system of equations describing diffusion into the nucleus to verify our numerical solution from Chapter 3. Figure 4.6 shows the concentration in the centre of the nucleus over time for the 1D and 3D analytical, and the 1D numerical solutions with no buffers and a diffusion coefficient of 1×10^{-3} μm^2/ms on the same plot as the approximated cytosolic Ca^{2+} concentration, q(t). The solutions to the three models are indistinguishable at this scale. Figure 4.6B plots the differences between the two 1D solutions. Similarly, Figure 4.7B shows little change between models even with a faster rate of diffusion.

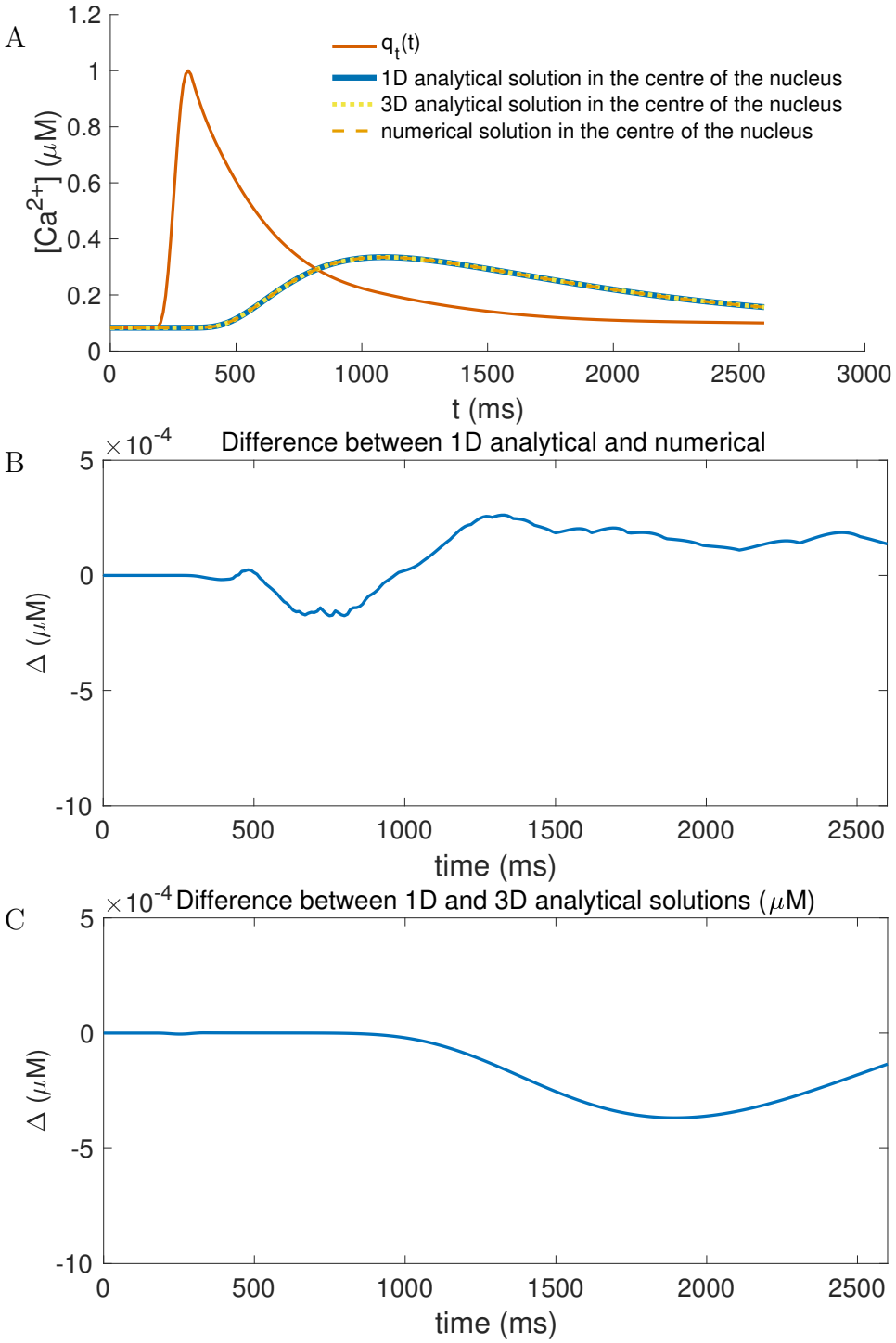

Figure 4.6: (A) Comparison of the solutions of each diffusion model (1D, 3D, 1D numerical) at the centre of the nucleus as well as the concentration of Ca^{2+} diffusing in at the nuclear boundary. Below are the differences between (B) 1D analytical − numerical solutions and (C) 1D − 3D analytical solutions at the centre of the nucleus. Each model was run with diffusion coefficient $D = 10^{-3}$ $\mu m^2/ms$. $q_t(t)$ in the legend refers to the time derivative of $q(t)$, i.e. $\frac{\partial 1}{\partial t}$

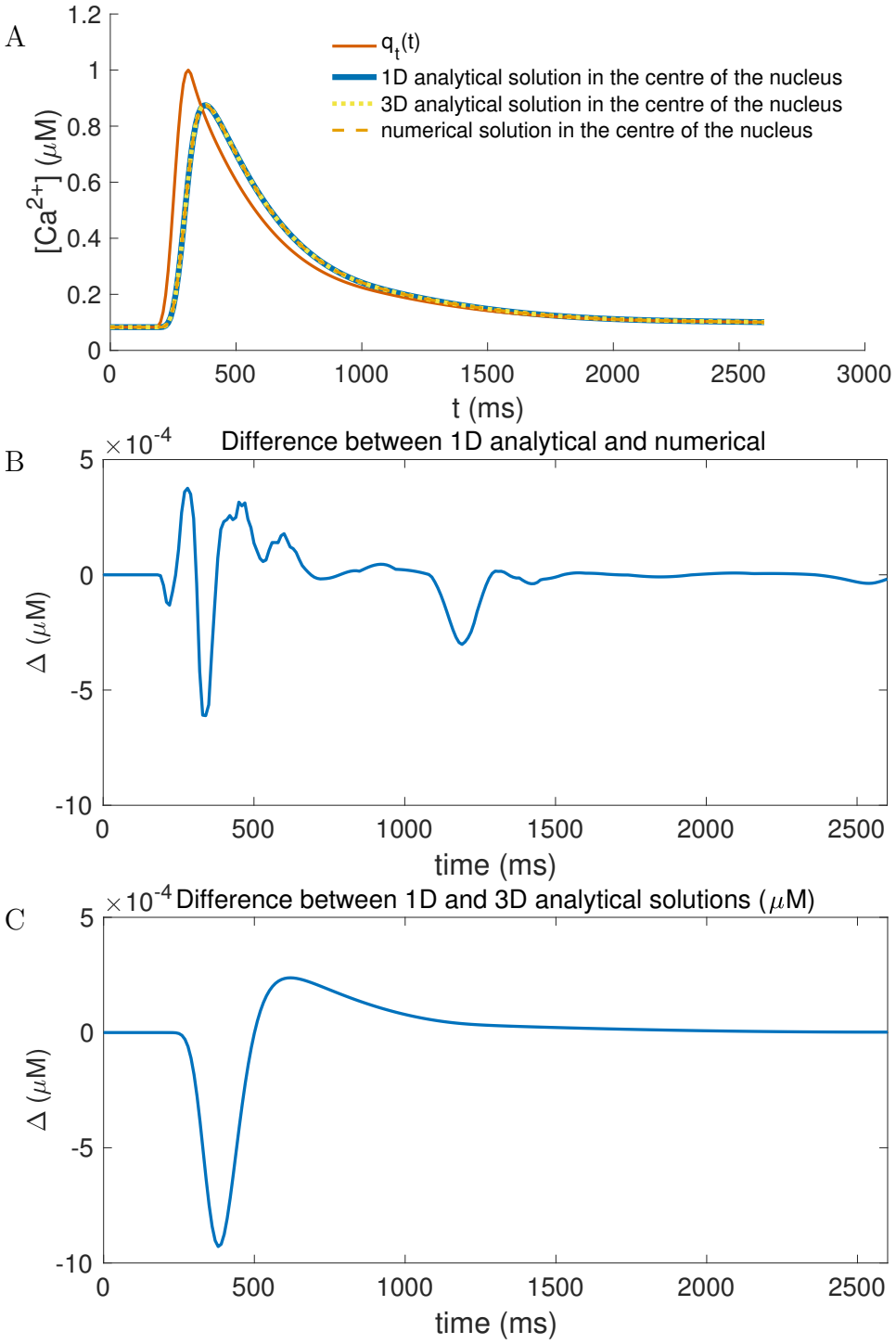

Figure 4.7: (A) Comparison of the solutions of each diffusion model (1D, 3D, 1D numerical) at the centre of the nucleus as well as the concentration of Ca^{2+} diffusing in at the nuclear boundary. Below are the differences between (B) 1D analytical − numerical solutions and (C) 1D − 3D analytical solutions with higher diffusion coefficient. Each model was run with diffusion coefficient $D = 0.0174$ $\mu m^2/ms$. $q_t(t)$ in the legend refers to the time derivative of $q(t)$, i.e. $\frac{\partial 1}{\partial t}$

4.3.3 In which situations does diffusion from the ends of the nucleus start to impact the centre?

From this point onwards, we investigate the importance of geometry in the 3D diffusion model to determine the situations in which it differs from the 1D approximation. If we assume that Ca^{2+} diffusion within the nucleus is isotropic we should assume that diffusion along the minor axes of the nucleus would have the greatest effect on nuclear Ca^{2+} concentration. We see from Figure 4.8 that the greatest impact on the average nuclear $[Ca^{2+}]$ is during the cytosolic Ca^{2+} rise phase, with a faster initial rise in the 3D simulation but a slower plateau resulting in a similar time to peak. Conversely, $[Ca^{2+}]$ decreases faster in the 3D simulation than in the 1D solution, particularly when we take an average that includes the edges of the nucleus. This is due to the additional diffusion flux in the z-direction which allow the ends to respond to changes in cytosolic $[Ca^{2+}]$ more quickly. Both simulations peak faster near the nuclear envelope so the further from the NE we take the average, the later the TTP.

We can see the difference more clearly in Figure 4.5 where the 1D and 3D model solutions are depicted side by side. The $[Ca^{2+}]$ at each end of the nucleus is higher in the 3D simulation where Ca^{2+} is allowed to diffuse in from all sides. However, overall, the two simulations show very similar Ca^{2+} concentrations within the nucleus.

4.3.4 How much of a difference does size of the nucleus make to nuclear calcium dynamics?

The nuclei of cardiomyocytes all take a similarly cylindrical shape. However, even within our small dataset (8 nuclei), we have noticed a fair amount of variation in the size and geometry of male Wistar rat ventricular nuclei (see Figure 3.3). With the sizes of the nuclei measured (shown in more detail in Figure 4.2), if we assume a normal distribution we expect approximately 30% of nuclei to vary by 20% (≈ 1 standard devisation) from the average nucleus size we are simulating. Figure 4.10 shows the $[Ca^{2+}]$ in nuclei of different sizes 180ms after the initiation of the same cytosolic transient. This is approxiately when the nuclear Ca^{2+} transient reaches its maximum $[Ca^{2+}]$ and the difference between in sizes is most apparent. We see from Figure 4.10 that the radius of the nucleus has the greatest effect on the amplitude of the Ca^{2+} transient at its centre, while the length of the nucleus

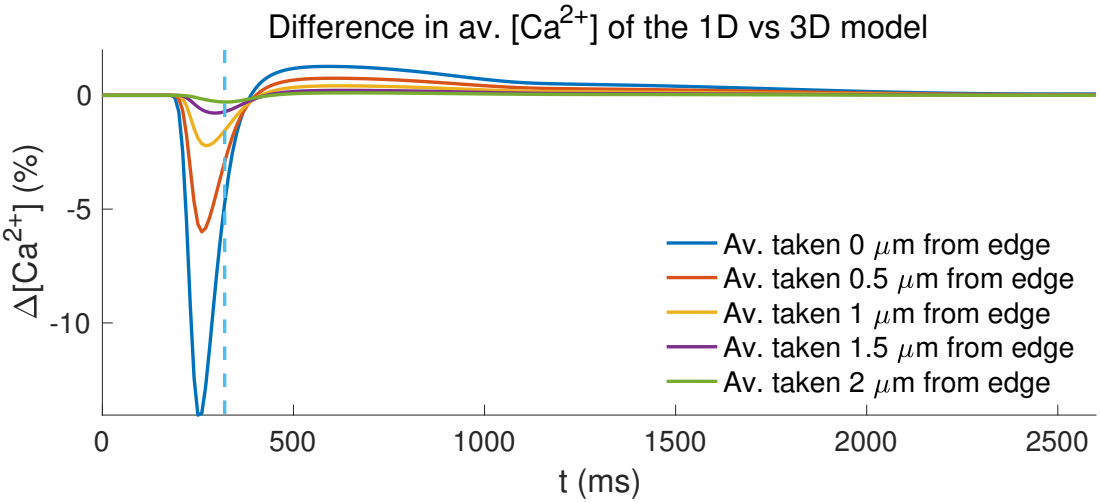

Figure 4.8: Here we show the differences between the average $[Ca^{2+}]$ taken over an area of the longitudinal cross section) in the nucleus of the 1D − 3D models over time, with averages taken at varying distances from the NE. In these simulations, we have modelled nuclei with radius 2 μm and length 20 μm. The more of the nucleus we include in the average, the greater the difference between the two simulations with the 3D average having a greater average $[Ca^{2+}]$, with greater nuclear coverage in our average. The differences in average concentration between simulations are at least an order of magnitude smaller than the concentrations we see in the nucleus unless we include the whole nucleus (where the $[Ca^{2+}]$ at the boundary is essentially equal to that in the cytosol).

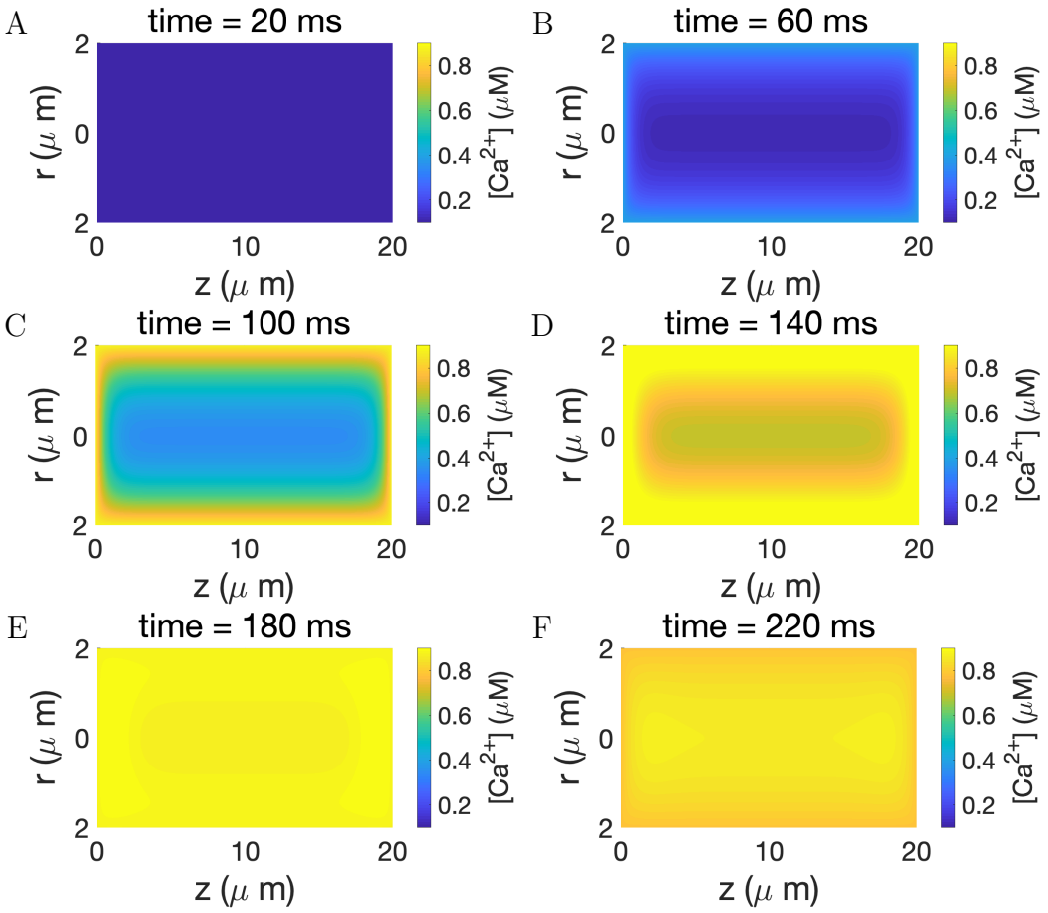

Figure 4.9: $[Ca^{2+}]$ over a cross section of the nucleus at different time points. Plots are all shown at the same scale to better show change in Ca^{2+} concentration in the nucleus as a whole. The diffusion coefficient in these simulations is 0.0174 $\mu m^2/ms$. Times are given post-initiation of the cytosolic Ca^{2+} transient.

appears to make very little difference. The edge effects at $z = 0$ and $z = l$ appear to be l-dependent, but are affected by the radius ofthe nucleus. Even simulations of nuclei with 80% of the average length show very little change compared to the stark difference between the $[Ca^{2+}]$ in nuclei of different radii. The effect of the difference in length vs radius on Max Ca^{2+}, FDHM, TTP, and time to base in shorter nuclei is summarised in Figure 4.11. Additionally, it is evident that in our dataset the variation in $[Ca^{2+}]$ due to variation in the sizes of cardiac nuclei is far greater than the variation within a single nucleus of average size.

4.3.5 How much does the angle of the line-scan affect measured nuclear calcium concentration?

An issue in interpreting line-scan data is that the alignment of the scan with respect to the z-axis of the nucleus might affect the results. Depicted in Figure 4.12A we show that at the effective diffusion coefficient of Ca^{2+} in the nucleus, 0.0174 $\mu m^2/ms$, the angle of the line-scan makes little difference to the average Ca^{2+} transient seen. However, small differences do have a greater relative effect on quantities like the TTP (see Figure 4.13). The effect of line-scan angle would be greater if the diffusion coefficient, D were smaller. Figure 4.12B depicts simulations at the same angles with smaller diffusion coefficient, D to better show the effect of angle on the average transient measured with a line-scan.

Figures 4.13 and 4.14 show the percentage change in TTP and FDHM with angle for the same values of D. The change in FDHM is barely noticeable with either value of D. The change in TTP with angle is only a few percent with higher D but far more substantial with lower D.

4.3.6 Effect of cumulative transient changes on nuclear calcium

At $D = 0.0174\ \mu m^2 ms^{-1}$, Ca^{2+} movement is fast enough that nuclear $[Ca^{2+}]$ is back at resting levels within 3 s (the period of $[Ca^{2+}]$ oscillation in our data). Shortening this period to 1 s we find the same result. Figure 4.15 shows the simulated cytosolic and nuclear transient over multiple beats at 1 Hz.

As the system has returned to rest prior to the next stimulus, the response is also periodic and does not change over subsequent oscillations. This means that at 0.3 Hz, altered transients, i.e. transients with greater amplitude or FDHM,

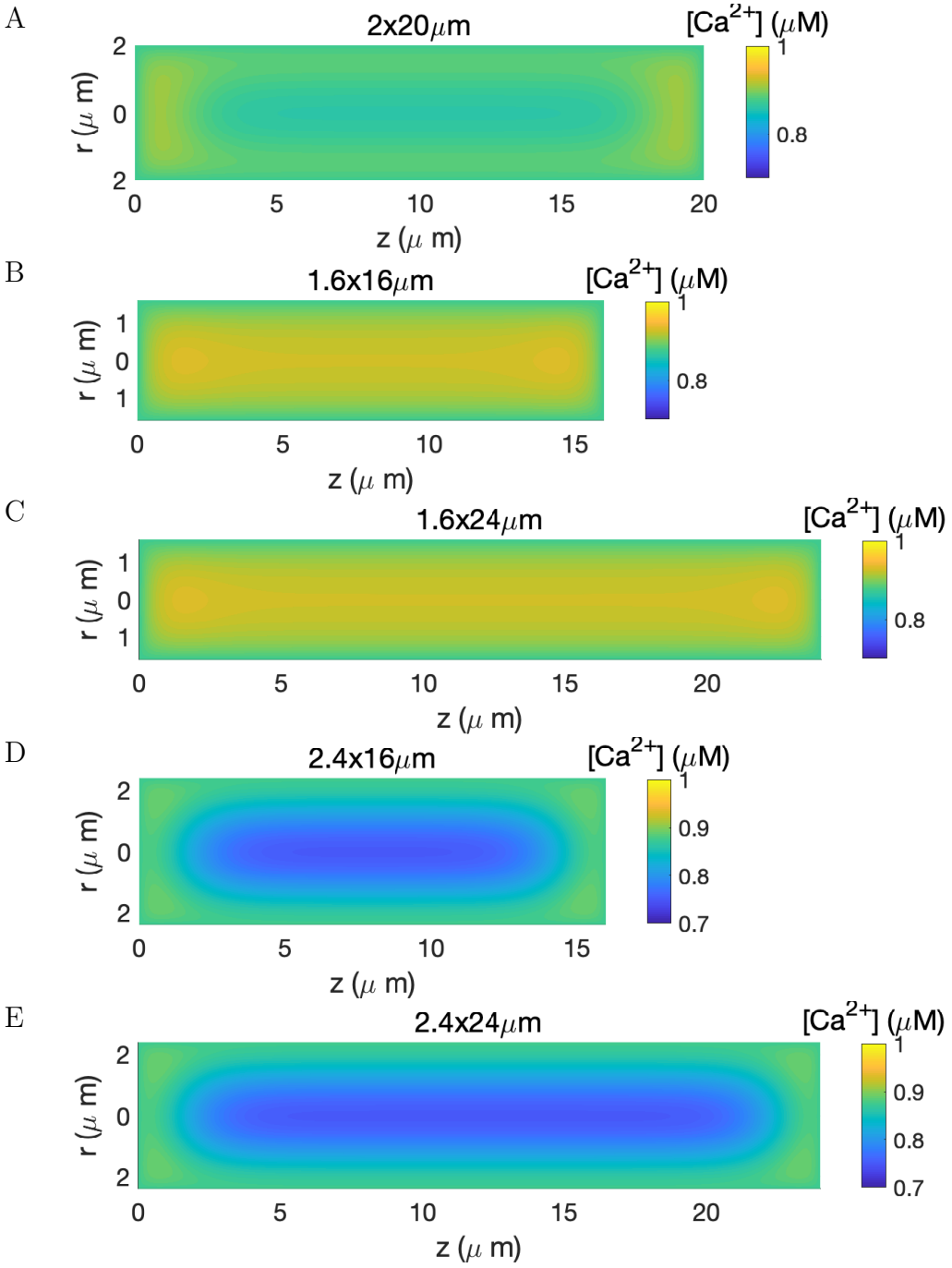

Figure 4.10: Examination of the effect of nucleus size on the $[Ca^{2+}]$ inside the nucleus. Nucleus sizes are to scale. Each plot depicts the $[Ca^{2+}]$ in the nucleus 180 ms after the start of a cytosolic transient. Each simulation was run with $D_c = 0.0174$ $\mu m^2/ms$. The full nucleus is shown in each plot.

have a similar effect over multiple beats as they do initially (see Figure 4.11D). Simulating the transient at a 5.5 Hz by repeating only the first 180 ms of the

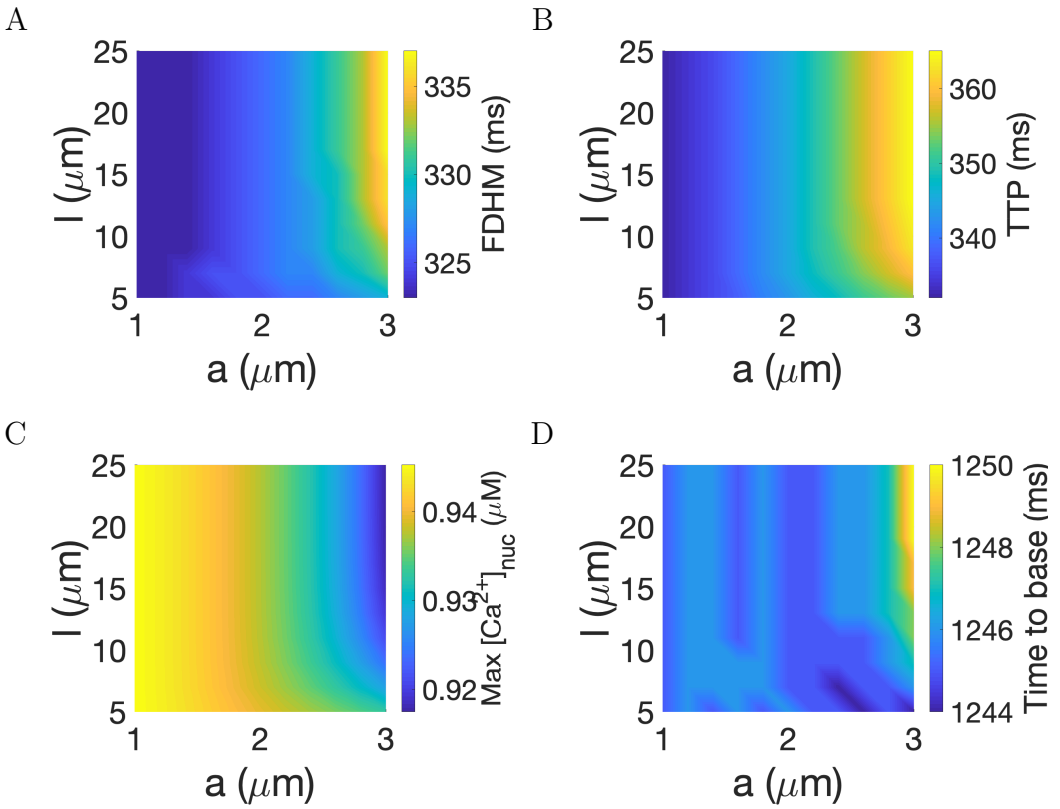

Figure 4.11: Effect of nucleus dimensions on the FDHM, TTP, Max Ca^{2+} , and time to base of the transient at the centre of the nucleus. The diffusion coefficient in these simulations is 0.0178 $\mu m^2/ms$.

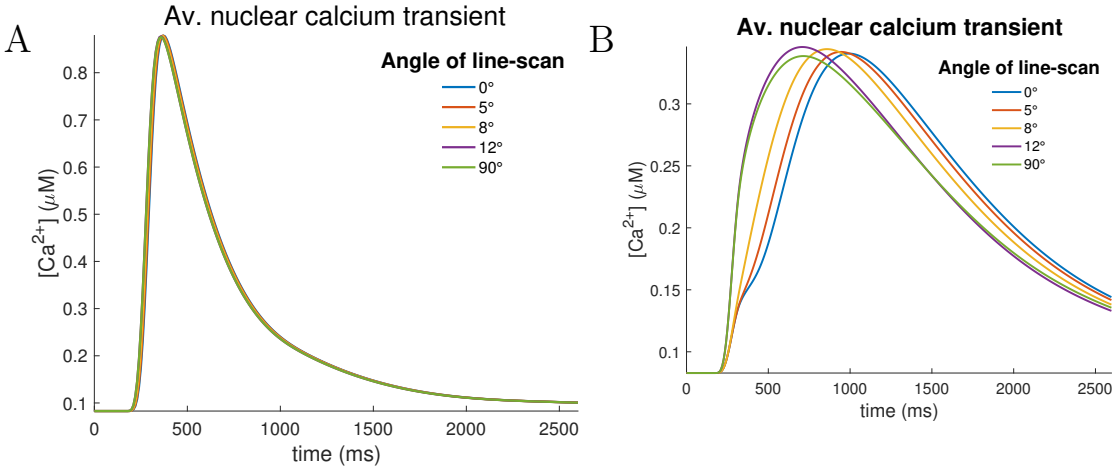

Figure 4.12: Comparison of the average visible Ca^{2+} concentration in the nucleus over time along a line-scan at various angles with the z-axis. (A) was run with diffusion coefficient $D = 0.0174\ \mu m^2/ms$ while (B) was run with diffusion coefficient $D = 10^{-3}\ \mu m^2/ms$.

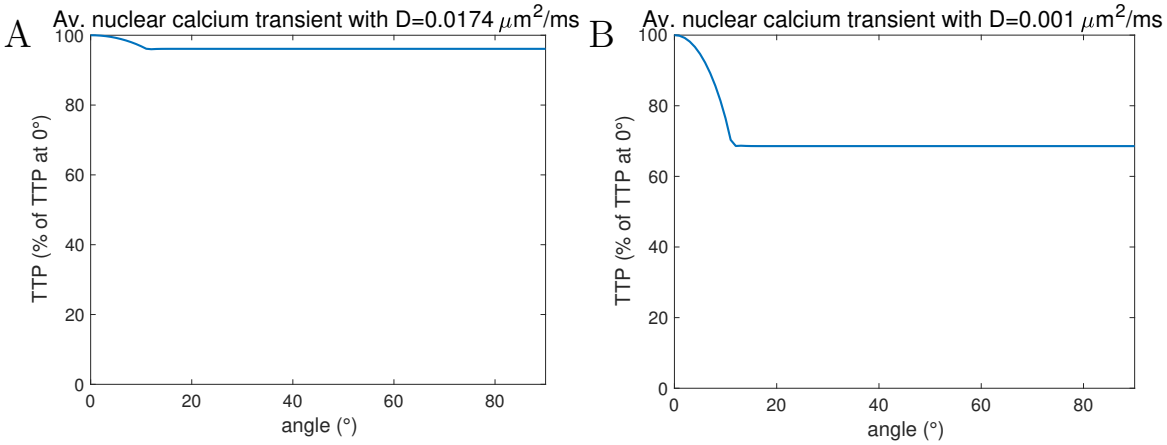

Figure 4.13: Comparison of the TTP of the average visible Ca^{2+} concentration in the nucleus with the angle of the line-scan with the z-axis. (A) was run with diffusion coefficient $D = 0.0174\ \mu m^2/ms$ while (B) was run with diffusion coefficient $D = 10^{-3}\ \mu m^2/ms$.

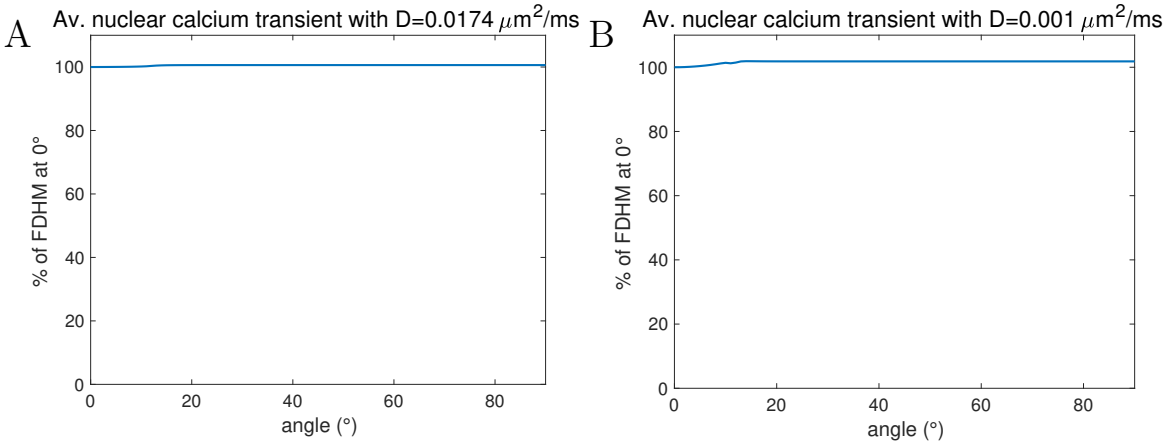

Figure 4.14: Comparison of the FDHM of the average visible Ca^{2+} concentration in the nucleus with the angle of the line-scan with the z-axis. (A) was run with diffusion coefficient $D = 0.0174\ \mu m^2/ms$ while (B) was run with diffusion coefficient $D = 10^{-3}\ \mu m^2/ms$.

experimental cytosolic transient (see Figure 4.15), we begin to see changes to both the initial nuclear transient and those following. In this case, modifying the characteristics of the cytosolic Ca^{2+} transient results in less straightforward alterations to the nuclear Ca^{2+} transient. Cytosolic transients with greater FDHM result in nuclear transients with greater overall $[Ca^{2+}]$ – both peak and diastolic.

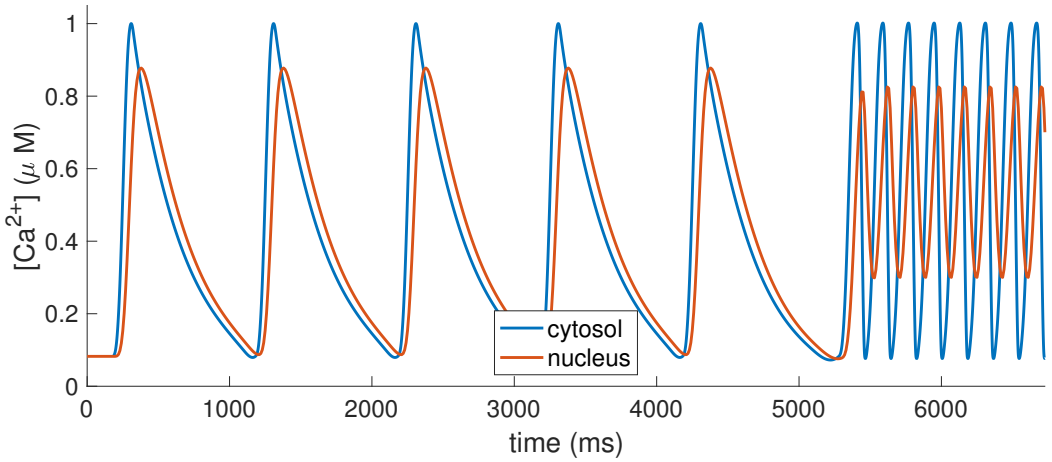

Figure 4.15: Simulations of cytosolic and nuclear Ca^{2+} oscillations run at $D = 0.0174$ $\mu m^2/ms$. The periodic cytosolic signal starts at 1 Hz before increasing in frequency to 5.5 Hz, closer to the frequency of rat heart beats, after 5300 ms. The Ca^{2+} in the nucleus is able to return to resting Ca^{2+} levels at the end of each transient when paced at 1 Hz so the difference between transients is minimal. However at 5.5 Hz nuclear $[Ca^{2+}]$ does not have time to return to diastolic $[Ca^{2+}]$ and nuclear diastolic $[Ca^{2+}]$ is permanently elevated in comparison to the cytosol. The cytosolic transient was generated from attenuated data which was originally obtained from rat ventricular myocytes paced at 0.3 Hz (see Section 3.2).

4.4 Discussion

We have compared the 3D and 1D simulations of Ca^{2+} dynamics in the nucleus. In the majority of the nuclear space, there is little difference between the $[Ca^{2+}]$ predicted by either solution. The radius of the nucleus has a greater impact on overall nuclear $[Ca^{2+}]$ than the length. The 1D model does not account for the end effects. However, if we expect hypertrophic gene regulation to occur throughout the nucleus or primarily near the centre, the 1D simulation is sufficient to predict nuclear $[Ca^{2+}]$.

Additionally, we have shown that, at the estimated Ca^{2+} diffusion coefficient, $d = 0.0174$ $\mu m^2 ms^{-1}$, the alignment of a line-scan through the nucleus makes little difference to the overall nuclear $[Ca^{2+}]$ measured. Fast paced contractions can raise the diastolic nuclear $[Ca^{2+}]$ in the nucleus above that of the cytosol. If we assume a similar rate of rise and fall of $[Ca^{2+}]$ in the cells of rats *in vivo*, basal nuclear $[Ca^{2+}]$ is likely to be elevated above the cytosol by several hundred nanomolar (the 5.5 Hz paced part of Figure 4.15). At resting human pacing ($\approx$ 1 Hz), we see little change between the diastolic $[Ca^{2+}]$ of the cytosol and

nucleus (the initial part of Figure 4.15). However there are differences between the Ca^{2+} channels between humans and rats so our simulations will not be entirely representative.

4.4.1 The importance of modelling spatial calcium dynamics in the nucleus

The nuclei of cardiomyocytes are often treated as a single homogeneous compartment, or two identical ones. Here too, we have generally looked at the bulk nuclear [Ca^{2+}] or the [Ca^{2+}] in the centre of the nucleus and assumed that the edge of the nucleus, being so similar to the cytosol is of less importance. Whether this is a valid assumption in the context of NFAT-mediated Ca^{2+} signalling or we require a more spatially nuanced understanding remains to be determined. NFAT4 localisation, post-dephosphorylation, in HEK293 cells shows NFAT uniformly distributed across the whole of the nucleus, except for the nucleolus (65). The location and potential movement of the relevant DNA within the nucleus is unknown. Further research may reveal that a more detailed distribution of Ca^{2+} is necessary to understand NFAT-mediated gene expression. However, our simulations suggest that a nuclear average should suffice. As such, a 1D simulation of Ca^{2+} dynamics in the nucleus should be sufficient to understand NFAT activity within the cytosol.

4.4.2 Nuclear calcium and NFAT

We have very little data on what the hypertrophic Ca^{2+} signal in the nucleus must look like in order to allow NFAT-mediated gene expression. However, it has been hypothesised that NFAT must remain bound to calcineurin within the nucleus to effect gene expression (128, 14). This seems to indicate that a similar Ca^{2+} signal for CnA to bind to and dephosphorylate NFAT in the cytosol must also be present in the nucleus to allow NFAT to remain bound and in its dephosphorylated state and enact gene expression. However, it is possible that the exact nature of the required Ca^{2+} signal may be affected by competitive binding within the nucleus. We showed in Chapter 3 that a change in Ca^{2+} dynamics within the cytosol translated to a similar change to Ca^{2+} dynamics within the nucleus such as an increase in Max [Ca^{2+}] within both. The same trends are true after multiple Ca^{2+} transients. However, these trends may not hold in cells paced at

higher frequencies, particularly if the action of SERCA does not correspondingly increase, as it does at higher temperatures (88). If the time to base is greater than the period of oscillation (as we see in the 5.5 Hz paced part of Figure 4.15), we see an increase in basal $[Ca^{2+}]$. In these conditions, an increase in cytosolic FDHM, could result in a step increase in average nuclear $[Ca^{2+}]$ with each oscillation, and eventually both an increase in nuclear maximum transient amplitude and basal $[Ca^{2+}]$. Further simulations taking into account both the pacing frequency and Ca^{2+} pump behaviour *in vivo* would be worth exploring.

4.4.3 Limitations of the model

Our model assumes a regularly shaped nucleus, i.e. few nuclear invaginations, and homogeneous Ca^{2+} release around the nucleus. While synchronised Ca^{2+} release, and organised RyR distribution across the cell is important for cardiomyocyte function, Ca^{2+} release in response to an electrical stimulus is not always uniform (52). Hence, a spatially uniform transient at the nuclear envelope is only an approximation of cardiomyocyte Ca^{2+} dynamics. RyRs are located on the Z-discs, meaning that they can be found in bands spread 2 μm apart, approximately perpendicular to the nucleus (see subsection 1.1.2). We can see some of the variation in $[Ca^{2+}]$ at the nuclear envelope in Figure 3.2. However, this is still only a 1D view of the nuleus, and we can see clearly in Figure 3.2E that at a border where there appears to be very little Ca^{2+} at the nuclear envelope, Ca^{2+} is diffusing into the nucleus from a different direction and more than matches the $[Ca^{2+}]$ at the other end the nucleus in the same linescan. With a slightly faster diffusion rate of Ca^{2+} in the cytosol, $[Ca^{2+}]$ at the nuclear envelope will partially average out, and our model will still give a fair approximation of overall nuclear Ca^{2+} dynamics.

4.4.4 Conclusion

In terms of the average $[Ca^{2+}]$ within the nucleus, the natural variation in nuclear radius appears to have a greater effect than Ca^{2+} than longitudinal Ca^{2+} diffusion. The importance of spatial variation in $[Ca^{2+}]$ across the nucleus in regulating hypertrophic genes remains to be determined, however, we can assume that any variation in nuclear Ca^{2+} dynamics due to variation in nucleus size is not enough

to disrupt the signal. As we saw in Figure 4.10, the variation in Ca^{2+} dynamics due to natural variation in the geometry of cardiac nuclei is far larger than the variation in Ca^{2+} dynamics across a single nucleus. Overall, a 1D approximation appears to be sufficient to model $[Ca^{2+}]$ within the nucleus for a large variety of situations.

Chapter 5

Conclusions

In this study, our aim has been to understand the complex mechanisms involved in the role of Ca^{2+} as a signalling molecule within the cardiac hypertrophic pathway. To this end, we have constructed a compartmental model of the effect of IP_3 on Ca^{2+} dynamics within the cardiac cytosol. This model allows us to quantify the potential changes to Ca^{2+} dynamics as a result of IP_3R activation during hypertrophy and demonstrate the feasibility of the duty cycle hypothesis proposed by Hannanta-anan and Chow (49).

Additionally, we have developed a model of $[Ca^{2+}]$ in the cardiac nucleus to better understand the downstream impact of altered cytosolic Ca^{2+} dynamics on the same pathway. This model explores the effects of the nuclear environment on Ca^{2+} diffusion, including nuclear Ca^{2+} buffers, and the effects of nucleus geometry. The construction of this model allows us to determine the effects of changes to cytosolic Ca^{2+} dynamics as well as the impact of perinuclear Ca^{2+} release on nuclear Ca^{2+} dynamics through adjustment of model boundary conditions. With this model, we have been able to replicate the temporal characteristics of nuclear $[Ca^{2+}]$ in experimental data. This model supports the hypothesis that non-ECC perinuclear Ca^{2+} release is affecting nuclear calcium within cardiomyocytes.

We have analytically solved a 3D, linear version of this model. The 3D model suggests that spatial variation in $[Ca^{2+}]$ within the nucleus may be relatively unimportant in gene regulatory signalling.

Overall, this work contributes to a better understanding of how the movement of Ca^{2+} is affected by the hypertrophic signal both within the cytosol and the nucleus and thereby how IP_3-dependent modification to cellular Ca^{2+} dynamics can convey the hypertrophic signal.

5.1 Advances made in this study

5.1.1 Our cytosolic [Ca^{2+}] model is able to reproduce experimental observations

Prior to this investigation, there existed a plethora of cardiac [Ca^{2+}] models and several experimental investigations into the gating of IP_3R channels in addition to models of IP_3R channels in cell types where they are the primary effectors of the Ca^{2+} signal. However, none explored the interactions between RyR and IP_3R channels in the cardiac cell. In particular, there were no models that described the altered cardiac Ca^{2+} dynamics that lead to hypertrophy.

The model we describe in Chapter 2 combines what is known about cardiac Ca^{2+} dynamics of healthy cells (the gating, dependencies, and interactions between channels that are necessary to generate the cardiac contraction signal) and IP_3R channels (their gating, and dependencies) into a coherent model of the alterations made to cytosolic cardiac Ca^{2+} dynamics to transmit the hypertrophic signal.

In doing so, we made several assumptions about the distribution and interactions of cardiac Ca^{2+} channels. These include that IP_3R channels are essentially uniformly distributed throughout the cytosol, as well as the assumption that IP_3R channels are located closely enough or on areas of the SR membrane such that they are almost immediately sensitive to recent drains of SR Ca^{2+} stores as well as the corresponding Ca^{2+} release in the cytosol.

Exploration of the parameter space of our model in Section 2.3 revealed that depending on the parameters chosen, activation of IP_3R channels could increase or decrease the Ca^{2+} transient amplitude. Similarly, IP_3R activation within our model was capable of increasing or decreasing transient resting [Ca^{2+}]. However, the FDHM of the simulated cardiac Ca^{2+} transient increased with IP_3R activation in all simulated cases but one. The exception to this occurred where IP_3R channels were activated with implausibly high flux at slower oscillations, i.e. 0.3 Hz. In this case, FDHM decreased. Finally, the transient duty cycle, as defined by Hannanta-anan and Chow (49) increased with IP_3R activation in all cases.

5.1.2 Our cytosolic [Ca^{2+}] model provides evidence for specific IP_3R gating behaviour

Comparing our model to alterations to the ECC transient in experimental literature, we were able to show that with these assumptions, IP_3R channels could not behave in the same manner as the IP_3R type I channel gating described in the Cao-Siekmann-Sneyd model (137). We were able to use experimental literature to further narrow down the range of parameters describing IP_3R type II gating in cardiac cells and found this range of physiologically plausible parameters to be consistent with experimental data.

5.1.3 Our cytosolic [Ca^{2+}] model supports the duty cycle hypothesis in the CnA/NFAT pathway

Hannanta-anan and Chow (49) proposed the hypothesis that Ca^{2+} duty cycle determines the proportion of NFAT4 dephosphorylation and, hence, the hypertrophic signal in the CnA/NFAT pathway. This was demonstrated through a series of experiments showing the effect of tightly controlled Ca^{2+} signals on NFAT-mediated gene regulation in HeLa cells. NFAT is highly conserved across species and cell lines. However, it was not clear from experimental evidence that the CnA/NFAT pathway had any effect on the duty cycle of the cardiac Ca^{2+} transient.

In our simulations, the duty cycle of the cardiac Ca^{2+} transient across the determined physiologically plausible range was greater than the cardiac Ca^{2+} transient in healthy cells. Hence, our model further substantiates the hypothesis that the cardiac hypertrophic signal is transmitted through an increase in cardiac [Ca^{2+}] duty cycle.

5.1.4 Our nuclear [Ca^{2+}] model is able to reproduce the temporal characteristics of experimental observations

Prior to this study, relatively little was known about the dynamics of Ca^{2+} in the nucleus, specifically what controls the movement of Ca^{2+} throughout the nucleus. It is believed that, beyond the NE, there are no Ca^{2+} channels within the nucleus. In Chapters 3 and 4, we compared the temporal features of the cytosolic and

nuclear transients of individual cardiomyocytes and built up a biophysical model based on the movement of Ca^{2+} observed in experimental data.

Comparing the temporal characteristics of cytosolic and nuclear Ca^{2+} dynamics within adult rat ventricular myocytes, we built up the model starting from a simple diffusion model. We determined that the temporal characteristics of the nuclear Ca^{2+} transient could be simulated from the cytosolic transient through the addition of perinuclear Ca^{2+} release and at least one nonlinear Ca^{2+} buffer within the nucleus.

5.1.5 Our nuclear [Ca^{2+}] model predicts the changes that will occur in nuclear Ca^{2+} dynamics in response to alterations to cytosolic Ca^{2+} dynamics.

Given any alteration to the [Ca^{2+}] at the NE, we can simulate the corresponding alterations to the [Ca^{2+}] within the nucleus by changing the boundary conditions of our model. Through this method, we were able to simulate the effects on nuclear Ca^{2+} dynamics of hypertrophic alterations to the cytosolic Ca^{2+} transient predicted in Chapter 2. We found that an increase in cytosolic Ca^{2+} transient amplitude or FDHM would have a corresponding increase in nuclear Ca^{2+} transient amplitude or FDHM. Any increase to cytosolic [Ca^{2+}] FDHM, would additionally increase nuclear [Ca^{2+}] amplitude.

5.1.6 Our nuclear [Ca^{2+}] model supports the hypothesis that there is perinuclear Ca^{2+} release during ECC

To replicate the temporal characteristics of the nuclear Ca^{2+} transients observed in the line-scan data in section 3.2, it was necessary to increase the FDHM of the boundary condition of our model. There remains the possibility that there is an important aspect of nuclear Ca^{2+} dynamics that we have failed to include in our model that could also replicate the effect of an increase in cytosolic FDHM. However, from our simulations in Chapter 2, an increase in FDHM of the Ca^{2+} transient between the bulk cytosol and the nucleus is an indication of Ca^{2+} release in the perinuclear region. The necessity of this change to replicate experimental data supports the existence of IP_3R-mediated Ca^{2+} release in or around the nucleus.

5.1.7 Our nuclear [Ca^{2+}] model demonstrates that a 1D diffusion model of Ca^{2+} is sufficient to determine the defining characteristics of the nuclear Ca^{2+} transient

Through an extension of our simple 1D diffusion model to 3D in Chapter 4, we simulated spatial [Ca^{2+}] variation throughout the three-dimensional nucleus. Simulating nuclei within one standard deviation of our measured average nuclear radius, we have shown that the variation in [Ca^{2+}] across the length of the nucleus is minor in comparison to the simulated variation in [Ca^{2+}] between nuclei of varying radius. This indicates that the variation in [Ca^{2+}] along the length of the nucleus has a negligible effect on the hypertrophic signal. However, it is possible that the variation in nuclear Ca^{2+} dynamics due to nuclear radius could explain some of the discrepancy in response to hypertrophic stimuli between cells.

5.2 Limitations of this study

5.2.1 The models do not fully describe the system

Necessarily, all models are approximations of reality. Despite the known, and potentially unknown, nuclear Ca^{2+} buffers, the model of nuclear [Ca^{2+}] considered only one buffer because of the limited amount of information we could glean from the data available to us. There are potentially dozens, if not more, Ca^{2+} buffers within the nucleus. Additionally, in creating the model we made several assumptions e.g. a uniform distribution of NPCs, isotropic diffusion, with limited data to support them.

We have also ignored irregularities in nuclear geometry and temporary nuclear invaginations that can form on the nuclear envelope and penetrate into the nucleus. These could potentially create even more spatial variation in the nuclear [Ca^{2+}] . Nuclear invaginations in particular could increase the speed at which any Ca^{2+} signal reaches the centre of the nucleus and counteract the slower Ca^{2+} diffusion in larger nuclei. Additionally, the presence of any of these nuclear invaginations could have skewed our results to indicate faster Ca^{2+} diffusion.

Another modelling assumption that could not be verified was the assumption that IP_3R channels are not located in the dyad with RyR and LTCC channels. Preliminary results from a variation of the model described in Chapter 2 indicate

that the effect of IP_3R channels on the Ca^{2+} transient would be lessened if not completely changed if they were located in the dyad. However, so far, published microscopy data has not been able to verify either distribution.

5.2.2 Our model predicts perinuclear Ca^{2+} release but does not explicitly model it

We predicted in Chapter 3 the effect of alterations to the cytosolic Ca^{2+} signal on the nuclear Ca^{2+} signal. However, our model has also predicted the existence of some form of perinuclear Ca^{2+} release that augments the cytosolic Ca^{2+} signal on its way to the nucleus. We have not examined the dependence of such a signal on $[Ca^{2+}]$ making any predictions based on cytosolic $[Ca^{2+}]$ less reliable. Given the likelihood that this perinuclear Ca^{2+} release is either $[Ca^{2+}]$ -induced, or relatively constant, we expect our predictions of the effects of cytosolic Ca^{2+} alterations to be qualitatively correct. However, modelling this potential perinuclear Ca^{2+} release and coupling it to our model is a promising avenue of future research.

5.3 Future research

5.3.1 Experimental verification of models

While many of the modelling decisions made in the course of this project were based on experimental results, and the models designed to mimic the output of experiments, we have not ourselves done any experiments. As such, we have not been able to verify for ourselves the results of this study. We must await the verdict of interested experimental biologists to see if our modelling assumptions and predictions play out. In particular: our prediction on the importance of $[IP_3]$ on the overall effect of IP_3R channel activation on the cytosolic Ca^{2+} transient, and our predictions of the changes to nuclear Ca^{2+} dynamics in response to cytosolic Ca^{2+} dynamics.

5.3.2 Coupling to NFAT/gene expression dynamics

In order to understand the complete CnA/NFAT hypertrophic pathway, it is necessary to couple these models to models of the pathways other components. The most obvious starting point would be a model of NFAT dephosphorylation

and translocation, as well as gene regulation in response to Ca^{2+} dynamics. This would give us a full picture of the CnA/NFAT pathway from Ca^{2+} signal to gene expression.

Coupling a model of IP_3 production/release in response to activation of the G-coupled receptor would also provide a more complete picture of this pathway. There is some evidence that IP_3 concentration oscillates within the cytosol with Ca^{2+} concentration (112). We have so far modelled only the effect of IP_3R activation when $[IP_3]$ is constant. The timing and amplitude of any potential IP_3 oscillations, as well as the timing of ET-1 or other external agonists that lead to IP_3 release, would give us new insight into cardiac Ca^{2+} channel interactions and the hypertrophic signal.

5.3.3 The roles of other IP_3R isoforms in cardiac cells

We have modelled only the effect of IP_3R type II channels on the cardiac Ca^{2+} transient. While these are the most numerous within cardiac cells, making up approximately 85% of IP_3R channels (78), and believed to be primarily responsible for any IP_3-mediated response, there is also a small proportion of type III IP_3R isoforms within cardiac myocytes. These are not as well studied as the more common type I and II isoforms but could have a role in IP_3-Ca^{2+} signalling. A better understanding of the gating properties of IP_3R type III isoforms and their distribution within cardiac myocytes is necessary to better understand their role within the cell.

5.3.4 The roles of other NFAT isoforms in cardiac cells

As with IP_3R channels, we focussed on only one isoform of NFAT. NFAT4 has been shown to be a necessary component in the CnA/NFAT pathway and is also the main isoform studied in the by Tomida et al. (149) and Hannanta-anan and Chow (49). Different NFAT isoforms can respond to different Ca^{2+} signals (65). Additionally, other NFAT isoforms may also play a crucial role in hypertrophy. Understanding the importance of the other NFAT isoforms in cardiac cells may result in us needing to understand their response to Ca^{2+} as well. In that case, our model of the potential changes to Ca^{2+} dynamics in response to hypertrophy will be essential.

5.3.5 The required nuclear signals for NFAT to remain dephosphorylated and enact gene expression

There are no detailed studies of the nuclear Ca^{2+} signal required to keep NFAT dephosphorylated in the nucleus so that it can activate the hypertrophic genes. In the experiments performed by Hannanta-anan and Chow (49), no further externally-stimulated Ca^{2+} release was required to see evidence of NFAT4-mediated gene expression. It is possible that this is true for NFAT4 in cardiomyocytes too. There is mixed evidence for whether separate, localised Ca^{2+} signals are required in cardiomyocytes or whether the modified ECC Ca^{2+} transient is sufficient (165, 174, 72, 40). Future experimental evidence may allow us to refine our model to account for other specific hypertrophic alterations to the Ca^{2+} transient.

5.3.6 Experimental evidence of the effect of $[IP_3]$ on the cardiac Ca^{2+} transient

A true test of any mathematical model lies in its ability to make predictions. One of the simplest experimental tests of our cytosolic Ca^{2+} model is to investigate the variation in effect of the cytosolic Ca^{2+} transient in cells stimulated with varying concentrations of IP_3. Access to data on the change in amplitude a change in $[IP_3]$ makes to the Ca^{2+} transient could verify some of our model predictions and potentially allow us to further pinpoint the true parameter values for IP_3R channels within our model.

5.3.7 Density and behaviour of perinuclear Ca^{2+} channels

We have only touched upon the effects of Ca^{2+} channels located on or around the NE, incorporating their effects into the potential boundary conditions of the nucleus as alterations to the cytosolic $[Ca^{2+}]$ that we know is also affecting the nucleus. This means that we can simulate the effect of any potential perinuclear Ca^{2+} release on nuclear Ca^{2+} dynamics however not much is known about the form that this release will take. An investigation into the composition of these perinuclear channels, their density, and what external factors may influence them would give us a more comprehensive understanding of the transition from cytosolic to nuclear Ca^{2+} dynamics.

5.4 Future applications of this research

In the long term, the existence of simple and reliable cardiac [Ca^{2+}] models may play an integral role in identifying both drug targets and contraindications within cardiomyocytes when combating hypertrophy and other cardiac issues. Models that combine simulations of Ca^{2+} release from each channel type as well as channel interactions allow us to better predict the effects, and side-effects, of drugs that interact with the cardiac Ca^{2+} machinery or adjacent cardiac mechanisms (154, 76). Once a new drug's biological target is identified, we can combine these models along with others describing the cardiac cell to determine both the immediate and follow on effects. Hypothetically, a complete model of the cardiac cell and downstream effects on both the heart and rest of the body would allow us to dramatically cut back on the need for clinical trials with bulk of a drug's effects determined through simulation.

While we are a long way from this goal, the potential time and lives saved in drug development and testing would be invaluable. Similarly, with the rise in personalised medicine, these would be amongst the many models that could be easily adjusted based on determinants of channel density to simulate the Ca^{2+} dynamics of an individual and determine a precise, customised treatment.

Bibliography

[1] Anderson, R.H. and Ho, S.Y. The Architecture of the Sinus Node, the Atrioventricular Conduction Axis, and the Internodal Atrial Myocardium. *Journal of Cardiovascular Electrophysiology*, 9(11):1233–1248, 1998. doi: 10.1111/j.1540-8167.1998.tb00097.x.

[2] Baksh, S. Expression of Calreticulin in Escherichia coli and Identification of Its Ca2' Binding Domains. *J Biological Chemistry*, 266(32):8, 1991.

[3] Bare, D.J. et al. Cardiac Type 2 Inositol 1,4,5-Trisphosphate Receptor: Interaction and modulation by calcium/calmodulin-dependent protein kinase II. *Journal of Biological Chemistry*, 280(16):15912–15920, 2005. doi: 10.1074/jbc.M414212200.

[4] Bass, G.T. *Decoding Calcium Signalling Crosstalk in Cardiac Hypertrophy.* PhD thesis, The University of Melbourne, 2017.

[5] Bazzazi, H. et al. Novel fluorescence resonance energy transfer-based reporter reveals differential calcineurin activation in neonatal and adult cardiomyocytes: FRET-based calcineurin sensors. *The Journal of Physiology*, 593(17):3865–3884, 2015. doi: 10.1113/JP270510.

[6] Berenji, K. et al. Does load-induced ventricular hypertrophy progress to systolic heart failure? *American Journal of Physiology-Heart and Circulatory Physiology*, 289(1):H8–H16, 2005. doi: 10.1152/ajpheart.01303.2004.

[7] Berridge, M.J. The AM and FM of calcium signalling. *Nature*, 386(6627): 759–760, 1997. doi: 10.1038/386759a0.

[8] Berridge, M.J. The Inositol Trisphosphate/Calcium Signaling Pathway in Health and Disease. *Physiological Reviews*, 96(4):1261–1296, 2016. doi: 10.1152/physrev.00006.2016.

[9] Bers, D.M. *Excitation-Contraction Coupling and Cardiac Contractile Force*. Developments in Cardiovascular Medicine. Kluwer Academic Publishers, Dordrecht, 1st edition, 1991.

[10] Bers, D.M. *Excitation-Contraction Coupling and Cardiac Contractile Force*, volume 237 of *Developments in Cardiovascular Medicine*. Springer Netherlands, Dordrecht, 2001.

[11] Bers, D.M. Cardiac excitation–contraction coupling. *Nature*, 415(6868): 198–205, 2002. doi: 10.1038/415198a.

[12] Bkaily, G., Avedanian, L. and Jacques, D. Nuclear membrane receptors and channels as targets for drug development in cardiovascular diseases. *Canadian Journal of Physiology and Pharmacology*, 87(2):108–119, 2009. doi: 10.1139/Y08-115.

[13] Blanch i Salvador, J. and Egger, M. Obstruction of ventricular Ca^{2+}-dependent arrhythmogenicity by inositol 1,4,5-trisphosphate-triggered sarcoplasmic reticulum Ca^{2+} release. *The Journal of Physiology*, 596(18):4323–4340, 2018. doi: 10.1113/JP276319.

[14] Bootman, M.D. et al. An update on nuclear calcium signalling. *J Cell Sci*, 122(Pt 14):2337–2350, 2009. doi: 10.1242/jcs.028100.

[15] Bourajjaj, M. et al. NFATc2 Is a Necessary Mediator of Calcineurin-dependent Cardiac Hypertrophy and Heart Failure. *Journal of Biological Chemistry*, 283(32):22295–22303, 2008. doi: 10.1074/jbc.M801296200.

[16] Brette, F., Sallé, L. and Orchard, C.H. Quantification of Calcium Entry at the T-Tubules and Surface Membrane in Rat Ventricular Myocytes. *Biophysical Journal*, 90(1):381–389, 2006. doi: 10.1529/biophysj.105.069013.

[17] Cao, P. et al. A Stochastic Model of Calcium Puffs Based on Single-Channel Data. *Biophysical Journal*, 105(5):1133–1142, 2013. doi: 10.1016/j.bpj.2013.07.034.

[18] Cao, P. et al. A Deterministic Model Predicts the Properties of Stochastic Calcium Oscillations in Airway Smooth Muscle Cells. *PLOS Computational Biology*, 10(8), 2014. doi: 10.1371/journal.pcbi.1003783.

[19] Chamero, P. Dampening of Cytosolic Ca^{2+} Oscillations on Propagation to Nucleus. *Journal of Biological Chemistry*, 277(52):50226–50229, 2002. doi: 10.1074/jbc.C200522200.

[20] Charlemagne, D. et al. Alteration of Na,K-ATPase subunit mRNA and protein levels in hypertrophied rat heart. *Journal of Biological Chemistry*, 269(2):1541–1547, 1994.

[21] Colella, M. et al. Ca^{2+} oscillation frequency decoding in cardiac cell hypertrophy: Role of calcineurin/NFAT as Ca^{2+} signal integrators. *Proceedings of the National Academy of Sciences*, 105(8):2859–2864, 2008. doi: 10.1073/pnas.0712316105.

[22] Colquhoun, D. and Hawkes, A.G. On the Stochastic Properties of Bursts of Single Ion Channel Openings and of Clusters of Bursts. *Philosophical Transactions of the Royal Society of London B: Biological Sciences*, 300 (1098):1–59, 1982. doi: 10.1098/rstb.1982.0156.

[23] Cooling, M., Hunter, P. and Crampin, E.J. Modeling Hypertrophic IP_3 Transients in the Cardiac Myocyte. *Biophysical Journal*, 93(10):3421–3433, 2007. doi: 10.1529/biophysj.107.110031.

[24] Cooling, M., Hunter, P. and Crampin, E. Modelling biological modularity with CellML. *IET Systems Biology*, 2(2):73–79, 2008. doi: 10.1049/iet-syb: 20070020.

[25] Cooling, M.T., Hunter, P. and Crampin, E.J. Sensitivity of NFAT Cycling to Cytosolic Calcium Concentration: Implications for Hypertrophic Signals in Cardiac Myocytes. *Biophysical Journal*, 96(6):2095–2104, 2009. doi: 10.1016/j.bpj.2008.11.064.

[26] Dobi, A. and v. Agoston, D. Submillimolar levels of calcium regulates DNA structure at the dinucleotide repeat (TG/AC)n. *Proceedings of the National Academy of Sciences*, 95(11):5981–5986, 1998. doi: 10.1073/pnas. 95.11.5981.

[27] Domeier, T.L. et al. IP_3 receptor-dependent Ca^{2+} release modulates excitation-contraction coupling in rabbit ventricular myocytes. *American Journal of Physiology - Heart and Circulatory Physiology*, 294(2):H596–H604, 2008. doi: 10.1152/ajpheart.01155.2007.

[28] Domínguez-Rodríguez, A. et al. The other side of cardiac Ca^{2+} signaling: Transcriptional control. *Frontiers in Physiology*, 3, 2012. doi: 10.3389/fphys.2012.00452.

[29] Dossetor, R.S. Renal compensatory hypertrophy in the adult. *The British Journal of Radiology*, 48(576):993–995, 1975. doi: 10.1259/0007-1285-48-576-993.

[30] Escobar, A.L. et al. Role of inositol 1, 4, 5-trisphosphate in the regulation of ventricular Ca^{2+} signaling in intact mouse heart. *Journal of molecular and cellular cardiology*, 53(6):768–779, 2012. doi: 10.1016/j.yjmcc.2012.08.019.

[31] Fabiato, A. Calcium-induced release of calcium from the cardiac sarcoplasmic reticulum. *American Journal of Physiology-Cell Physiology*, 245(1): C1–C14, 1983. doi: 10.1152/ajpcell.1983.245.1.C1.

[32] Fabiato, A. Time and calcium dependence of activation and inactivation of calcium-induced release of calcium from the sarcoplasmic reticulum of a skinned canine cardiac Purkinje cell. *The Journal of General Physiology*, 85(2):247–289, 1985. doi: 10.1085/jgp.85.2.247.

[33] Falcke, M. Buffers and Oscillations in Intracellular Ca^{2+} Dynamics. *Biophysical Journal*, 84(1):28–41, 2003. doi: 10.1016/S0006-3495(03)74830-9.

[34] Falcke, M. On the Role of Stochastic Channel Behavior in Intracellular Ca^{2+} Dynamics. *Biophysical Journal*, 84(1):42–56, 2003. doi: 10.1016/S0006-3495(03)74831-0.

[35] Faustino, R.S. et al. Calreticulin secures calcium-dependent nuclear pore competency required for cardiogenesis. *Journal of Molecular and Cellular Cardiology*, 92:63–74, 2016. doi: 10.1016/j.yjmcc.2016.01.022.

[36] Fawcett, D.W. The Ultrastructure of the Cat Myocardium: I. Ventricular Papillary Muscle. *The Journal of Cell Biology*, 42(1):1–45, 1969. doi: 10.1083/jcb.42.1.1.

[37] Finch, E.A., Turner, T.J. and Goldin, S.M. Calcium as a coagonist of inositol 1,4,5-trisphosphate-induced calcium release. *Science*, 252(5004): 443–446, 1991. doi: 10.1126/science.2017683.

[38] Foskett, J.K. et al. Inositol Trisphosphate Receptor Ca^{2+} Release Channels. *Physiological Reviews*, 87(2):593–658, 2007. doi: 10.1152/physrev.00035.2006.

[39] Fox, J.L., Burgstahler, A.D. and Nathanson, M.H. Mechanism of long-range Ca 2 + signalling in the nucleus of isolated rat hepatocytes. *Biochem. J*, 326(2):491–495, 1997. doi: 10.1042/bj3260491.

[40] Garcia, M.I. and Boehning, D. Cardiac inositol 1,4,5-trisphosphate receptors. *Biochimica et Biophysica Acta (BBA) - Molecular Cell Research*, 1864 (6):907–914, 2017. doi: 10.1016/j.bbamcr.2016.11.017.

[41] Gaur, N. and Rudy, Y. Multiscale Modeling of Calcium Cycling in Cardiac Ventricular Myocyte: Macroscopic Consequences of Microscopic Dyadic Function. *Biophysical Journal*, 100(12):2904–2912, 2011. doi: 10.1016/j.bpj.2011.05.031.

[42] Genka, C. et al. Visualization of biphasic Ca^{2+}diffusion from cytosol to nucleus in contracting adult rat cardiac myocytes with an ultra-fast confocal imaging system. *Cell Calcium*, 25(3):199–208, 1999. doi: 10.1054/ceca.1999.0026.

[43] Gerasimenko, O.V. et al. Calcium transport pathways in the nucleus. *Pflugers Arch*, 432(1):1–6, 1996.

[44] Gilchrist, J.S.C., Czubryt, M.P. and Pierce, G.N. Calcium and calcium-binding proteins in the nucleus. *Molecular and Cellular Biochemistry*, 135 (1):79–88, 1994. doi: 10.1007/BF00925963.

[45] Grant, R.P. Notes on the Muscular Architecture of the Left Ventricle. *Circulation*, 32(2):301–308, 1965. doi: 10.1161/01.CIR.32.2.301.

[46] Greenstein, J.L. and Winslow, R.L. An integrative model of the cardiac ventricular myocyte incorporating local control of Ca^{2+} release. *Biophysical Journal*, 83(6):2918–2945, 2002. doi: 10.1016/S0006-3495(02)75301-0.

[47] Guatimosim, S. et al. Nuclear Ca^{2+} regulates cardiomyocyte function. *Cell Calcium*, 44(2):230–242, 2008. doi: 10.1016/j.ceca.2007.11.016.

[48] Hall, A.P. et al. Liver Hypertrophy: A Review of Adaptive (Adverse and Non-adverse) Changes—Conclusions from the 3rd International ESTP Expert Workshop. *Toxicologic Pathology*, 40(7):971–994, 2012. doi: 10.1177/0192623312448935.

[49] Hannanta-anan, P. and Chow, B.Y. Optogenetic Control of Calcium Oscillation Waveform Defines NFAT as an Integrator of Calcium Load. *Cell Systems*, 2(4):283–288, 2016. doi: 10.1016/j.cels.2016.03.010.

[50] Harzheim, D. et al. Increased InsP3Rs in the junctional sarcoplasmic reticulum augment Ca^{2+} transients and arrhythmias associated with cardiac hypertrophy. *Proceedings of the National Academy of Sciences of the United States of America*, 106(27):11406–11411, 2009. doi: 10.1073/pnas.0905485106.

[51] Heineke, J. and Molkentin, J.D. Regulation of cardiac hypertrophy by intracellular signalling pathways. *Nature Reviews Molecular Cell Biology*, 7(8):589–600, 2006. doi: 10.1038/nrm1983.

[52] Heinzel, F.R. et al. Dyssynchrony of Ca^{2+} release from the sarcoplasmic reticulum as subcellular mechanism of cardiac contractile dysfunction. *Journal of Molecular and Cellular Cardiology*, 50(3):390–400, 2011. doi: 10.1016/j.yjmcc.2010.11.008.

[53] Higazi, D.R. et al. Endothelin-1-Stimulated InsP3-Induced Ca^{2+} Release Is a Nexus for Hypertrophic Signaling in Cardiac Myocytes. *Molecular Cell*, 33(4):472–482, 2009. doi: 10.1016/j.molcel.2009.02.005.

[54] Hinch, R. A Mathematical Analysis of the Generation and Termination of Calcium Sparks. *Biophysical Journal*, 86(3):1293–1307, 2004. doi: 10.1016/S0006-3495(04)74203-4.

[55] Hinch, R. et al. A Simplified Local Control Model of Calcium-Induced Calcium Release in Cardiac Ventricular Myocytes. *Biophysical Journal*, 87 (December):24–29, 2004. doi: 10.1529/biophysj.104.049973.

[56] Hohendanner, F. et al. Calcium and IP_3 dynamics in cardiac myocytes: Experimental and computational perspectives and approaches. *Frontiers in Pharmacology*, 5(35):1–10, 2014. doi: 10.3389/fphar.2014.00035.

[57] Hohendanner, F., Maxwell, J.T. and Blatter, L.A. Cytosolic and nuclear calcium signaling in atrial myocytes: IP_3-mediated calcium release and the role of mitochondria. *Channels*, 9(3):129–138, 2015. doi: 10.1080/19336950.2015.1040966.

[58] Hunt, H. et al. IP_3R Ca^{2+} release shapes the cytosolic Ca^{2+} transient for hypertrophic signalling in cardiomyocytes. *arXiv:1902.04851 [q-bio]*, 2020.

[59] Hussain, A. et al. An Automated Workflow for Segmenting Single Adult Cardiac Cells from Large-Volume Serial Block-Face Scanning Electron Microscopy Data. *Journal of Structural Biology*, 202(3):275–285, 2018. doi: 10.1101/242701.

[60] Ionescu, L. et al. Mode Switching Is the Major Mechanism of Ligand Regulation of InsP3 Receptor Calcium Release Channels. *The Journal of General Physiology*, 130(6):631–645, 2007. doi: 10.1085/jgp.200709859.

[61] Jaffe, L.F. The path of calcium in cytosolic calcium oscillations: A unifying hypothesis. *Proceedings of the National Academy of Sciences of the United States of America*, 88(21):9883–9887, 1991. doi: 10.1073/pnas.88.21.9883.

[62] Jansen, M.J.W. Analysis of variance designs for model output. *Computer Physics Communications*, 117(1):35–43, 1999. doi: 10.1016/S0010-4655(98)00154-4.

[63] Johny, J.P., Plank, M.J. and David, T. Importance of Altered Levels of SERCA, IP_3R, and RyR in Vascular Smooth Muscle Cell. *Biophysical Journal*, 112(2):265–287, 2017. doi: 10.1016/j.bpj.2016.11.3206.

[64] Kar, P. and Parekh, A.B. Distinct Spatial Ca^{2+} Signatures Selectively Activate Different NFAT Transcription Factor Isoforms. *Molecular Cell*, 58(2):232–243, 2015. doi: 10.1016/j.molcel.2015.02.027.

[65] Kar, P. et al. Control of NFAT Isoform Activation and NFAT-Dependent Gene Expression through Two Coincident and Spatially Segregated Intracellular Ca^{2+} Signals. *Molecular Cell*, 64(4):746–759, 2016. doi: 10.1016/j.molcel.2016.11.011.

[66] Katz, A.M. Congestive Heart Failure. *New England Journal of Medicine*, 293(23):1184–1191, 1975. doi: 10.1056/NEJM197512042932309.

[67] Katz, A.M. *Physiology of the Heart*. Lippincott Williams & Wilkins, 2010.

[68] Kawai, M., Hussain, M. and Orchard, C.H. Excitation-contraction coupling in rat ventricular myocytes after formamide-induced detubulation. *The American Journal of Physiology*, 277(2):H603–609, 1999. doi: 10.1152/ajpheart.1999.277.2.H603.

[69] Keener, J.P. and Sneyd, J. *Mathematical Physiology*. Number 8 in Interdisciplinary Applied Mathematics. Springer, New York, NY, 2nd ed edition, 2009.

[70] Keminer, O. and Peters, R. Permeability of Single Nuclear Pores. *Biophysical Journal*, 77(1):217–228, 1999. doi: 10.1016/S0006-3495(99)76883-9.

[71] Kiess, T.O. and Kockskämper, J. SERCA Activity Controls the Systolic Calcium Increase in the Nucleus of Cardiac Myocytes. *Frontiers in Physiology*, 10, 2019. doi: 10.3389/fphys.2019.00056.

[72] Kockskämper, J. et al. Endothelin-1 enhances nuclear Ca^{2+} transients in atrial myocytes through Ins(1,4,5)P3-dependent Ca^{2+} release from perinuclear Ca^{2+} stores. *Journal of Cell Science*, 121(2):186–195, 2008. doi: 10.1242/jcs.021386.

[73] Korolev, N. et al. Competitive Binding of Mg2+, Ca2+, Na+, and K+ Ions to DNA in Oriented DNA Fibers: Experimental and Monte Carlo Simulation Results. *Biophysical Journal*, 77(5):2736–2749, 1999. doi: 10.1016/S0006-3495(99)77107-9.

[74] Kushmerick, M.J. and Podolsky, R.J. Ionic Mobility in Muscle Cells. *Science*, 166(3910):1297–1298, 1969. doi: 10.1126/science.166.3910.1297.

[75] Ladd, D. et al. Assessing Cardiomyocyte Excitation-Contraction Coupling Site Detection From Live Cell Imaging Using a Structurally-Realistic Computational Model of Calcium Release. *Frontiers in Physiology*, 10, 2019. doi: 10.3389/fphys.2019.01263.

[76] Li, Z. et al. General Principles for the Validation of Proarrhythmia Risk Prediction Models: An Extension of the CiPA In Silico Strategy. *Clinical Pharmacology & Therapeutics*, 107(1):102–111, 2020. doi: 10.1002/cpt.1647.

[77] Lipp, P. et al. Nuclear calcium signalling by individual cytoplasmic calcium puffs. *The EMBO Journal*, 16(23):7166–7173, 1997. doi: 10.1093/emboj/16.23.7166.

[78] Lipp, P. et al. Functional InsP3 receptors that may modulate excitation–contraction coupling in the heart. *Current Biology*, 10(15):939–S1, 2000. doi: 10.1016/S0960-9822(00)00624-2.

[79] Liu, Y., Randall, W.R. and Schneider, M.F. Activity-dependent and -independent nuclear fluxes of HDAC4 mediated by different kinases in adult skeletal muscle. *The Journal of Cell Biology*, 168(6):887–897, 2005. doi: 10.1083/jcb.200408128.

[80] Ljubojevic, S. et al. In situ calibration of nucleoplasmic versus cytoplasmic Ca 2+ concentration in adult cardiomyocytes. *Biophysical Journal*, 100 (10):2356–2366, 2011. doi: 10.1016/j.bpj.2011.03.060.

[81] Lorell, B.H. and Carabello, B.A. Left Ventricular Hypertrophy. *Circulation*, 102(4):470–479, 2000. doi: 10.1161/01.CIR.102.4.470.

[82] Louch, W.E. et al. Control of Ca^{2+} Release by Action Potential Configuration in Normal and Failing Murine Cardiomyocytes. *Biophysical Journal*, 99(5):1377–1386, 2010. doi: 10.1016/j.bpj.2010.06.055.

[83] Lu, X. et al. Intrafibrillar and perinuclear mitochondrial heterogeneity in adult cardiac myocytes. *Journal of Molecular and Cellular Cardiology*, 136: 72–84, 2019. doi: 10.1016/j.yjmcc.2019.08.013.

[84] Luby-Phelps, K. Behavior of a fluorescent analogue of calmodulin in living 3T3 cells. *The Journal of Cell Biology*, 101(4):1245–1256, 1985. doi: 10.1083/jcb.101.4.1245.

[85] Lukyanenko, V., Chikando, A. and Lederer, W.J. Mitochondria in cardiomyocyte Ca^{2+} signaling. *The International Journal of Biochemistry & Cell Biology*, 41(10):1957–1971, 2009. doi: 10.1016/j.biocel.2009.03.011.

[86] Lynch, J. et al. Calreticulin signals upstream of calcineurin and MEF2C in a critical Ca $^{2+}$ -dependent signaling cascade. *The Journal of Cell Biology*, 170(1):37–47, 2005. doi: 10.1083/jcb.200412156.

[87] Mackenzie, L. et al. The role of inositol 1,4,5-trisphosphate receptors in Ca^{2+} signalling and the generation of arrhythmias in rat atrial myocytes. *The Journal of Physiology*, 541(Pt 2):395–409, 2002. doi: 10.1113/jphysiol.2001.013411.

[88] Mackiewicz, U. and Lewartowski, B. Temperature dependent contribution of Ca^{2+} transporters to relaxation in cardiac myocytes: Important role of sarcolemmal Ca^{2+}-ATPase. *Journal of Physiology and Pharmacology: An Official Journal of the Polish Physiological Society*, 57(1):3–15, 2006.

[89] Mattaj, I.W. and Englmeier, L. NUCLEOCYTOPLASMIC TRANSPORT: The Soluble Phase. *Annual Review of Biochemistry*, 67(1):265–306, 1998. doi: 10.1146/annurev.biochem.67.1.265.

[90] Mauger, J.P. Role of the nuclear envelope in calcium signalling. *Biology of the Cell*, 104(2):70–83, 2011. doi: 10.1111/boc.201100103.

[91] McKinsey, T.A. et al. Signal-dependent nuclear export of a histone deacetylase regulates muscle differentiation. *Nature*, 408(6808):106, 2000. doi: 10.1038/35040593.

[92] McKinsey, T.A., Zhang, C.L. and Olson, E.N. MEF2: A calcium-dependent regulator of cell division, differentiation and death. *Trends in Biochemical Sciences*, 27(1):40–47, 2002. doi: 10.1016/S0968-0004(01)02031-X.

[93] Means, S. et al. Reaction Diffusion Modeling of Calcium Dynamics with Realistic ER Geometry. *Biophysical Journal*, 91(2):537–557, 2006. doi: 10.1529/biophysj.105.075036.

[94] Mihl, C., Dassen, W. and Kuipers, H. Cardiac remodelling: Concentric versus eccentric hypertrophy in strength and endurance athletes. *Netherlands Heart Journal*, 16(4):129–133, 2008.

[95] Minamikawa, T., Takahashi, A. and Fujita, S. Differences in features of calcium transients between the nucleus and the cytosol in cultured heart muscle cells: Analyzed by confocal microscopy. *Cell Calcium*, 17(3):165–176, 1995. doi: 10.1016/0143-4160(95)90031-4.

[96] Mohler, P.J. et al. Ankyrin-B mutation causes type 4 long-QT cardiac arrhythmia and sudden cardiac death. *Nature*, 421(6923):634–639, 2003. doi: 10.1038/nature01335.

[97] Mohler, P.J., Davis, J.Q. and Bennett, V. Ankyrin-B Coordinates the Na/K ATPase, Na/Ca Exchanger, and InsP3 Receptor in a Cardiac T-Tubule/SR Microdomain. *PLOS Biology*, 3(12):e423, 2005. doi: 10.1371/journal.pbio.0030423.

[98] Molkentin, J.D. et al. A Calcineurin-Dependent Transcriptional Pathway for Cardiac Hypertrophy. *Cell*, 93(2):215–228, 1998. doi: 10.1016/S0092-8674(00)81573-1.

[99] Moraru, I.I. et al. Regulation of Type 1 Inositol 1,4,5-Trisphosphate–gated Calcium Channels by InsP3 and Calcium. *The Journal of General Physiology*, 113(6):837–849, 1999. doi: 10.1085/jgp.113.6.837.

[100] Moravec, C.S. et al. Endothelin is a positive inotropic agent in human and rat heart in, vitro. *Biochemical and Biophysical Research Communications*, 159(1):14–18, 1989. doi: 10.1016/0006-291X(89)92397-8.

[101] Moschella, M. and Marks, A. Inositol 1,4,5-trisphosphate receptor expression in cardiac myocytes. *The Journal of Cell Biology*, 120(5):1137–1146, 1993. doi: 10.1083/jcb.120.5.1137.

[102] Myers, G.E. Analytical methods in conduction heat transfer. Technical report, McGraw-Hill Book Company, New York, 1971.

[103] Nakanishi, H. et al. Sarcolemmal Ca^{2+} transport activities in cardiac hypertrophy caused by pressure overload. *American Journal of Physiology-Heart and Circulatory Physiology*, 257(2):H349–H356, 1989. doi: 10.1152/ajpheart.1989.257.2.H349.

[104] Nakayama, H. et al. The IP_3 Receptor Regulates Cardiac Hypertrophy in Response to Select Stimuli. *Circulation research*, 107(5):659–666, 2010. doi: 10.1161/CIRCRESAHA.110.220038.

[105] Namekata, I. et al. Propagation of Normal and Abnormal Cytoplasmic Ca^{2+} Oscillation into the Cell Nucleus in Cardiomyocytes. *bioimages*, 12 (2+3+4):61–69, 2004. doi: 10.11169/bioimages.12.61.

[106] Nicotera, P., Zhivotovsky, B. and Orrenius, S. Nuclear calcium transport and the role of calcium in apoptosis. *Cell Calcium*, 16(4):279–288, 1994. doi: 10.1016/0143-4160(94)90091-4.

[107] Olson, E.N. Sizing up the heart: Development redux in disease. *Genes & Development*, 17(16):1937–1956, 2003. doi: 10.1101/gad.1110103.

[108] Oosthoek, P.W. et al. Immunohistochemical delineation of the conduction system. II: The atrioventricular node and Purkinje fibers. *Circulation Research*, 73(3):482–491, 1993. doi: 10.1161/01.RES.73.3.482.

[109] Page, E. Quantitative ultrastructural analysis in cardiac membrane physiology. *American Journal of Physiology-Cell Physiology*, 235(5):C147–C158, 1978. doi: 10.1152/ajpcell.1978.235.5.C147.

[110] Pandit, S.V. et al. A Mathematical Model of Action Potential Heterogeneity in Adult Rat Left Ventricular Myocytes. *Biophysical Journal*, 81(6):3029–3051, 2001. doi: 10.1016/S0006-3495(01)75943-7.

[111] Perez-Terzic Carmen et al. Structural Plasticity of the Cardiac Nuclear Pore Complex in Response to Regulators of Nuclear Import. *Circulation Research*, 84(11):1292–1301, 1999. doi: 10.1161/01.RES.84.11.1292.

[112] Politi, A. et al. Models of IP_3 and Ca^{2+} Oscillations: Frequency Encoding and Identification of Underlying Feedbacks. *Biophysical Journal*, 90(9):3120–3133, 2006. doi: 10.1529/biophysj.105.072249.

[113] Proven, A. et al. Inositol 1,4,5-trisphosphate supports the arrhythmogenic action of endothelin-1 on ventricular cardiac myocytes. *Journal of Cell Science*, 119(16):3363–3375, 2006. doi: 10.1242/jcs.03073.

[114] Pusl, T. et al. Epidermal Growth Factor-mediated Activation of the ETS Domain Transcription Factor Elk-1 Requires Nuclear Calcium. *Journal of Biological Chemistry*, 277(30):27517–27527, 2002. doi: 10.1074/jbc.M203002200.

[115] Rajagopal, V. et al. Examination of the Effects of Heterogeneous Organization of RyR Clusters, Myofibrils and Mitochondria on Ca^{2+}Release Patterns in Cardiomyocytes. *PLoS Computational Biology*, 11(9):e1004417, 2015. doi: 10.1371/journal.pcbi.1004417.

[116] Ramos-Franco, J., Fill, M. and Mignery, G.A. Isoform-specific function of single inositol 1,4,5-trisphosphate receptor channels. *Biophysical Journal*, 75(2):834–839, 1998. doi: 10.1016/S0006-3495(98)77572-1.

[117] Rinne, A. et al. Isoform- and tissue-specific regulation of the Ca(2+)-sensitive transcription factor NFAT in cardiac myocytes and heart failure. *American Journal of Physiology. Heart and Circulatory Physiology*, 298(6): H2001–2009, 2010. doi: 10.1152/ajpheart.01072.2009.

[118] Roderick, H.L. et al. Calcium in the heart: When it's good, it's very very good, but when it's bad, it's horrid. *Biochemical Society Transactions*, 35 (Pt 5):957–961, 2007. doi: 10.1042/BST0350957.

[119] Rüdiger, S. Stochastic models of intracellular calcium signals. *Physics Reports*, 534(2):39–87, 2014. doi: 10.1016/j.physrep.2013.09.002.

[120] Ryall, K. et al. Network reconstruction and systems analysis of cardiac myocyte hypertrophy signaling. *The Journal of Biological Chemistry*, 287 (50):42259–42268, 2012. doi: 10.1074/jbc.M112.382937.

[121] Salazar, C., Politi, A.Z. and Höfer, T. Decoding of Calcium Oscillations by Phosphorylation Cycles: Analytic Results. *Biophysical Journal*, 94(4): 1203–1215, 2008. doi: 10.1529/biophysj.107.113084.

[122] Saltelli, A. et al. Variance based sensitivity analysis of model output. Design and estimator for the total sensitivity index. *Computer Physics Communications*, 181(2):259–270, 2010. doi: 10.1016/j.cpc.2009.09.018.

[123] Sarma, A. and Yang, W. Calcium regulation of nucleocytoplasmic transport. *Protein & Cell*, 2(4):291–302, 2011. doi: 10.1007/s13238-011-1038-x.

[124] Saucerman, J.J. and Bers, D.M. Calmodulin mediates differential sensitivity of CaMKII and calcineurin to local Ca^{2+} in cardiac myocytes. *Biophysical Journal*, 95(10):4597–4612, 2008. doi: 10.1529/biophysj.108.128728.

[125] Schlenstedt, G. and Solsbacher, J. Transport between the cytoplasm and the nucleus. *Protoplasma*, 209(3-4):166–172, 1999. doi: 10.1007/BF01453445.

[126] Shannon, T.R. et al. A mathematical treatment of integrated Ca dynamics within the ventricular myocyte. *Biophys. J*, 87(November):3351–3371, 2004. doi: 10.1529/biophysj.104.047449.

[127] Shannon, T.R., Wang, F. and Bers, D.M. Regulation of Cardiac Sarcoplasmic Reticulum Ca Release by Luminal [Ca] and Altered Gating Assessed with a Mathematical Model. *Biophysical Journal*, 89(6):4096–4110, 2005. doi: 10.1529/biophysj.105.068734.

[128] Shibasaki, F. et al. Role of kinases and the phosphatase calcineurin in the nuclear shuttling of transcription factor NF-AT4. *Nature*, 382(6589): 370–373, 1996. doi: 10.1038/382370a0.

[129] Shimizu, I. and Minamino, T. Physiological and pathological cardiac hypertrophy. *Journal of Molecular and Cellular Cardiology*, 97:245–262, 2016. doi: 10.1016/j.yjmcc.2016.06.001.

[130] Shuai, J. and Parker, I. Optical single-channel recording by imaging Ca^{2+} flux through individual ion channels: Theoretical considerations and limits to resolution. *Cell Calcium*, 37(4):283–299, 2005. doi: 10.1016/j.ceca.2004.10.008.

[131] Shuai, J.W. and Jung, P. Optimal ion channel clustering for intracellular calcium signaling. *Proceedings of the National Academy of Sciences*, 100 (2):506–510, 2003. doi: 10.1073/pnas.0236032100.

[132] Shuai, J.W. and Jung, P. Selection of intracellular calcium patterns in a model with clustered Ca 2 + release channels. *Physical Review E*, 67(3), 2003. doi: 10.1103/PhysRevE.67.031905.

[133] Siekmann, I. et al. A kinetic model for type I and II IP_3R accounting for mode changes. *Biophysical Journal*, 103(4):658–668, 2012. doi: 10.1016/j.bpj.2012.07.016.

[134] Siekmann, I., Sneyd, J. and Crampin, E.J. Statistical analysis of modal gating in ion channels. *Proceedings of the Royal Society A: Mathematical, Physical and Engineering Sciences*, 470(2166):20140030–20140030, 2014. doi: 10.1098/rspa.2014.0030.

[135] Siekmann, I. et al. Data-driven modelling of the inositol trisphosphate receptor (IPR) and its role in calcium induced calcium release (CICR). In *Computational Glioscience*, Springer Series in Computational Neuroscience. Springer, 1st edition, 2019.

[136] Signore, S. et al. Inositol 1, 4, 5-Trisphosphate Receptors and Human Left Ventricular MyocytesClinical Perspective. *Circulation*, 128(12):1286–1297, 2013. doi: 10.1161/CIRCULATIONAHA.113.002764.

[137] Sneyd, J. et al. On the dynamical structure of calcium oscillations. *Proceedings of the National Academy of Sciences*, 114(7):1456–1461, 2017. doi: 10.1073/pnas.1614613114.

[138] Sobie, E.A. et al. Termination of Cardiac Ca^{2+} Sparks : An Investigative Mathematical Model of Calcium-Induced Calcium Release. *Biophysical Journal*, 83(1):59–78, 2002. doi: 10.1016/S0006-3495(02)75149-7.

[139] Sparrow, A.J. et al. Measurement of Myofilament-Localised Calcium Dynamics in Adult Cardiomyocytes and the Effect of Hypertrophic Cardiomyopathy Mutations. *Circulation Research*, 2019. doi: 10.1161/CIRCRESAHA.118.314600.

[140] Stern, M.D. Theory of excitation-contraction coupling in cardiac muscle. *Biophys. J*, 63(2):497–517, 1992. doi: 10.1016/S0006-3495(92)81615-6.

[141] Stern, M.D. et al. Local Control Models of Cardiac Excitation–Contraction Coupling. *The Journal of General Physiology*, 113(3):469–489, 1999. doi: 10.1085/jgp.113.3.469.

[142] Streeter, D.D. et al. Fiber Orientation in the Canine Left Ventricle during Diastole and Systole. *Circulation Research*, 24(3):339–347, 1969. doi: 10.1161/01.RES.24.3.339.

[143] Swaminathan, D., Ullah, G. and Jung, P. A simple sequential-binding model for calcium puffs. *Chaos: An Interdisciplinary Journal of Nonlinear Science*, 19(3):037109, 2009. doi: 10.1063/1.3152227.

[144] Swietach, P., Spitzer, K.W. and Vaughan-Jones, R.D. Ca^{2+}-Mobility in the Sarcoplasmic Reticulum of Ventricular Myocytes Is Low. *Biophysical Journal*, 95(3):1412–1427, 2008. doi: 10.1529/biophysj.108.130385.

[145] Swillens, S. et al. Stochastic simulation of a single inositol 1,4,5-trisphosphatemsensitive Ca^{2+} channel reveals repetitive openings during 'blip-like' Ca^{2+} transients. *Cell Calcium*, 23(5):291–302, 1998. doi: 10.1016/S0143-4160(98)90025-2.

[146] Swillens, S. et al. From calcium blips to calcium puffs: Theoretical analysis of the requirements for interchannel communication. *Proceedings of the National Academy of Sciences*, 96(24):13750–13755, 1999. doi: 10.1073/pnas.96.24.13750.

[147] Terkildsen, J.R. et al. Using Physiome standards to couple cellular functions for rat cardiac excitation–contraction. *Experimental Physiology*, 93(7):919–929, 2008. doi: 10.1113/expphysiol.2007.041871.

[148] Thomas, D. et al. A comparison of fluorescent Ca^{2+}indicator properties and their use in measuring elementary and global Ca^{2+}signals. *Cell Calcium*, 28(4):213–223, 2000. doi: 10.1054/ceca.2000.0152.

[149] Tomida, T. et al. NFAT functions as a working memory of Ca^{2+} signals in decoding Ca^{2+} oscillation. *The EMBO journal*, 22(15):3825–3832, 2003. doi: 10.1093/emboj/cdg381.

[150] Tracy, R.E. and Sander, G.E. Histologically Measured Cardiomyocyte Hypertrophy Correlates with Body Height as Strongly as with Body Mass Index. *Cardiology Research and Practice*, 2011, 2011. doi: 10.4061/2011/658958.

[151] Ullah, G. et al. Multi-Scale Data-Driven Modeling and Observation of Calcium Puffs. *Cell calcium*, 52(2):152–160, 2012. doi: 10.1016/j.ceca.2012.04.018.

[152] van Rooij, E. et al. Requirement of Nuclear Factor of Activated T-cells in Calcineurin-mediated Cardiomyocyte Hypertrophy. *Journal of Biological Chemistry*, 277(50):48617–48626, 2002. doi: 10.1074/jbc.M206532200.

[153] Verheijck, E.E. et al. Pacemaker Synchronization of Electrically Coupled Rabbit Sinoatrial Node Cells. *The Journal of General Physiology*, 111(1):95–112, 1998. doi: 10.1085/jgp.111.1.95.

[154] Vicente, J. et al. Mechanistic Model-Informed Proarrhythmic Risk Assessment of Drugs: Review of the "CiPA" Initiative and Design of a Prospective Clinical Validation Study. *Clinical Pharmacology & Therapeutics*, 103(1): 54–66, 2018. doi: 10.1002/cpt.896.

[155] Wagner, J. and Keizer, J. Effects of Rapid Buffers on Ca^{2+} Diffusion and Ca^{2+} Oscillations. *Biophysical Journal*, 67:447–456, 1994. doi: 10.1016/S0006-3495(94)80500-4.

[156] Wang, H. and Clapham, D.E. Conformational changes of the in situ nuclear pore complex. *Biophysical journal*, 77(1):241–7, 1999. doi: 10.1016/S0006-3495(99)76885-2.

[157] Wilkins, B.J. and Molkentin, J.D. Calcium–calcineurin signaling in the regulation of cardiac hypertrophy. *Biochemical and Biophysical Research Communications*, 322(4):1178–1191, 2004. doi: 10.1016/j.bbrc.2004.07.121.

[158] Wilkins, B.J. et al. Targeted Disruption of NFATc3, but Not NFATc4, Reveals an Intrinsic Defect in Calcineurin-Mediated Cardiac Hypertrophic Growth. *Molecular and Cellular Biology*, 22(21):7603–7613, 2002. doi: 10.1128/MCB.22.21.7603-7613.2002.

[159] Wilkins, B.J. et al. Calcineurin/NFAT Coupling Participates in Pathological, but not Physiological, Cardiac Hypertrophy. *Circulation Research*, 94 (1):110–118, 2004. doi: 10.1161/01.RES.0000109415.17511.18.

[160] Wiltgen, S.M., Smith, I.F. and Parker, I. Superresolution Localization of Single Functional IP_3R Channels Utilizing Ca^{2+} Flux as a Readout. *Biophysical Journal*, 99(2):437–446, 2010. doi: 10.1016/j.bpj.2010.04.037.

[161] Winslow, R.L., Walker, M.A. and Greenstein, J.L. Modeling calcium regulation of contraction, energetics, signaling, and transcription in the cardiac myocyte. *Wiley Interdisciplinary Reviews: Systems Biology and Medicine*, 8(1):37–67, 2016. doi: 10.1002/wsbm.1322.

[162] World Health Organization. *World Health Statistics 2018: Monitoring Health for the SDGs : Sustainable Development Goals.* World Health Organization, 2018. OCLC: 1043859485.

[163] Wu, X. Sarcoplasmic Reticulum and Nuclear Envelope Are One Highly Interconnected Ca^{2+} Store Throughout Cardiac Myocyte. *Circulation Research*, 99(3):283–291, 2006. doi: 10.1161/01.RES.0000233386.02708.72.

[164] Wu, X. and Bers, D.M. Free and bound intracellular calmodulin measurements in cardiac myocytes. *Cell calcium*, 41(4):353–64, 2007. doi: 10.1016/j.ceca.2006.07.011.

[165] Wu, X. et al. Local InsP3-dependent perinuclear Ca^{2+} signaling in cardiac myocyte excitation-transcription coupling. *Journal of Clinical Investigation*, 116(3):675–682, 2006. doi: 10.1172/JCI27374.

[166] Yissachar, N. et al. Dynamic Response Diversity of NFAT Isoforms in Individual Living Cells. *Molecular Cell*, 49(2):322–330, 2013. doi: 10.1016/j.molcel.2012.11.003.

[167] Young, G.W.D. and Keizer, J. A single-pool inositol 1,4,5-trisphosphate-receptor-based model for agonist-stimulated oscillations in Ca^{2+} concentration. *Proceedings of the National Academy of Sciences*, 89(20):9895–9899, 1992. doi: 10.1073/pnas.89.20.9895.

[168] Yu, T. et al. The Physiome Model Repository 2. *Bioinformatics*, 27(5):743–744, 2011. doi: 10.1093/bioinformatics/btq723.

[169] Zahradníková, A. and Zahradník, I. Description of modal gating of the cardiac calcium release channel in planar lipid membranes. *Biophysical Journal*, 69(5):1780–1788, 1995. doi: 10.1016/S0006-3495(95)80048-2.

[170] Zahradníková, A. and Zahradník, I. A minimal gating model for the cardiac calcium release channel. *Biophysical Journal*, 71(6):2996–3012, 1996. doi: 10.1016/S0006-3495(96)79492-4.

[171] Zheng, M. et al. Sarcoplasmic reticulum calcium defect in Ras-induced hypertrophic cardiomyopathy heart. *American Journal of Physiology-Heart and Circulatory Physiology*, 286(1):H424–H433, 2004. doi: 10.1152/ajpheart.00110.2003.

[172] Zhu, W. et al. Ca^{2+}/Calmodulin-dependent Kinase II and Calcineurin Play Critical Roles in Endothelin-1-induced Cardiomyocyte Hypertrophy.

Journal of Biological Chemistry, 275(20):15239–15245, 2000. doi: 10.1074/jbc.275.20.15239.

[173] Zima, A.V. and Blatter, L.A. Inositol-1,4,5-trisphosphate-dependent Ca^{2+} signalling in cat atrial excitation–contraction coupling and arrhythmias. *The Journal of Physiology*, 555(3):607–615, 2004. doi: 10.1113/jphysiol.2003.058529.

[174] Zima, A.V. et al. IP_3-dependent nuclear Ca^{2+} signalling in the mammalian heart. *The Journal of Physiology*, 584(Pt 2):601–611, 2007. doi: 10.1113/jphysiol.2007.140731.

[175] Zima, A.V. et al. Ca^{2+} spark-dependent and independent sarcoplasmic reticulum Ca^{2+} leak in normal and failing rabbit ventricular myocytes. *The Journal of Physiology*, 588(Pt 23):4743–4757, 2010. doi: 10.1113/jphysiol.2010.197913.